# Antiferromagnets and Luttinger Liquids: Two Strongly Correlated Systems

**Ann Mattsson**

Institute of Theoretical Physics

Göteborg 1997

Doctoral thesis for the Degree of Doctor of Philosophy

# Antiferromagnets and Luttinger Liquids: Two Strongly Correlated Systems

**Ann Mattsson**

Institute of Theoretical Physics
Chalmers University of Technology and Göteborg University
S-412 96 Göteborg, Sweden

Göteborg, April 1997

The cover: “Africa” from Brookes, R., The General Gazetteer; or Compendious Geographical Dictionary. Eighth Edition. Dublin, 1808. With thanks to The Perry-Castañeda Library Map Collection, a feature of UT Library Online, University of Texas at Austin. Edited by Thomas Mattsson.

ISBN 91-7197-480-6
ISSN 0346-718X
ITP 97-06

Chalmersbibliotekets reproservice
Göteborg 1997

“*To Hale-Bopp*”

## Abstract

Strongly correlated systems show a variety of intriguing properties and have been extensively studied over the years. In this thesis two strongly correlated systems are discussed: the two-dimensional antiferromagnet and the Luttinger liquid.

The Luttinger liquid has attracted much interest as a paradigm of non-Fermi liquid behavior. In the first part of the thesis, basic properties of Fermi liquids are briefly described while those of Luttinger liquids are considered in more detail. The differences in spectral properties of Luttinger liquids and Fermi liquids are discussed, as are the consequences for photoemission experiments. In this context Luttinger liquids with boundaries, treated in Papers I, II, and III, are introduced. The exact single-electron Green's function at finite temperature is calculated with bosonization methods, for both periodic and finite open-boundary systems. The corresponding local spectral density is analyzed. For a system with open boundaries, the well-known zero temperature bulk behavior always crosses over to a boundary dominated regime for small energies, while at finite temperature the low energy behavior becomes quadratic. For a periodic finite-size system we also calculate the Coulomb-blockade-like oscillations and study their dependence on interaction and temperature.

The two-dimensional antiferromagnet has attracted much attention due to its connection to the undoped phase of the ceramic high-temperature superconductors. In the second part of the thesis including Papers IV and V, the two-dimensional Heisenberg antiferromagnet defined on the triangular and the honeycomb lattices is studied. We use the Schwinger-boson mean-field theory to investigate the stability of the ground state with respect to frustration. For the honeycomb lattice model we find an increased Néel stability as compared to the classical case. The dynamic structure factor is considered for various temperatures and the spin-wave velocity and the susceptibility are presented as functions of frustration for spin $S = \frac{1}{2}$. In the case of the intrinsically frustrated triangular lattice model we obtain, in the limit of infinite spin, results in complete agreement with the linear spin-wave theory. In contrast to the latter, however, two of the three modes acquire a mass for finite spin. The origin of this effect is discussed.


---


**Descriptors**: Strongly correlated systems, Luttinger liquid, boundary effects, finite-size effects, bosonization, photoemission, antiferromagnet, Heisenberg model, frustration, Néel order.

This thesis consists of an introductory text together with original research articles. The articles are listed below and will be referred to in the text as Paper I to Paper V.

I. **Boundary Effects on Spectral Properties of Interacting Electrons in One Dimension.**
Sebastian Eggert, Henrik Johannesson, and Ann Mattsson.
Physical Review Letters **76**, 1505 (1996).

II. **Properties of a Luttinger Liquid with Boundaries at Finite Temperature and Size**.
Ann Mattsson, Sebastian Eggert, and Henrik Johannesson.
Göteborg ITP 97-01, To be submitted to Physical Review B.

III. **Correlation Functions of Interacting One-Dimensional Fermions at Finite Size and Temperature**.
Sebastian Eggert, Ann Mattsson, and Jari Kinaret.
Göteborg ITP 97-08, Submitted to Physical Review Letters.

IV. **Spin Dynamics of the Triangular Heisenberg Antiferromagnet: A Schwinger-Boson Approach.**
Ann Mattsson.
Physical Review B **51**, 11574-11579 (1995).

V. **Frustrated Honeycomb Heisenberg Antiferromagnet: A Schwinger-Boson Approach.**
Ann Mattsson, Per Fröjdh, and Torbjörn Einarsson.
Physical Review B **49**, 3997-4002 (1994).

# Contents

# Introduction

If I had been living in the 19th century (and if I had been a man!) I would probably have been an explorer like Henry Stanley (1841-1904) or David Livingstone (1813-1873). In my parents home there is a book written by Stanley and accompanying this book are some very beautiful maps containing large so-called "blank areas". The geographical blank areas are not so many nowadays but fortunately there are other areas where there is still a need for explorations and I have chosen to work in the field of physics (whereas Stanley and Livingstone chose to explore Africa).

Like Stanley and Livingstone, physicists also draw maps and we still have to face the fact that there is no complete map but reality. Each map has its limitations, and to get an overall view of reality one has to study different types of map. The most common type in geographical contexts are topographical maps showing the surface features of a region including its relief, rivers, and lakes, etc. It also shows man-made features such as roads, bridges, etc. However, there are other types of map: geological, historical, political, vegetational, etc. In my view there are different types of map in physics as well. There are usually many ways to describe a phenomenon in Physics, each emphasizing some particular aspect. In fact, as stressed by Niels Bohr (the father of quantum physics) there can be no single map of Nature. Nature can only be represented by *complementary maps*.

The most obvious research activity is to do what Stanley and Livingstone did, starting at some already known place and then make an expedition into an unknown area. But there are other types of research one can do, like exploring areas already partly covered by other people. By studying many types of maps on different scales one can draw new conclusions in order to improve and increase our understanding of the field. An analogy is to prospect for gold and other minerals. Perhaps a botanical map, indicating where different flowers are supposed to be found, can help somebody prospecting for gold to find his gold mine by his knowledge that a certain flower usually grows near a vein of gold. This type of research is very well described by Proust who said that "the real exploration is not to look for new land but to look with new eyes".

When I am hiking in the mountains I enjoy looking for the map edge in the terrain, but of course I see nothing special since the boundary of the map is artificial. This is also the case with boundaries between different subfields of physics. At the center of the map is usually placed the currently most important feature while the extent to which the surroundings are covered depends on the scale of the map. Sometimes there are no maps covering the areas in between different major sites, or the maps in between are of a different kind, constructed with another technique. For me these areas are the most interesting areas because I have a strong belief that it is here that great new discoveries are made. To incessantly be thrown between different cultures, each with its own language and tradition, helps to distinguish between relevant and irrelevant information and provides a fertile ground for new thoughts to come through. Indeed, condensed matter, my own specialty, is a very wide field. A large number of subjects are studied with a great variety of experimental and theoretical methods. This cross-disciplinary character is for me one of the most attractive features of research in condensed matter theory.

Before I make a journey to a place I have never visited before I always try to orient myself by buying a map and talk to people who have already been there. This thesis is an attempt to describe my field of research for those of you who want to travel in the same area. Perhaps you will not find every part of the field worthwhile to visit but I hope that you will enjoy the places you do visit.

In chapters 1, 2, and 4 I place the relevant details for the exploration of the small blank areas that I have undertaken, and that I report on in chapter 3 and 5, on a map of my own creation. The maps I draw are by no means complete but they hopefully contain the main features so that the reader can orient herself towards my own work.

The success of a journey is largely due to how well the preparations were made, and sometimes the preparation is more agreeable than the journey itself. Mosquitos, malaria, heavy rain, snakes and impenetrable undergrowth can make journey to purgatory but then, suddenly, you stand there, before Lake Tanganyika in all its splendor, your discovery, the goal of your exploration.

Isn't that what we are all dreaming about?

## Outline of the introductory text

Chapter 1 is a short introduction to strongly correlated systems of which the following topics are examples.

Chapter 2 gives an introduction to Luttinger liquids in general. The aim is to familiarize the reader with the topic in order for her to be able to follow my own work presented in Chapter 3 and in Papers I, II, and III.

Chapter 3 focuses on my contribution to the study of Luttinger liquids: boundary, finite-size, and temperature effects.

Chapter 4 gives a general introduction to antiferromagnets. The aim is again to familiarize the reader with the topic so that she may be able to follow my own work presented in chapter 5 and in Papers IV and V.

Chapter 5 concentrates on my study of 2D antiferromagnets: disordering effects, specifically frustration.

## Summary of the papers

The content of the five papers is as follows:

Paper I treats the one-dimensional spinful Tomonaga-Luttinger model. Using bosonization methods we calculate the single-particle Green's function of the model in the presence of an open boundary. The critical exponents of the local spectral density and the momentum distribution are shown to be sensitive to the boundary: the well-known bulk behavior always crosses over to a boundary-dominated regime for small energies or small momenta. We consider explicitly the example of the large-$U$ Hubbard model and we also discuss implications for photoemission experiments on quasi-1D organic conductors.

Paper II is a generalization of Paper I in two respects: Temperature and finite-size effects are included. The *exact* finite temperature single-particle Green's function for a Luttinger liquid confined by open boundaries is calculated with the use of bosonization methods. The corresponding local spectral density is constructed and analyzed in detail. At finite temperature a new behavior opens up for small energies and we discuss the consequences for photoemission experiments.

Paper III is a spin-off from the work in Paper II. We present the explicit expression for the single particle Green's function for a spin-less system of finite size at finite temperature. From this expression we can calculate Coulomb blockade oscillations and we can determine their dependence on interaction strength and temperature. We also consider the density-density correlation function of the same system at finite temperature and perform a numerical simulation of the corresponding Hubbard model in order to test our analytical result. The numerical simulations show excellent agreement with our analytical results.

Paper IV presents an analysis of the intrinsically frustrated 2D Heisenberg antiferromagnet on a triangular lattice. Using Schwinger-boson mean-field theory we obtain an excitation spectrum that agrees completely with the linearized spin wave theory result in the limit of infinite spin. However, in contrast to the linearized spin wave theory, two of the three modes acquire mass for finite spin and we discuss the origin of this effect. In this thesis I have also included a better copy of Figure 2 in the paper.

Paper V is a study of the frustrated 2D Heisenberg antiferromagnet on a honeycomb lattice. With the use of the Schwinger-boson mean-field theory we calculate the spin-wave velocity and the uniform susceptibility as functions of the strength of the frustrating interaction for spin $S = \frac{1}{2}$. The dynamic structure factor is calculated for various temperatures and frustrations. We also examine the stability of the Néel state and for large $S$ we find an increased stability as compared to the classical case.

# 1 Strongly Correlated Systems

Strongly correlated systems are systems where the different parts strongly influence each other: The influence is so strong that it does not even make sense to talk about the system in the absence of these correlations. Instead, correlations have to be built into the system description *from scratch.*

Let us look at the example of a system of *molecules* and its various phases. At one extreme we have the dilute gas phase, where the molecules can be seen as essentially freely moving particles which do not interact with each other, and hence are uncorrelated. The other extreme is the solid phase, where the molecules form a crystal where every molecule has a fixed position relative to the other molecules, that is, the molecules are strongly correlated. In between these two extremes is the liquid phase, where the molecules are correlated to various degrees.

Another example: the conducting *electrons* in an alkali metal, such as a $Na$ or $K$ metal, can be very well described as freely moving, that is non-interacting, electrons in a periodic potential (originating from the alkali ions that are arranged in a lattice structure). The electrons then form a so-called "Fermi gas". The other extreme, the electron solid, can also be formed under suitable conditions, despite the small electron mass that implies large quantum fluctuations. This solid state of electrons is called a Wigner crystal [1], and the highly correlated electrons in such a crystal are arranged in a triangular pattern. To describe electrons in solids other than the alkali metals, we need to take into account that the electrons are interacting with each other and thus become correlated. In analogy with a liquid of molecules, interacting electrons can be said to form an *electron liquid.*

In condensed matter theory, as in other areas of physics, we try to predict the behavior of a system by doing calculations on a model. In a model, the inclusion of interactions between electrons can be done in several ways, the conventional framework being Landau's Fermi liquid theory or equivalently perturbation theory.

Perturbation theory is a very good way of treating a system as long as one has a small parameter governing an interaction that may be considered as a *disturbance* of a free system. The properties of the interacting system can then be expressed in terms of the properties of the unperturbed system, with known properties. The small parameter does not necessarily need to be a coupling constant, a popular method (the "large-$N$ expansion") uses $1/N$ as a small parameter with $N$ counting the amount of symmetry in the system. A well-known and efficient methodology has been developed for the calculation of perturbation series in terms of Feynman diagrams and this methodology is used in almost every area of physics. Diagrammatic methods are still developed to treat new kinds of problem. Perturbation theory does not require any specific properties of the unperturbed system but—and this is important—it limits itself to studies of properties *within* a single phase of the system.

Landau's Fermi liquid theory is a very successful theory in condensed matter and I will review some aspects of it in Sec. 2.1. The theory is based on the Fermi gas model and, as long as the specific *fermionic particle* nature of the Fermi gas is present, even strongly correlated systems can be studied by Fermi liquid theory. This means that in order for a system to be a Fermi liquid, the interaction must produce 'quasi'-particles that essentially behave as free fermions. Strange as it may sound, an interpretation of Fermi liquid theory in terms of microscopic quantities can be done with the very use of perturbation theory.

There are many electron systems that cannot be described by the Fermi liquid theory. These have a common feature in that they cannot be mapped onto a weakly interacting system, or equivalently, on the slightly perturbed Fermi gas. Instead, the strong correlations among the electrons lead to behavior not seen in ordinary Fermi liquids, so-called *non-Fermi liquid behavior*.

There are many different types of strongly correlated system. Let me give you some examples.

An ordinary magnet is a typical example of a strongly correlated system. To form a net magnetization all dipoles in the material must cooperate and align themselves with respect to each other.

Another example is the superfluid phase of $^3$He. Last year's (1996) Noble prize honored D. M. Lee, D. D. Osheroff, and R. C. Richardson for their discovery of this phenomenon. The superfluid phase of $^3$He is a system that can not be described by Fermi liquid theory even though the normal *liquid* phase of $^3$He is the very paradigm of a Fermi liquid system. Since $^3$He are fermions they are not supposed to be able to form a superfluid which is the low temperature phase of a boson system (Bose-Einstein condensation) like the $^4$He liquid. However, it turns out that strong correlations between the fermions lead to pairing among them and the two-fermion bound states thus produced are bosonic in nature and can form a Bose-Einstein condensate.

This kind of pairing of fermions is also the reason behind the non-Fermi liquid behavior of low temperature superconductors. According to the BCS-theory, developed by Bardeen, Schrieffer, and Cooper, a bound pair of electrons, a so-called *Cooper pair*, is formed due to lattice vibrations, *phonons*, creating an attractive interaction between the electrons. Also the founders of the BCS-theory were awarded a Nobel prize, in 1972.

Yet another example of non-Fermi liquid behavior in a strongly correlated system is the *multichannel* Kondo effect. Here the conduction electrons in a magnetically doped metal try to coherently eliminate the disturbance created by the extra spins (from the magnetic ions) added to the system. In contrast, the *single* channel Kondo system, with only s-wave electrons participating, *can* be described by the Fermi liquid theory—an unusual example where strong correlations are successfully taken into account by this theory.

A remarkable system that can show both Fermi liquid and non-Fermi liquid behavior is the Hall system. This is an interesting system even at the classical level where a (two-dimensional) thin film, placed in a magnetic field and fed with a current perpendicular to the field, develops a potential difference between the edges perpendicular to both current and magnetic field. The classical effect was discovered by E. H. Hall as early as in 1879[1]. About 100 years later, in 1980, Klaus von Klitzing [3] studied the Hall effect under extreme conditions: very high magnetic field and very low temperature, and discovered plateaus in the plot of the Hall resistance vs. magnetic field. This discovery of the *integer quantum Hall effect* (with the Hall resistivity quantized in *integer* steps of $h/e^2$, $h$ being Planck's constant and $e$ the electron charge) was honored with the 1985 Nobel Prize. Even though the integer Hall effect can be successfully explained within Fermi liquid theory, the *fractional quantum Hall effect* (with *fractional* quantization of the Hall resistivity) discovered some years later [4] cannot be explained without taking into account the strong electron correlations. We shall return to this fascinating system later.

In photoemission experiments on quasi-1D organic conductors, results are obtained that differ substantially from predictions by Fermi liquid theory. These conductors have highly anisotropic transport properties and effectively behave as one-dimensional metals. This one-dimensionality is supposed to lead to non-Fermi liquid behavior, as is also seen in photoemission spectra. The best candidate theory for explaining the observations is the *Luttinger liquid theory*, one of the major topics of this thesis.

Some of the most intriguing systems exhibiting strong correlations are the high temperature superconductors. I will try to motivate my choice of the two areas focused upon in my study, *2D antiferromagnets* and *Luttinger liquids*, in the context of these high-$T_c$ superconductors. However there are important connections to other strongly correlated systems (including the organic

[1] His report on the discovery [2] is very stimulating to read as it is written in a personal style not found in scientific articles nowadays.

conductors!) as I will point out as we go along.

## 1.1 High-$T_c$ superconductors

In 1986 Bednorz and Müller [5] discovered the first high-$T_c$ superconductor, a discovery awarded yet another Nobel prize, in 1987. They found this superconductivity below a critical temperature, $T_c \sim 35K$, in the doped ceramic copper oxide compound $La_{2-x}Ba_xCuO_4$. Later other types of copper oxide compounds have also been shown to exhibit superconductivity. For the moment (April 1997) the compound with the highest critical temperature is a mercury-based compound, $HgBa_2Ca_2Cu_3O_{8+\delta}$ with $T_c$ about $133K$ at atmospheric pressure [6].

All of these discoveries of new superconductors have been based on empirical observations since still, more than ten years after the first discovery, there is no theory with predictive power. In fact, no one knows why cuprates behave as they do, not even in their normal state above $T_c$. An enormous theoretical activity is going on and the research is being carried out on several frontiers simultaneously.

**Figure 1.1**: Phase diagram of $La_{2-x}M_xCuO_4$ where $M = Ba$ or $Sr$. AF=antiferromagnetic; SG=spin-glass; I=insulator; M=metal; SC=superconductor; O=orthorhombic; T=tetragonal (from Ref. [7]).

There is a strong belief that the explanation for the superconductivity is hidden in the anomalous behavior of the "normal" (non-superconducting) state of the ceramic compounds. In Fig. 1.1 a generic phase diagram for a high-$T_c$ superconductor is shown. In actual fact, each and every single phase has spurred a whole industry of model building and theoretical analyses. Experimental investigations of the cuprates continue and with new technology better samples can be manufactured and cleaner experiments can be performed which can reject or support a theory. I have studied two different subjects which both are connected to this search for an explanation of the "normal" state of the high-$T_c$ superconductors.

### 1.1.1 Antiferromagnets

There are many reasons why people study magnetic phenomena, ranging from fundamental questions in quantum mechanics to applications in materials science. But why study *antiferromagnets* and then, why *2D*?

One reason is that the high-$T_c$ superconductors discussed above are, in fact, antiferromagnets when not doped, i. e. the net magnetic moments of neighboring copper ions tend to be aligned in the insulating phase (see Fig. 1.1).

At low $T$ and $x$ (doping) the material is a pure 3D antiferromagnet. Above $T_N$ (the Néel temperature), though, the spins are still strongly correlated in the 2D copper-oxide planes common to the high-$T_c$ compounds [7]. Upon doping, the antiferromagnetic correlations disappear, leaving way for superconductivity. This experimentally observed competition between antiferromagnetic correlations and superconductivity makes it important to understand precisely *what* happens when a two-dimensional quantum antiferromagnet disorders.

In fact, the precise condition for having antiferromagnetic order in two dimensions is an open problem. In a 1D antiferromagnet we have disorder at all temperatures (see Table 1.1) as can be shown from the exact Bethe Ansatz solution [8]. In 2D we also have disorder as long as $T \neq 0$ according to the Mermin-Wagner theorem [9]. On the other hand, in 3D we always have a non vanishing Néel temperature, $T_N^{3D}$, which means that at $T < T_N^{3D}$ we have order. It remains to establish under what conditions one has order in 2D at

| | $T > T_N^{3D}$ | $T_N^{3D} > T > 0$ | $T = 0$ |
|---|---|---|---|
| $1D$ | $D$ | $D$ | $D$ |
| $2D$ | $D$ | $D$ | ? |
| $3D$ | $D$ | $O$ | $O$ |

**Table 1.1**: $T_N^{3D}$: The Néel temperature for a 3D system, $D$: Disordered, $O$: Ordered

$T = 0$ (see Table 1.1). As we shall see in Chapter 4, there are basically three things that control the situation: the *magnitude of the spin*, the *coordination number* of the lattice, and the presence of *frustration*(i. e. interactions that work against magnetic order). My own work, presented in Chapter 5, focuses on this last effect.

An ordered system, such as an antiferromagnet, is very interesting but as we shall see in the following section, the behavior of a 1D system, which is always disordered as seen from Table 1.1, can also exhibit very rich behavior.

### 1.1.2 Luttinger liquids

The "normal" metallic phase of a high-$T_c$ superconductor (see Fig. 1.1), that is at $T > T_c$, is not very normal at all!. At least there is no theory presently available that can explain its strange behavior, such as the observed linear resistivity or the anomalies in the Raman scattering spectrum, properties that cannot be understood within the Fermi liquid theory. Since the key to the mechanism of superconductivity is considered as hidden in the normal phases, a new theory for the metallic phase must be developed to explain this non-Fermi liquid behavior.

The favored model for describing electron interactions in high-$T_c$ compounds is the Hubbard model [10]. The *one-dimensional* Hubbard model behaves as a *Luttinger liquid* at low energies (and not as a Fermi liquid!), showing some spectacular properties as we shall see in Chapter 2 where I review Luttinger liquid physics. In 1990 Anderson [11] proposed that some of the Luttinger liquid features of the 1D Hubbard model could be transferred to the 2D model in order to describe the conducting electrons in the copper-oxide planes in the normal metallic phase. The specifics of this proposal is still controversial although, more generally speaking, the non-Fermi liquid behavior of the metallic phase of a high-$T_c$ superconductor motivates the study of *any* new liquid theory, including the Luttinger liquid.

It is interesting to note that much of the basic work on Luttinger liquids was done before 1986, the year when the high-$T_c$ superconductors entered the stage. The discovery of the high-$T_c$ superconductors merely boosted this interest. The early works, like the original work by Tomonaga in 1950, were inspired by problems in mathematical physics, while during the years that followed, theory got closer to the "real world", including the quasi-one-dimensional organic conductors mentioned above. Since the 70s much of the motivation for studying 1D models has originated from experiments carried out on these conductors and, indeed, this is also the case in our work presented in Chapter 3.

The development of nanostructure technology has made possible a new type of experiment. Experimentalists are now able to *fabricate* quasi-one-dimensional structures, such as 'quantum wires'. This also motivates the study of Luttinger liquids as does the recent discovery that the edge states of a fractional quantum Hall system are chiral Luttinger liquids. The chiral Luttinger liquids permit very clean experimental studies and once again the interest in one-dimensional system is boosted.

In this context, it is also appropriate to mention that the development of theoretical methods for studying Luttinger liquids has not only followed from studies done within the condensed matter community. A parallel development has taken place within the quantum field theory, mainly in the study of the

Thirring model.

To conclude, in one way the motivation from high-$T_c$ to study Luttinger liquids is not very strong, as a simplified one-dimensional model can not possibly solve the mystery of high temperature superconductors. From a fundamental point of view, however, there is a very strong motivation from high-$T_c$ to study Luttinger liquids: much of our intuition is based on the Fermi liquid theory. Working on other electron liquids, such as the Luttinger liquid, trains our synapses not too have to strong prejudices about possible electron behavior, a necessary condition for designing the proper non-Fermi liquid theory for the normal metallic phase of the high-$T_c$ superconductors.

# Part I

# Luttinger Liquids

# 2 Luttinger Liquids: Introduction

The concept of a Luttinger liquid is closely related to that of a Fermi liquid. In both cases we have an exactly solvable model at the "center of the theory", the Tomonaga-Luttinger model and the Fermi gas, respectively. The exactly solvable models are very simple only accounting for the key features of a more realistic model. Both the Fermi gas model and the Tomonaga-Luttinger model describe particles that are Fermions. In the Fermi gas they are free, whereas in the Tomonaga-Luttinger model one also includes a simple interaction ("forward scattering"). The liquid picture appears as we "dress" the "bare" (exactly solvable) models with other features, making them more realistic. These new features do not change the *qualitative* conclusions drawn from the bare models. But the parameters that *quantitatively* describe the system have to be assigned new values, i.e. they need to be *renormalized*.

In this chapter I will first discuss the Fermi liquid concept and in Sec. 2.2 I will show why Fermi liquid theory does not work in one dimension (1D). A new theory describing fermions in 1D thus needs to be developed and in Sec. 2.3 I present the core of this Luttinger liquid theory, the Tomonaga-Luttinger model. In Sec. 2.4 the Tomonaga-Luttinger model is "dressed" in the context of the Hubbard model and in Sec. 2.5 I consider some experimental realizations of Luttinger liquids. Finally, in Sec. 2.6, I summarize the main differences between Fermi liquid and Luttinger liquid behavior with special emphasis on the spectral properties.

## 2.1 Fermi liquid theory

Fermi liquid theory is a central theory in condensed matter physics. It has had—and still has—an enormous impact on the way we interpret experiments involving fermions. This impact is seen in the notion of "non-Fermi liquid behavior"; fermion behavior that cannot be explained by Fermi liquid theory is considered strange and mysterious.

Fermi liquid theory is equivalent to the physics of quasiparticles and I will start this section with a discussion on how the quasiparticle concept forms the very basis of Fermi liquids. In the following subsection I will give some examples of how these quasiparticles manifest themselves in different physical properties of a Fermi liquid system. For a classical treatise, see the book by Pines and Nozières [12].

### 2.1.1 Quasiparticles

To understand what a quasiparticle is, one has to know what a particle is. A "classical" particle is a distinct object, for example one can measure its radius, its mass and its charge. However, to transform this knowledge into a mathematical (physics) language is not very trivial and when it comes to quantum particles things get even worse. In quantum physics we also have the particle-wave dualism which makes the concept of a particle even more vague. The solution is to describe a particle by presenting its quantum numbers which label the state of the particle, its spin and momentum, for example. All information on the particle is embedded in its quantum numbers. A particle in a specific state is also the eigenstate of the Hamiltonian describing the system.

The main (but unproven) hypothesis of Landau's Fermi liquid theory is that the *same* quantum numbers that label the fermions in the free Fermi gas can be used to describe the physics of the interacting fermionic system, the Fermi liquid. The objects carrying these quantum numbers—whatever they are!—go under the name of *quasiparticles*. Landau's Fermi liquid theory describes the properties of a many-fermion system at low energies and temperatures in its normal state, that is, in a state where the symmetry of the system is unbroken. Important to note is that Fermi liquid theory only applies to fermionic systems, and that the statistical interaction is taken care of as early as at the level of Fermi gas theory. As we saw in Chapter 1, many of the systems showing non-Fermi liquid behavior do not have this Fermi gas symmetry, why they could not be described using Fermi liquid theory. For example ordinary superconductors where the fermions (electrons) form pairs have the symmetry of a Bose gas and thus need to be described by a theory containing this symmetry, such as the BCS-theory.

If we add a fermion to a non-interacting system this particle will occupy an unoccupied state without disturbing the other particles in the system. The particle can be described as the difference between the new and the old system. Similarly, we can define a quasiparticle as the difference between an *interacting* system with an added fermion and a system without such an addition. When we have interacting fermions in the original system, the added fermion will influence and be influenced by the other fermions thereby creating some disturbance or perturbation in the system. The composite formed by the added particle *and* the perturbed distribution of the other particles is the quasiparticle.

The quasiparticle concept has its limitations, though. For example, quasiparticles have a finite lifetime as the perturbation disperses. Only near the Fermi wave vector, $k_F$, is the lifetime large and thus the quasiparticles well defined. Small excitations above the ground state are thereby the fundamental objects for which Fermi liquid theory works.

The above discussion can formally be summarized in the equation for the quasiparticle energy, that is, the energy change, $E$, in an interacting fermion system when adding a particle to it:

$$E = \sum_{\boldsymbol{k},\sigma} \epsilon_{\boldsymbol{k}} \delta n_{\boldsymbol{k},\sigma} + \frac{1}{2} \sum_{\boldsymbol{k},\boldsymbol{k}',\sigma,\sigma'} f(\boldsymbol{k},\boldsymbol{k}',\sigma,\sigma') \delta n_{\boldsymbol{k},\sigma} \delta n_{\boldsymbol{k}',\sigma'} \ . \tag{2.1}$$

Here $\epsilon_{\boldsymbol{k}}$ is the single particle energy, $\delta n_{\boldsymbol{k},\sigma}$ is the change of the Fermi-Dirac distribution due to the added particle, and $f$ is a function, introduced by Landau, describing the interaction between quasiparticles. By symmetry arguments the $f$-function can be expanded in terms of Legendre polynomials, and by using the low energy expansion of the single particle energy

$$\epsilon_{\boldsymbol{k}} = \frac{k_F}{m^*}(|\boldsymbol{k}| - k_F) \ , \tag{2.2}$$

one can obtain expressions for the thermodynamic parameters specific heat, spin susceptibility, and compressibility, in terms of the effective mass $m^*$ and the Landau parameters $F_n^{a,s}$, i.e. the expansion coefficients of the $f$-function (see [13] for details and notation). A number of other observables may also be derived, including transport properties [12].

As we have already noted, Fermi liquid theory has been very influential in forming our view of how many-fermion systems behave. Fermi liquid theory has also successfully predicted the existence of certain new phenomena, such as the "zero sound" in $^3$He. Still, the theory has rather limited value for quantitative predictions in general. For example, the large number of phenomenological parameters typically needed to describe electrons in metals has limited the use of Landau Fermi liquid theory in computing observables for these systems. Rather, the theory has primarily been important at a conceptual level, to help us think about interacting electrons, and suggesting what models and approximations may work (or not work!). In this thesis, I will therefore focus on the qualitative aspects of Fermi liquids, with particular attention to similarities to, as well as differences from, Luttinger liquids.

### 2.1.2 What do quasiparticles look like?

It is rather easy to translate the Fermi liquid concept of quasiparticles into the microscopic level, thus obtaining an *interpretation* of the quasiparticle picture in microscopic quantities such as the single particle Green's function. We first note that the exact Green's function for the Fermi gas is

$$G(\boldsymbol{k},\omega) = \frac{1}{\omega - \epsilon_{\boldsymbol{k}0} - i0^+} \ , \tag{2.3}$$

where $\epsilon_{\boldsymbol{k}0} = |\boldsymbol{k}|^2/2m - \mu$, $\mu$ being the chemical potential and $0^+$ is an infinitesimal positive constant. Turning on interactions modifies the Green's function and it can now be written as

$$G(\boldsymbol{k},\omega) = \frac{1}{\omega - \epsilon_{\boldsymbol{k}0} - \Sigma(\boldsymbol{k},\omega)} \ , \tag{2.4}$$

where $\Sigma(\boldsymbol{k},\omega)$ is the self energy originating from the interactions among the fermions. The self energy $\Sigma(\boldsymbol{k},\omega)$ is a complex quantity with the real part, $\mathrm{Re}\,\Sigma(\boldsymbol{k},\omega)$, shifting the energy, $\epsilon_{\boldsymbol{k}0} \to \epsilon_{\boldsymbol{k}0} + \mathrm{Re}\,\Sigma(\boldsymbol{k},\omega)$, and the imaginary part, $\mathrm{Im}\,\Sigma(\boldsymbol{k},\omega)$, measuring the inverse lifetime of a quasiparticle, $\tau^{-1}$. Within Fermi liquid theory different approximations can be made for the self energy but common to all is that the imaginary part of $\Sigma$ will be quadratic in $(|\boldsymbol{k}|-k_F)$ and $\omega$. Taking the simplest $\boldsymbol{k}$-independent ($|\boldsymbol{k}| = k_F$) self energy consistent with the Fermi liquid theory,

$$\Sigma(\boldsymbol{k},\omega) = \alpha\omega + i\beta\omega^2 \ , \tag{2.5}$$

one obtains the following Green's function at the Fermi level:

$$G(k_F,\omega) = \frac{Z_{k_F}}{\omega - i0^+} - \frac{Z_{k_F}}{\omega + i/\beta'} \ , \tag{2.6}$$

where $Z_{k_F} = 1/(1-\alpha)$ and $\beta' = Z_{k_F}\beta$. By comparing this Green's function with the free particle propagator, Eq. (2.3), the first term can be identified as having particle nature, the only difference being the factor $Z_{k_F}$ (the *quasiparticle residue*). This first part of the Green's function represents the quasiparticle, which, due to the vanishing of the imaginary part of the self energy at $\omega = \omega_F = 0$ will always be present at the Fermi level. The second part of the Green's function is called the "incoherent" part, and describes collective excitations (originating from oscillations of the Fermi surface).

To further explore the signatures of quasiparticles I will focus on the fermion momentum distribution and on the spectral density, which both can be derived from the single-particle Green's function in Eq. (2.4). Using the self-energy in Eq. (2.5) the momentum distribution can be shown to have the form $(Z_{k_F}\theta(k_F - |\boldsymbol{k}|) + \textit{continuous function})$ as shown in Fig. 2.1, together with the distribution for a free fermion gas. The quasiparticle nature is seen in the discontinuity at the Fermi surface, of magnitude $Z_{k_F}$. In the case when $Z_{k_F} = 0$ is called a *marginal* Fermi liquid, this distribution is similar to the Luttinger liquid distribution, as we will see in Fig. 2.8.

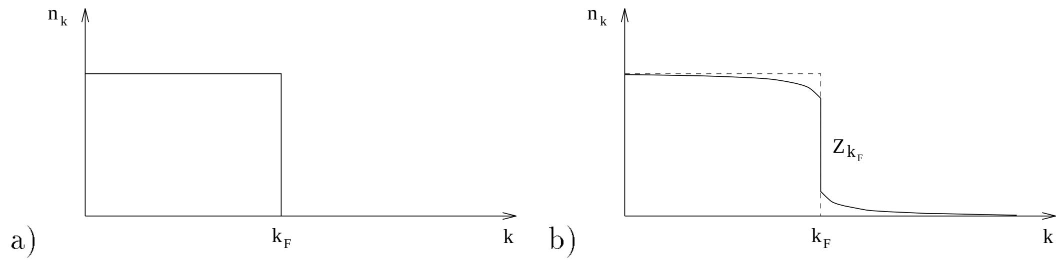


**Figure 2.1**: Momentum distribution function for a) free fermions and b) interacting fermions within the Fermi liquid theory.

Another important quantity is the spectral density, $\rho(\boldsymbol{k}, \omega)$. It measures the probability that a fermion added to the system (in its ground state) is found in a state with momentum $\boldsymbol{k}$ and energy $\omega$, and is proportional to the imaginary part of the Green's function,

$$\rho(\boldsymbol{k}, \omega) = \frac{1}{\pi} \mathrm{Im}\, G(\boldsymbol{k}, \omega) \ . \tag{2.7}$$

We immediately see that for a non-interacting fermion, described by the Green's function in Eq. (2.3), the spectral function will be a $\delta$-function, $\rho(\boldsymbol{k}, \omega) = \delta(\omega - \epsilon_{\boldsymbol{k}0})$. This is clearly a single particle for which the (kinetic) energy is determined by the momentum. Similarly, from Eq. (2.6) we straightforwardly obtain the spectral function for interacting fermions with momentum equal to the Fermi wave vector. This is shown in Fig. 2.2a. We see the quasiparti-

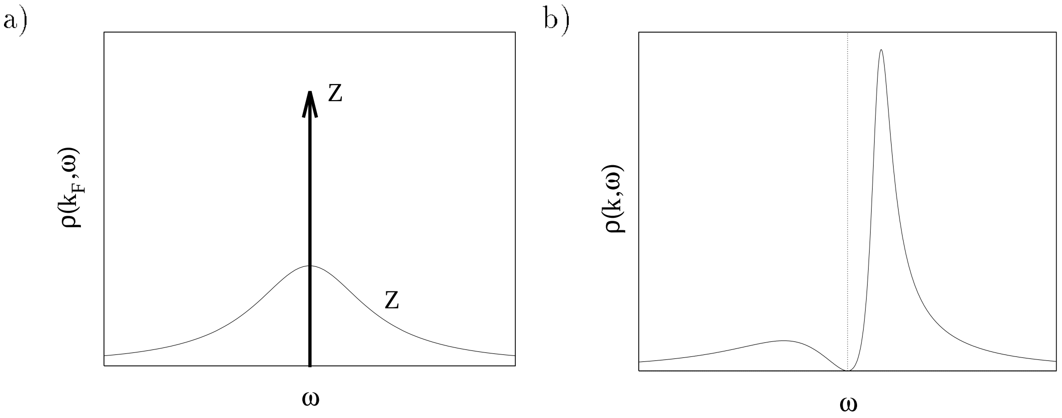


**Figure 2.2**: a) Spectral function for $|\boldsymbol{k}| = k_F$ for a Fermi liquid system as in Eq. (2.6). Note the quasiparticle peak and the "incoherent" Lorentzian background. b) A typical spectral function for a Fermi liquid for $|\boldsymbol{k}| \neq k_F$.

cle $\delta$-function peak originating from the first term in Eq. (2.6) and the broad Lorentzian distribution originating from the incoherent part of the Green's function. With the use of Eq. (2.4) and Eq. (2.5) the spectral function can be derived for other values of $\boldsymbol{k}$. A typical spectral density for $|\boldsymbol{k}| \neq k_F$ is also shown in Fig. 2.2b. Note in particular the broadening of the $\delta$-function peak into a Lorentzian (with width inverse proportional to the lifetime).

I will end this section with a remark connected to Fig. 2.2a. As seen in this figure the total spectral weight is $2Z$ and not 1 as it should be, according to a well-known sum rule (a total probability must be 1). This is due to the fact that the Green's function in Eq. (2.6) is not causal, that is, the imaginary part of the denominator in the second term is not negative. The approximation for the self-energy in Eq. (2.5) also fails to keep the total spectral weight (integrated over $\omega$) to the same constant for all $|\boldsymbol{k}|$. This has implications when one tries to fit predicted photoemission curves to experimental data, and work is being done to improve the approximation for the self-energy so as to solve this problem [14, 15, 16].

The Fermi liquid theory is treated in most text books on many-body physics. My main sources have been [13, 17, 18, 19, 20].

## 2.2 Why the Fermi liquid theory does not work in 1D

In this section we shall see that the Fermi liquid picture described above in fact does not work for 1D electron systems. Consequently another picture that describes 1D electrons needs to be developed. The Luttinger liquid is such a picture.

What goes wrong with the Fermi liquid in 1D? Well, let us consider a gas of free fermions, an ideal Fermi gas, under the influence of a potential $\phi(\boldsymbol{r})$. Within linear response theory (see for example Refs [21, 20]) we can calculate the rearrangement of the charge density, expressed as the induced charge $\rho(\boldsymbol{r})$ due to this potential. Going over to Fourier transforms we have the relation:

$$\rho(\boldsymbol{k}) = \chi(\boldsymbol{k})\phi(\boldsymbol{k})\,, \tag{2.8}$$

where $\chi(\boldsymbol{k})$ is the free particle response function related to the density-density correlation function. Lindhard derived an expression for this function [22] which is therefore also called the Lindhard function:

$$\chi(\boldsymbol{k}) = \int \frac{d\boldsymbol{k}'}{(2\pi)^d} \frac{f_{\boldsymbol{k}'} - f_{\boldsymbol{k}'+\boldsymbol{k}}}{\epsilon_{\boldsymbol{k}'} - \epsilon_{\boldsymbol{k}'+\boldsymbol{k}}}\,, \tag{2.9}$$

where $f_{\boldsymbol{k}}$ is the Fermi distribution function and $d$ denotes the dimension. This response function can be calculated in one, two, and three dimensions. The resulting curves are shown in Fig. 2.3. We see that the 1D curve is singular at $k = 2k_F$ and that the other curves have a cusp and a logarithmic divergent derivative, respectively, at this wave vector. This has implications for

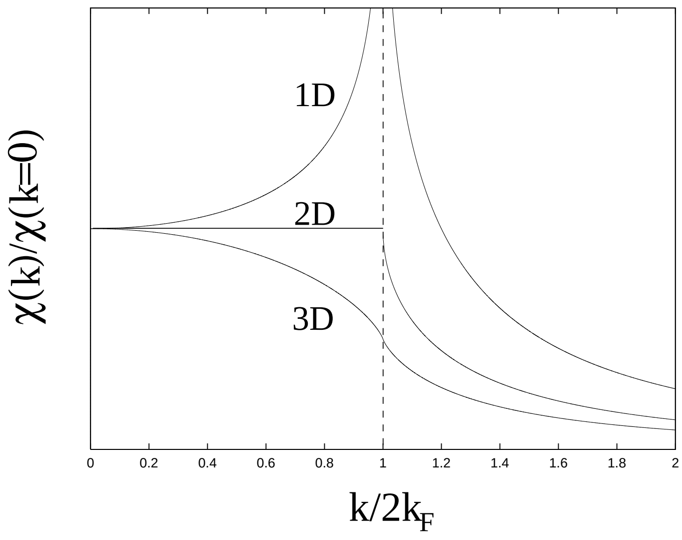


**Figure 2.3**: Lindhard response function for one-, two-, and three-dimensional Fermi gas at T=0, with $k = |\boldsymbol{k}|$

the response of a free fermion gas to a potential. For example, if we consider the potential as coming from ions on a lattice, phonons will couple to the electrons leading to the well-known lattice instability in 1D (the Peierls instability [23]), while in 2D and 3D the electron-phonon coupling results in a "Kohn anomaly" [24] in the phonon dispersion curves.

The potential $\phi(\boldsymbol{k})$ does not necessarily originate from an applied field or ions on a lattice. Much more important for our discussion is that it can be effectively induced by the other fermions in a gas *if these are interacting*. Let us assume that we move one of the fermions a small distance. If the system consists of non-interacting particles nothing will happen but if we consider a system with *interacting* fermions this displacement will change the potential felt by the other fermions and they will adjust according to Eq. (2.8). These adjustments will in turn lead to a new induced potential, leading to new rearrangements. In higher dimensions these adjustments will be damped since the response functions are non-singular and the system will return to its initial state. This is equivalent to the statement that quasiparticles have finite lifetime. In 1D, in contrast, the original disturbance will be *enhanced* since the response function is singular and the gas thus responds to a potential change in a singular way. The disturbance will not be damped but turn into something new that cannot be described by the Fermi liquid theory.

The hypothesis of the one-to-one correspondence between the eigenstates (electrons) in a Fermi gas and the quasiparticles of the Fermi Liquid is represented by the requirement of a nonsingular "adiabatic switching on" of the interaction. The instability in the 1D electron gas described above will thus ruin the fundamental Fermi liquid hypothesis: Turning on interactions among electrons in a 1D Fermi gas will *not* create quasiparticles, at least not of the Fermi liquid type.

The origin of the singular response function is the topology of the 1D Fermi surface, as we shall see now. From Eq. (2.9) we see that the main contribution to the integral comes from particle-hole excitations, giving a nominator of 1, where the particle and the hole have almost the same energy causing the denominator of the integrand to almost vanish. We see in Fig. 2.4 that such particle-hole pairs are connected by a momentum difference $\boldsymbol{k} = 2\boldsymbol{k}_F$. In two and three dimensions the measure keeps the integral finite while this is not the case in 1D; thus a singularity appears.

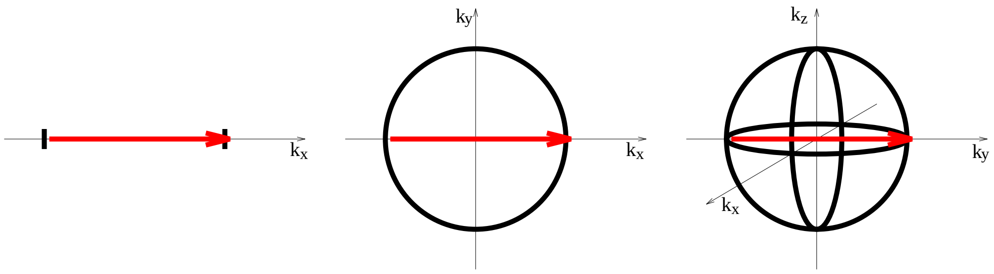


**Figure 2.4**: The Fermi surfaces for one-, two-, and three-dimensional free fermion systems. In each case a vector $\boldsymbol{k}$ is marked connecting a particle-hole pair which gives infinite contribution to the integral in Eq. (2.9).

The nonexistence of quasiparticles in 1D is thus entirely due to the structure of the particle-hole pair spectrum. The free Fermi gas *single* particle spectrum,

$$E(k) = E_F - \frac{v_F}{2k_F}\left(k^2 - k_F^2\right) \ , \tag{2.10}$$

is drawn in Fig. 2.5. The particle-hole pair spectrum is easily constructed from the single particle spectrum and is also shown in Fig. 2.5. The characteristic feature of the particle-hole spectrum prohibiting the creation of quasiparticles is the empty regions indicated by arrows. As we have discussed, quasiparticles are sometimes described as electrons with a cloud of low-energy excitations around it and, since these low-energy particle-hole excitations do not exist in 1D, quasiparticles can not be created.

A final word before we go on. Interacting fermions, of course, exist even in one dimension, but they cannot form quasiparticles, and these interacting fermions must therefore be described using another theory than the Fermi liquid theory. The basis of such a theory, replacing the Fermi gas model, is the Tomonaga-Luttinger model where, as we shall see, certain interactions are included from the very beginning.

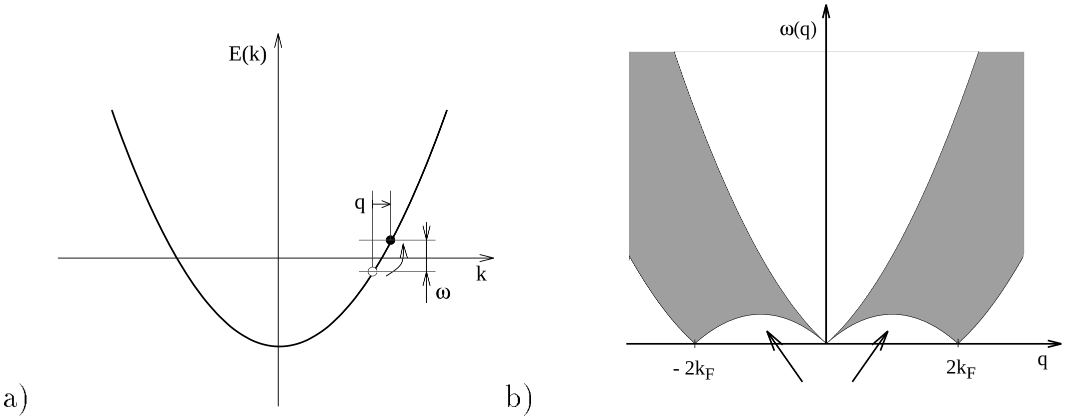


**Figure 2.5**: a) Single particle spectrum for a free Fermi gas. A particle-hole excitation is shown. b) Particle-hole pair spectrum derived from a). The arrows indicate the absence of low-energy excitations.

## 2.3 The spinful Tomonaga-Luttinger model: the core of the Luttinger liquid

We now introduce a simple solvable model, the Tomonaga-Luttinger model, which is the "center" of a new liquid theory replacing the Fermi gas. A closely related model, the Tomonaga model, was approximately solved by Tomonaga in 1950 [25][1]. Luttinger later found out [26] that a slight modification of the Tomonaga model made it exactly solvable, and in 1965 Mattis and Lieb [27] provided the correct solution of the model, nowadays termed the Tomonaga-Luttinger model (TLM).

What Tomonaga, Luttinger, and Mattis and Lieb did was to diagonalize the Hamiltonian in a rather straightforward way by means of fermion currents which can be described by bosons. To calculate single particle properties one needs a formula connecting the single fermions with the bosons, and in 1974 Mattis [28] and Luther and Peschel [29] independently found such a representation. Both of these representations contained a cut-off parameter rendering them exact operator identities only by a limiting procedure. Haldane [30] and Heidenreich et al. [31] later gave a precise formulation as an operator identity for a finite system on a ring of length $L$.

At the same time as Mattis, and Luther and Peschel worked on the TLM, some field theorist were working on the Thirring model. I will here cite a part of a paper by Coleman [32] from 1975 which reveals that at that time field theory and condensed matter theory were not at all as close as they are today:

> "..... Schroer has also pointed out that many of the results

[1] Sandwiched between the papers 'On the connection between spin and statistics' by W. Pauli and 'High energy nuclear events' by Enrico Fermi.

obtained here are in close correspondence with the result of the studies of one-dimensional electron gases by Luther and collaborators. Luther and I are in total agreement with Schroer on this point; we are also united in our embarrassment that we were incapable of reaching this conclusion unprompted. (Our offices are on the same corridor.)"

The same year Mandelstam was able to construct the Fermi field operator as a nonlocal function of the canonical Bose fields [33], and this kink-operator formalism is the basis for my presentation of Bosonization. But first, let us look at the TLM.

### 2.3.1 Presentation of the model

The early work on the Tomonaga-Luttinger model (in condensed matter physics) used a $k$-space formulation and several of the reviews that are available [30, 34, 35] also use this approach. I will here use another language, the field theory language, since I want to avoid any prejudices regarding the boundary conditions which are needed when doing a mode expansion (the standard $k$-space formulation assumes *periodic* boundaries). My main references here have been [36, 37, 38]. In this section I will restrict myself to interactions that can be solved for exactly, that is *forward scattering*, leaving *backscattering* and *Umklapp* for Sec. 2.4. For completeness I will consider spinful fermions, though.

The Hamiltonian of the TLM is

$$\begin{aligned} H_{TML} \;=\; \sum_{\sigma=\uparrow,\downarrow} \int dx \Big\{ & v_F \Big[ :\psi^\dagger_{L,\sigma}(x) i \frac{d}{dx} \psi_{L,\sigma}(x): - :\psi^\dagger_{R,\sigma}(x) i \frac{d}{dx} \psi_{R,\sigma}(x): \Big] + \\ & + g_{2\perp} J^\sigma_L(x) J^{-\sigma}_R(x) \;+\; g_{2||} J^\sigma_L(x) J^\sigma_R(x) + \\ & + g_{4\perp} (J^\sigma_L(x) J^{-\sigma}_L(x) + J^\sigma_R(x) J^{-\sigma}_R(x)) + \\ & + g_{4||} (J^\sigma_L(x) J^\sigma_L(x) + J^\sigma_R(x) J^\sigma_R(x)) \Big\} \end{aligned} \tag{2.11}$$

where $J^\sigma_{L/R} \equiv : \psi^\dagger_{L/R,\sigma} \psi_{L/R,\sigma}$ : are fermion currents and $: \cdots :$ denotes normal ordering. The normal ordering is an important part of the TLM. It is needed to take care of the filled Dirac seas that Luttinger introduced to make the model exactly solvable. This also makes $\psi_{L/R,\sigma}$, the left or right moving fields with spin $\sigma = \uparrow$ or $\downarrow$, fulfill fermionic anti-commutation relations:

$$\left\{ \psi_{L/R,\sigma}(x), \psi^\dagger_{L/R,\sigma'}(x') \right\} = \delta_{\sigma\sigma'} \delta(x - x'). \tag{2.12}$$

The first part of the Hamiltonian in Eq. (2.11) then describes free relativistic fermions with linear dispersion (see Fig. 2.6a). The interaction terms have

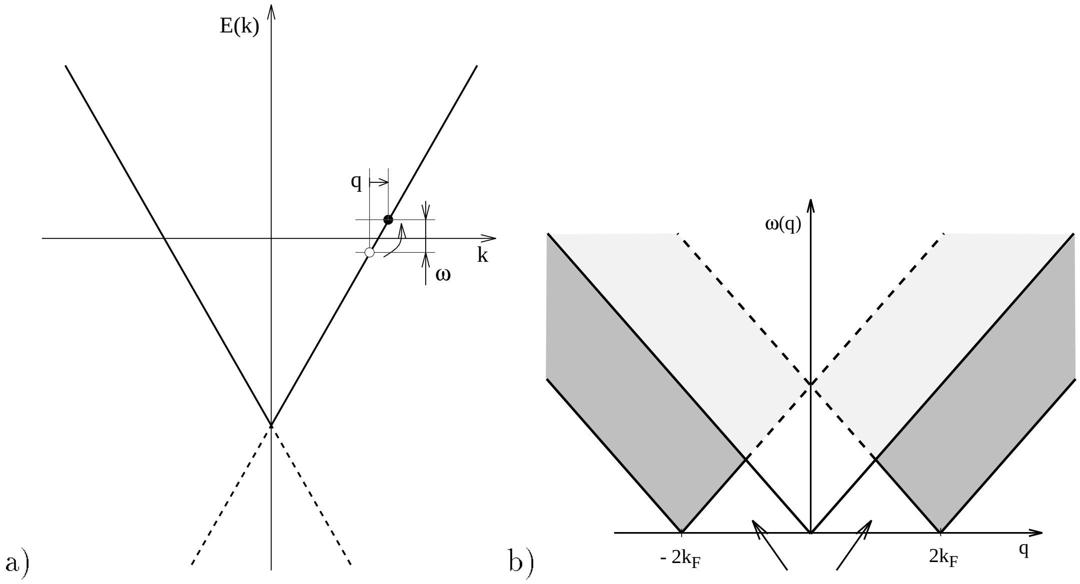


**Figure 2.6**: a) Single particle spectrum for free fermions with linear dispersion. A particle-hole excitation is shown. The dashed lines indicate filled "unphysical" states. b) Particle-hole pair spectrum derived from a). The arrows indicate the absence of low-energy excitations. The lighter areas indicate excitations involving unphysical states.

coupling constants indexed according to the "g-ology" scheme used by Sólyom in Ref. [34]. In Fig. 2.7 these terms are explained in a diagrammatic way.

It can be shown that the free part of the Hamiltonian can be rewritten in terms of the fermion currents,

$$:\psi^\dagger_{L,\sigma} i\frac{d}{dx}\psi_{L,\sigma}: - :\psi^\dagger_{R,\sigma} i\frac{d}{dx}\psi_{R,\sigma} = \pi(J^\sigma_L J^\sigma_L + J^\sigma_R J^\sigma_R)\,. \tag{2.13}$$

By the transformations

$$J_L^{c/s} \equiv \frac{1}{\sqrt{2}}\left(J_L^\uparrow \pm J_L^\downarrow\right) \tag{2.14}$$

$$J_R^{c/s} \equiv \frac{1}{\sqrt{2}}\left(J_R^\uparrow \pm J_R^\downarrow\right) \tag{2.15}$$

the Hamiltonian can be split into a charge current and a spin current part

$$H_{TLM} = H_c + H_s\,, \tag{2.16}$$

where each piece can be diagonalized by a Bogoliubov transformation. The spin-charge separation seen in Eq. (2.16) is a well-known signature of Luttinger liquid behavior. I will come back to this important feature of the TLM in Sec. 2.3.3.

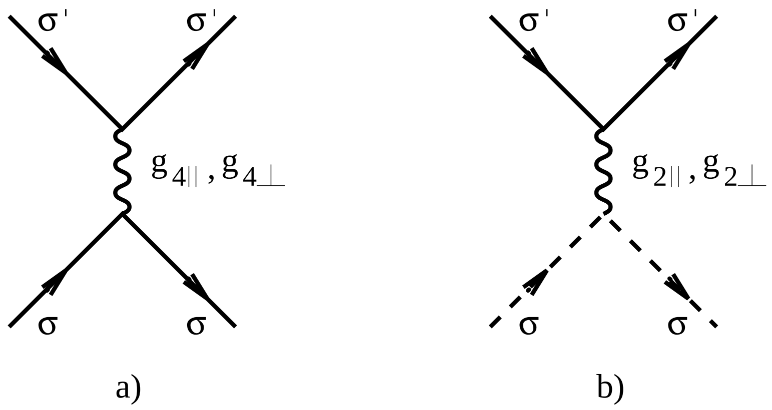


**Figure 2.7**: Forward scattering terms considered in the Tomonaga-Luttinger model. The full line represents the left (right) chiral field while the dashed line represents the right (left) chiral field. The spin indices are $\sigma, \sigma' =\uparrow, \downarrow$ and if $\sigma = \sigma'$ the couplings are $g_{i||}$ $(i = 2, 4)$ while if $\sigma \neq \sigma'$ they are $g_{i\perp}$.

As we can see we do not need bosonization for diagonalizing the Hamiltonian but, paradoxically as it may sound, connecting back to the fermions will be hard without using bosons! Specifically, we need to find a method for calculating correlation functions, such as the single particle (fermion) Green's function. Apart from making things easier and helping us in the calculations of single particle properties, bosonization is also conceptually very exciting. Indeed, representing fermions by bosons is a challenging idea, and Sidney Coleman, one of the pioneers of bosonization within field theory, in the acknowledgment of [32][2] thanks a colleague for reassuring him of his sanity!

## 2.3.2 Bosonization

We will now go through some basic bosonization methodology [39]. Basically, bosonization is nothing but a way of representing fermions in terms of bosons. As usual a faithful representation needs to conserve the commutation relations in order for the dynamics not to change via the Heisenberg equation of motion. In our case the Hamiltonian can be written in terms of the spin- and charge-currents. As long as other operators preserve their commutation relations with these currents when going from a fermionic to a bosonic representation, the dynamics will not change.

The commutation relation between the fermion currents can be shown to form the Kac-Moody algebra (for a review, see [40])

$$[J^{\sigma}_{L/R}(x), J^{\sigma}_{L/R}(x')] = \pm\frac{i}{2\pi}\partial_x\delta(x - x') \tag{2.17}$$

[2] I have already quoted another part of this reference on Page 23.

and, since the transformations in Eqs. (2.14) and (2.15) are canonical, the same commutation relations hold for $J_{L/R}^{c/s}$.

By introducing bosons $\bar{\phi}_{c/s}$ with conjugate momenta $\bar{\Pi}_{c/s}$,

$$[\bar{\phi}_{c/s}(x), \bar{\Pi}_{c/s}(x)] = i\delta(x - x'), \tag{2.18}$$

a straightforward calculation shows that

$$J_L^{c/s} \equiv \frac{1}{\sqrt{4\pi}} \left(\partial_x \bar{\phi}_{c/s} + \bar{\Pi}_{c/s}\right) \tag{2.19}$$

$$J_R^{c/s} \equiv \frac{1}{\sqrt{4\pi}} \left(\partial_x \bar{\phi}_{c/s} - \bar{\Pi}_{c/s}\right) \tag{2.20}$$

yield the same commutation relations as in Eq. (2.17).

If we were satisfied with only calculating quantities depending on the currents, we could stop here but in order to calculate single-particle properties we need—as we have already noted—to have a representation of the fermions in terms of the bosons in Eqs. (2.19) and (2.20).

Like any other operator, the chiral fermionic fields in Eq. (2.12) must preserve the commutation relations with the currents:

$$[\psi_{L/R,\sigma}(x), J_{L/R}^{\sigma}(x')] = \psi_{L/R,\sigma}(x)\delta(x - x'). \tag{2.21}$$

The magic formula

$$\psi_{L/R,\sigma}(x) = \frac{\eta_\sigma}{\sqrt{2\pi\alpha}} \exp\left(\mp 2\pi i \int_{-\infty}^{x} J_{L/R}^{\sigma}(y)dy\right) \tag{2.22}$$

where $\eta_\sigma$ obeys $\{\eta_\uparrow, \eta_\downarrow\} = 0$ and $\eta_\sigma^2 = 1$ (and is there to assure the right anti-commutation relations between operators with different spin $\sigma$), yields the same commutation relations as in Eq. (2.21) while at the same time yielding the required anti-commutation relations in Eq. (2.12). The required relation between the fermions and the bosons is then obtained by the use of Eqs. (2.19) and (2.20). The factor $\alpha$ is a cut-off factor which has the dimension of length.

Before we write the final version of the magic formula, let us elaborate a bit on the bosons. In terms of the boson fields in Eqs. (2.19) and (2.20) the Hamiltonian in Eq. (2.16) is given by

$$H_{TLM} = \sum_{\nu=s,c} \int dx \left\{ \frac{\bar{v}_\nu}{2} \left[(\partial_x \bar{\phi}_\nu)^2 + \bar{\Pi}_\nu^2\right] + \frac{g_\nu}{4\pi} \left[(\partial_x \bar{\phi}_\nu)^2 - \bar{\Pi}_\nu^2\right] \right\} \tag{2.23}$$

with

$$\bar{v}_c = v_F + \frac{g_{4\|}}{\pi} + \frac{g_{4\perp}}{\pi}, \qquad g_c = g_{2\|} + g_{2\perp}, \tag{2.24}$$

$$\bar{v}_s = v_F + \frac{g_{4\|}}{\pi} - \frac{g_{4\perp}}{\pi}, \qquad g_s = g_{2\|} - g_{2\perp}, \tag{2.25}$$

A rescaling of the bosons by a canonical transformation (Bogoliubov transformation):

$$\bar{\phi}_\nu = K_\nu \phi_\nu, \quad \bar{\Pi}_\nu = \Pi_\nu / K_\nu, \tag{2.26}$$

gives

$$H_{TLM} = \sum_{\nu=s,c} \int dx \left\{ \frac{v_\nu}{2} \left[ (\partial_x \phi_\nu)^2 + \Pi_\nu^2 \right] \right\}. \tag{2.27}$$

This is the Hamiltonian of free bosons, one free boson for each channel $\nu$, with effective velocities given by

$$v_\nu = (\bar{v}_\nu + \frac{g_\nu}{2\pi}) K_\nu^2 \,, \qquad K_\nu^2 = \sqrt{\frac{\bar{v}_\nu - \frac{g_\nu}{2\pi}}{\bar{v}_\nu + \frac{g_\nu}{2\pi}}} \,. \tag{2.28}$$

The corresponding Lagrangian density is given by

$$\mathcal{L} = \sum_{\nu=s,c} \left\{ \frac{v_\nu}{2} \left[ (\partial_{v_\nu t} \phi)^2 - (\partial_x \phi)^2 \right] \right\} \tag{2.29}$$

where $\partial_{v_\nu t} \equiv \frac{1}{v_\nu} \partial_t$, and with canonical momentum

$$\Pi_\nu \equiv \frac{\partial \mathcal{L}}{\partial \dot{\phi}_\nu} = \partial_{v_\nu t} \phi_\nu \,. \tag{2.30}$$

Expressing the resulting Euler-Lagrange equations, i.e. the Klein-Gordon equations, in terms of $\partial_\pm = \partial_x \pm \partial_{v_\nu t}$,

$$(\partial_{v_\nu t}^2 - \partial_x^2) \phi_\nu = \partial_+ \partial_- \phi_\nu = 0 \,, \tag{2.31}$$

we note that that the two solutions can be written in terms of left- and right moving bosons, $\phi_{\nu,L}(x + v_\nu t)$ and $\phi_{\nu,R}(x - v_\nu t)$. We use the combination $\phi_\nu(x,t) = \phi_{\nu,L}(x + v_\nu t) + \phi_{\nu,R}(x - v_\nu t)$ and its dual field $\tilde{\phi}_\nu(x,t) = \phi_{\nu,L}(x + v_\nu t) - \phi_{\nu,R}(x - v_\nu t)$. The field and the dual field are then related by

$$\partial_x \phi_\nu = \partial_{v_\nu t} \tilde{\phi}_\nu \,, \qquad \partial_x \tilde{\phi}_\nu = \partial_{v_\nu t} \phi_\nu \,. \tag{2.32}$$

Collecting our results, we can write down our final version of the magic formula:

$$\psi_{L/R,\sigma}(x) = \frac{\eta_\sigma}{\sqrt{2\pi\alpha}} \prod_{\nu=c,s} \exp\left( i\epsilon_{\nu,\sigma} \sqrt{\frac{\pi}{2}} \left( \mp K_\nu \phi_\nu(x) - K_\nu^{-1} \tilde{\phi}_\nu(x) \right) \right), \tag{2.33}$$

with $\epsilon_{\nu,\sigma} = 1$ unless $\nu = s$ and $\sigma = \downarrow$, when it is equal to $-1$, in which version we have used the duality relation $\Pi_\nu \equiv \partial_{v_\nu t} \phi = \partial_x \tilde{\phi}$.

In order to perform calculations using this formula one needs a mode expansion of the bosons. This will be illustrated in Chapter 3.

### 2.3.3 Properties of the TLM: no quasiparticles but spin-charge separation

With the use of the magic formula, Eq. (2.33), one can, in principle, calculate *any* correlation function, the only problem being how to perform the calculations in practice! With knowledge of the correlation functions, *all* properties of a model can be investigated within the linear response theory, and over the years a number of different properties of the TLM have been investigated in this way. Needless to say, I will not discuss all of these properties. Instead I choose to present some of those that are particularly interesting, as they clearly show the difference between a Luttinger liquid and a Fermi liquid at the same time as they are related to my own work.

At this point one may ask why we should at all bother about the physics of interacting fermions in one dimension, the Luttinger liquid, when the experimental, observable physics of "real" interacting fermions takes place in 3D, the kind of world we inhabit? The answer is that, although in an experimental situation the electrons are never purely one-dimensional, we still hope that the Luttinger liquid model can explain the experimental outcome if the system we are looking at is *effectively* one-dimensional (like the quasi-1D organic conductors or the edge excitations in the fractional quantum Hall effect, to be discussed below). More ambitiously, there are also hopes that, by studying the one-dimensional Luttinger liquid, we may gain insight into how to construct a similarly powerful theory in dimensions larger than one, which could explain the non-Fermi liquid behavior seen in many systems [41], most intriguingly in the high-$T_c$ superconductors.

As I have pointed out before, we usually need a mode expansion to be able to do explicit calculations. The results to be discussed are derived for infinite or periodic systems. In our work, in contrast, we consider another type of system with *open boundaries* but we leave the discussion of this to Chapter 3. In this section I will restrict my attention to the differences between Luttinger liquids and Fermi liquids, as seen in the momentum distribution and spectral function already introduced in Sec. 2.1.

The single-particle Green's function, $G_{L/R}(x,t;x',t') = \langle \psi^\dagger_{L/R,\sigma}(x,t)\psi_{L/R,\sigma}(x',t')\rangle$ has been calculated for a bulk system by numerous people (see for example [35, 38, 37]). The result is (adapted to our notation)

$$G_L(x,t;0,0) \propto \prod_{\nu=c,s} (v_\nu t + x - i\alpha)^{-\frac{(K_\nu + K_\nu^{-1})^2}{8}} (v_\nu t - x - i\alpha)^{-\frac{(K_\nu - K_\nu^{-1})^2}{8}} \quad (2.34)$$

where $v_\nu$ and $K_\nu$ are defined in Eq. (2.28) and $G_R(x,t;x',t') = G_L(-x,t;-x',t')$. Note the small cut-off factor $\alpha$ which can be seen as the smallest length in the system, or equivalently, as the largest allowed momentum. It will eventually be set to zero but we have kept it finite here to keep track of the phase of the Green's function.

From the Green's function in Eq. (2.34) the momentum distribution function can be derived [42, 43]. Close to the the positive Fermi point, $k_F$, one finds

$$n(k_F + k) \sim \frac{1}{2} - C_1 \mathrm{sign}(k)|k|^\alpha - C_2 k \ , \tag{2.35}$$

where the amplitudes $C_1$ and $C_2$ can be calculated exactly [43]. The famous bulk exponent, usually just denoted by $\alpha$ as in Eq. (2.35) (not to be mixed up with the small cut-off in Eq. (2.34)), is given by

$$\alpha \equiv \frac{(K_c^2 + K_c^{-2} + K_s^2 + K_s^{-2})}{4} - 1 \ . \tag{2.36}$$

The momentum distribution is sketched in Fig. 2.8 and can be compared with the distributions for free fermions and interacting fermions described by the Fermi liquid theory in Fig. 2.1. For the non-interacting TLM we have $C_2 =$

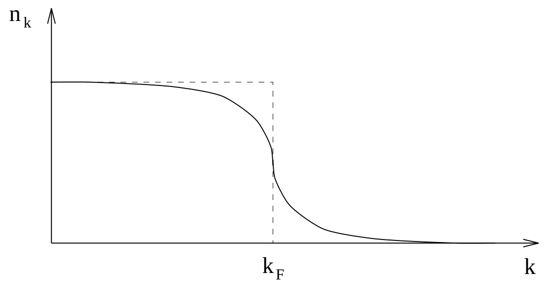


**Figure 2.8**: Momentum distribution function for interacting fermions in the TLM.

0 and $\alpha = 0$ and we recover the free fermion distribution function as was expected.

What about the quasiparticles then? As we saw in Sec. 2.1 a signature of quasiparticles (as we know them from Fermi liquid theory) is the jump in the momentum distribution of the fermions at the chemical potential, the quasiparticle residue $Z_{k_F}$ (see Fig. 2.1). As seen in Fig. 2.8 (cf. also Eq. (2.35)) this discontinuity does not exist for interacting fermions in one dimension.

As we pointed out in Sec. 2.2, the nonexistence of quasiparticles in 1D is entirely due to the properties of the particle-hole pair spectrum. The analysis leading up to this spectrum in Fig. 2.5 was based on the quadratic free fermion spectrum. In the TLM, the spectrum of the fermions is linear, as shown in Fig. 2.6a. The corresponding particle-hole spectrum in Fig. 2.6b shows the same absence of low-energy excitations, thus prohibiting the formation of quasiparticles by the same argument as before.

The absence of quasiparticles also manifests itself in the spectral function defined in Eq. (2.7). Voit has done some beautiful numerical work on the spectral function [44, 43, 35] and Fig. 2.9 is taken from his review [35]. Meden and Schönhammer have also done recent work on the spectral function [45, 46, 47],

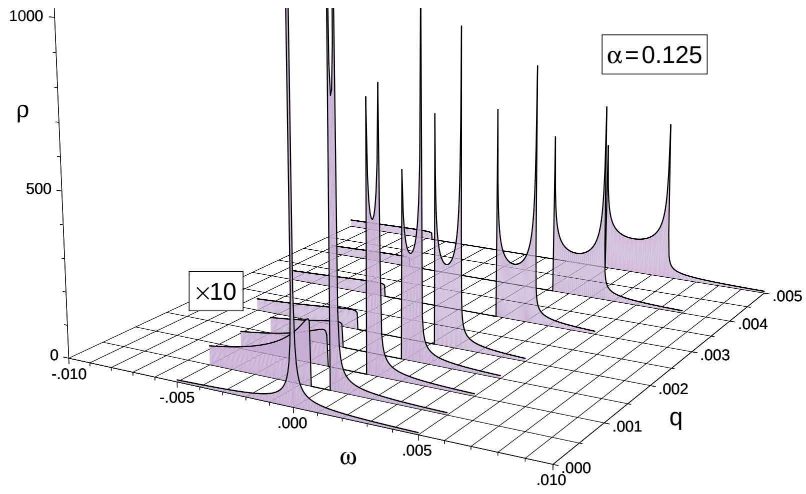


**Figure 2.9**: Spin charge separation seen in the spectral function of the TLM (from Ref. [35]). The positions of the peaks and the edges are determined by the spin and charge velocities, $v_s < v_c$. The structure is discussed in the text. (To be compared with Fig. 2.2)

specifically incorporating temperature effects (see Sec. 3.3.2). In Fig. 2.9 we clearly see the spin charge separation manifested as a the double-peak structure. The tails fall off with power laws where the exponents are functions of the $K_\nu$'s. The double peak structure remains even if we turn off the interaction between left and right branches, $g_{2\perp} = g_{2||} = 0$, in contrast to the shallow bump at negative energies originating from these interactions. A similar structure is seen in the Fermi liquid spectral function in Fig. 2.2. The absence of quasiparticles, or equivalently, low-energy excitations, is manifest in the gap between the positive and negative energy structures. The asymmetry of the gap relative to the Fermi energy, $\omega = 0$, is simply a consequence of the $SU(2)$-invariance that predicts that $K_s = 1$ (see Sec. 2.4.3), or equivalently, $g_s = 0$, making the spin-channel non-interacting, i.e. the spin-channel bump at negative energies vanishes.

The integrated spectral density,

$$N(\omega) = \int_{-\infty}^{\infty} dk \rho(k, \omega) \ , \tag{2.37}$$

(also derivable from the Green's function in Eq. (2.34), cf. Eq. (3.23)) shows the scaling behavior [48, 43, 47]

$$N(\omega) \propto |\omega|^\alpha \ , \tag{2.38}$$

for low energies $\omega$, with $\alpha$ given in Eq. (2.36).

The momentum distribution can also be derived from the spectral function:

$$n(k) = \int_{-\infty}^{\infty} d\omega f_{FD}(\omega)\rho(k,\omega) \ . \tag{2.39}$$

Some of the main features of the momentum distribution $n(k)$ can be seen from this formula. If $T = 0$ the Fermi-Dirac distribution turns to a step function effectively reducing the integration to negative $\omega$ only. For the non interacting case the integration will be over a $\delta$-function for negative $k$ and vanish for positive $k$, yielding the ordinary free fermion step function momentum distribution in Fig. 2.1. Turning on interaction moves spectral weight from positive to negative energies, as can be seen in Fig. 2.9. This redistribution of spectral weight is less pronounced for large $k$. However, as $k$ approaches the Fermi wave vector, the deviation from the non-interacting step function becomes clear. Since the $\delta$-function peak gets smeared symmetrically by interactions at $k_F$, half of the spectral weight will be included in the integration at $k_F$, giving $n(k_F) = 1/2$.

Note that the spin-charge separation seen so clearly in Fig. 2.9 is not seen in the momentum distribution, nor in the spectral density. To probe the spin-charge separation we need to consider quantities depending on *both* energy and momentum [35], such as the spectral function, which can be experimentally probed in angle-resolved photoemission spectroscopy (ARPES) (see Sec. 2.5.2).

## 2.4 Lattice model realizations of Luttinger liquids

There are several theoretically interesting systems that can be mapped onto the TLM under suitable conditions. Examples include the low-energy physics of the Heisenberg spin-$\frac{1}{2}$ chain [50] and the low-energy limit of the Hubbard model [10]. The latter we have used as an example in Papers I and II, and I will therefore consider it in some detail in Secs. 2.4.1 and 2.4.4. In Sec. 2.4.1 I present the Hubbard model and its low-energy limit. The low-energy Hamiltonian will consist of two parts; one that we recognize as the TLM and the other consisting of backscattering and Umklapp terms. These processes are considered in some detail in Sec. 2.4.2 where we also examine other possible processes *not* included in the TLM. To be able to map the low-energy limit of the Hubbard model onto the TLM we need to use the renormalization group technique. The ideas behind renormalization are presented in brief in Sec. 2.4.3 where I use the percolation model as a caricature example. Finally, in Sec. 2.4.4, I discuss how the renormalization group is used to map the low-energy limit of the Hubbard model onto the TLM.

### 2.4.1 The Hubbard model: the low-energy limit

The Hubbard model is the simplest possible model showing both antiferromagnetic correlations and electron transport behavior. This highly simplified model of a correlated metal has resisted solution except in the limits of one or infinite dimensions [10]. The model Hamiltonian is:

$$H = -t \sum_{i,\sigma} (c^\dagger_{i,\sigma} c_{i+1,\sigma} + c^\dagger_{i+1,\sigma} c_{i,\sigma}) + U \sum_i n_{i,\uparrow} n_{i,\downarrow} \ , \qquad (2.40)$$

where $i = 1, 2, \dots$ is a site index, $\sigma = \uparrow, \downarrow$ a spin index, and $n_{i,\sigma} = c^\dagger_{i,\sigma} c_{i,\sigma}$ the number operator. The first part, the hopping term, governed by the parameter $t$, is the band (delocalized) part, making the Hubbard model show metallic transport properties when $t \gg U$. The second part, governed by the parameter $U$, is an on-site interaction, modeling a screened Coulomb interaction between the electrons.

The Hubbard model is considered a standard model for electron transport in narrow-band materials like, for example, the transition metal oxides. It has been studied extensively over the years and I will not go into any detail here. Instead I will restrict myself to pointing out two important results that have implications for our work and that also show the Hubbard model to be a good realization of a Luttinger liquid.

First, the one-dimensional Hubbard model can be diagonalized by a *Bethe Ansatz* [51], and the energy spectrum and the thermodynamics are known exactly for this case. The wave functions, though, obtained by the exact Bethe Ansatz solution are so complicated that the expectation values or correlation functions are inaccessible via this solution. We will see, however, that a detour by the TLM will allow us to reach the correlation functions without using these wave functions.

Secondly, the low-energy limit of the Hubbard model in one dimension can be mapped onto the TLM. The low-energy limit is obtained, within perturbation theory, by treating $U/t$ as a small perturbation. The unperturbed model, $U = 0$, produces a tight-binding band spectrum, $\epsilon(k) = -2t \cos ak$, where $a$ is the lattice spacing. Expanding the electron operators at the Fermi points, $\pm k_F$,

$$c_{i,\sigma} = e^{-ik_F na} c_{L,i,\sigma} + e^{ik_F na} c_{R,i,\sigma} \ , \qquad (2.41)$$

and going to the continuum limit,

$$c_{L/R,i,\sigma} \sim \sqrt{\frac{a}{2\pi}} \psi_{L/R,\sigma} \ , \qquad (2.42)$$

one obtains

$$H = \sum_{\sigma=\uparrow,\downarrow} \int dx \left\{ v_F \left[ :\psi^\dagger_{L,\sigma}(x) i \frac{d}{dx} \psi_{L,\sigma}(x): - :\psi^\dagger_{R,\sigma}(x) i \frac{d}{dx} \psi_{R,\sigma}(x): \right] + \right.$$

$$
\begin{aligned}
&+ \frac{g}{2} \sum_{k,l=L,R} :\psi^\dagger_{k,\sigma}(x)\psi_{k,\sigma}(x)::\psi^\dagger_{l,-\sigma}(x)\psi_{l,-\sigma}(x): + \\
&+ \; g \; :\psi^\dagger_{R,\sigma}(x)\psi_{L,\sigma}(x)\psi^\dagger_{L,-\sigma}(x)\psi_{R,-\sigma}(x): + \\
&+ \; \left[ g e^{i2\pi x n_e} \; :\psi^\dagger_{L,\sigma}(x)\psi_{R,\sigma}(x)\psi^\dagger_{L,-\sigma}(x)\psi_{R,-\sigma}(x): + \text{h.c.} \right] \Bigg\} ,
\end{aligned} \tag{2.43}
$$

where $v_F = 2ta\sin(n_e\pi/2)$, $g = Ua/2\pi$ and $n_e = \frac{2ak_F}{\pi}$.

The electron operator $c_{i,\sigma}$, defined on the lattice, is replaced in the continuum by the electron field in the same way as the lattice operators in Eq. (2.42) are connected to the chiral fields. The electron field is thus related to the chiral field according to

$$
\Psi_\sigma(x) = e^{-ik_Fx}\psi_{L,\sigma}(x) + e^{ik_Fx}\psi_{R,\sigma}(x). \tag{2.44}
$$

as seen from Eq. (2.41).

We recognize the first part of the low-energy Hubbard Hamiltonian in Eq. (2.43) as the TLM in Eq. (2.11), with $g_{2\perp} = 2g_{4\perp} = g$ and $g_{2\|} = 2g_{4\|} = 0$ while the last part, i.e. the backscattering and Umklapp terms, is new, prohibiting a direct mapping onto the TLM. Fortunately, however, there is a method to treat the backscattering and Umklapp terms. This is the renormalization group method but in order to use it we need to include *all* possible terms in the Hamiltonian since couplings that initially are zero can acquire finite values in the renormalization process. In the following subsections I will first present the general Hamiltonian and then discuss how the backscattering and Umklapp terms can be treated. (Note that as long as we do not explore a half-filled system, i.e. a system with an equal number of electrons and sites ($n_e = 1$), Umklapp processes are averaged to zero already in the "bare" theory, due to rapid phase oscillations.) We will return to the Hubbard Hamiltonian in Sec. 2.4.4.

### 2.4.2 Backscattering and Umklapp

As seen in Sec. 2.3.1, forward scattering processes are already included in the TLM while backscattering and Umklapp are not. These processes are schematically shown in Fig. 2.10 and can be written as

$$
H_{1\|} = \sum_{\sigma=\uparrow,\downarrow} \int dx \, g_{1\|} : \psi^\dagger_{L,\sigma}(x)\psi_{R,\sigma}(x)\psi^\dagger_{R,\sigma}(x)\psi_{L,\sigma}(x) : \tag{2.45}
$$

$$
H_{1\perp} = \sum_{\sigma=\uparrow,\downarrow} \int dx \, g_{1\perp} : \psi^\dagger_{L,\sigma}(x)\psi_{R,\sigma}(x)\psi^\dagger_{R,-\sigma}(x)\psi_{L,-\sigma}(x) : \tag{2.46}
$$

$$
H_{3\|} = \sum_{\sigma=\uparrow,\downarrow} \int dx \, g_{3\|} : \psi^\dagger_{L,\sigma}(x)\psi_{R,\sigma}(x)\psi^\dagger_{L,\sigma}(x)\psi_{R,\sigma}(x) : + \text{h.c.} \tag{2.47}
$$

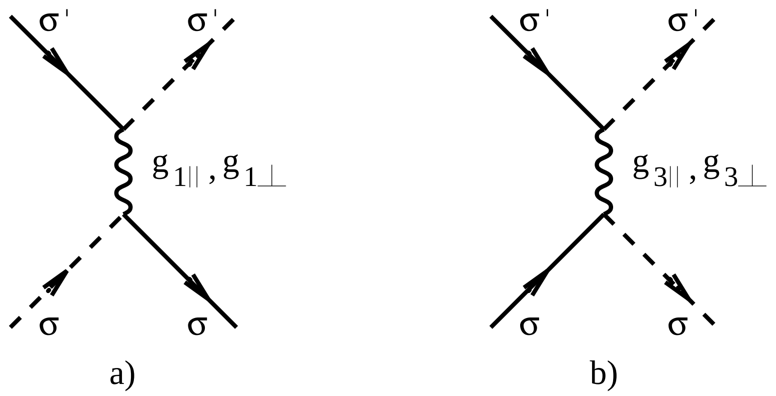


**Figure 2.10**: a) Backscattering and b) Umklapp processes. The full line represents the left (right) chiral field while the dashed line represents the right (left) chiral field. The spin indices are $\sigma, \sigma' =\uparrow, \downarrow$ and if $\sigma = \sigma'$ the couplings are $g_{i||}$ $(i = 1, 3)$ while if $\sigma \neq \sigma'$ they are $g_{i\perp}$.

$$H_{3\perp} = \sum_{\sigma=\uparrow,\downarrow} \int dx\, g_{3\perp} : \psi^\dagger_{L,\sigma}(x)\psi_{R,\sigma}(x)\psi^\dagger_{L,-\sigma}(x)\psi_{R,-\sigma}(x) : +\text{h.c.} \quad (2.48)$$

The $g_{1||}$-terms are equal to the $g_{2||}$-terms in the exactly solvable Tomonaga-Luttinger Hamiltonian in Eq. (2.11) and can therefore be taken into account by letting $g_{2||} \to g_{2||} - g_{1||}$, while the $g_{3||}$-terms are precluded due to the Pauli principle. Left are the $g_{1\perp}$- and $g_{3\perp}$- terms which can both be rewritten by the use of the bosonization formula in Eq. (2.33) with the result

$$H_{1\perp} = \frac{2g_{1\perp}}{(2\pi\alpha)^2} \int dx \, \cos\left(\sqrt{8\pi} K_s \phi_s(x)\right) , \quad (2.49)$$

$$H_{3\perp} = \frac{2g_{3\perp}}{(2\pi\alpha)^2} \int dx \, \cos\left(\sqrt{8\pi} K_c \phi_c(x)\right) . \quad (2.50)$$

Note that the backscattering and Umklapp contributions to the Hamiltonian are spin-charge separated from the very beginning. The general Hamiltonian becomes

$$H = H_{TLM} + H_{1\perp} + H_{3\perp} , \quad (2.51)$$

with $H_{TLM}$ given in Eq. (2.27). We note that since the spin and charge channels of the general Hamiltonian in Eq. (2.51) are symmetric, only one channel needs to be explicitly considered. The result for the other channel can be obtained simply by changing the indices, $c \leftrightarrow s$, in the result from the first.

As already announced, to treat the backscattering and Umklapp terms introduced in the Hamiltonian we need to use renormalization group techniques. So, let me pause here and very briefly introduce some of the key ideas behind this remarkable method.

### 2.4.3 Renormalization

The Renormalization group method is one of the most important methods in theoretical physics developed during the last twenty-five years [52] and in 1982 Kenneth Wilson was honored with the Nobel prize for his contribution to the development of this method [53].

To give the main ideas of the renormalization group technique I will first consider a conceptually very simple model, the percolation model, totally different from the Hamiltonian systems we have considered so far. We will see that the renormalization group idea reveals an underlying universality and that this universality idea can easily be transmitted to the systems we have studied even though these systems do not have much in common with the percolation system.

Let us consider metallic and non metallic spheres arranged in a two-dimensional triangular way (closed packed) in a box (see Fig. 2.12). Under which conditions will we be able to transmit an electrical current from one box-side to the opposite side? This is only possible if we have metallic spheres in an (perhaps winding) unbroken array from one side to the other, that is, if we have percolation. Let us introduce the probability $p$ that a site is occupied by a metallic sphere. For a large system (many spheres) this probability is the same as the percentage of the total number of spheres that are metallic. The main feature of the model that we are interested in is for which probabilities $p$ the system is percolating.

The idea of renormalization is to attack the problem locally by averaging out irrelevant information, only keeping the relevant one. That there is irrelevant information is obvious if one considers that many features measured in an experiment are sample independent even though two samples cannot be identical. Some of the parameters that fully describe the sample must therefore be irrelevant and this is the very foundation of science, that by identifying relevant parameters you can explain certain details in real life.

In the percolation problem on a triangular lattice the relevant information is whether the system percolates locally, that is, if, in a group of three nearby spheres (forming a cell), there are at least two metallic spheres, which thereby span the cell, see Fig. 2.11. By successively replacing each percolating cell

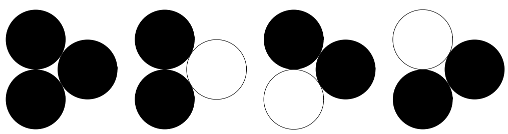

**Figure 2.11**: Percolating cells.

of three spheres with a (larger) metallic sphere, and the non-percolating cells with non-metallic spheres, a series of transformations of the initial problem can be made. In Fig. 2.12 we see how a series of transformations of the initial problems (having $p = 0.4$ and $p = 0.6$ respectively) converges to $p^* = 0$ (non-percolating) and $p^* = 1$ (percolating) respectively.

Somewhere in between $p = 0.4$ and $p = 0.6$ there must be a critical probability $p_c$ dividing the parameter space, $0 \leq p \leq 1$, and thereby the outcome of a percolation experiment, into two parts: percolation for $p > p_c$ and no percolation for $p < p_c$. Of course this is true only in a statistical sense and exactly valid only in the limit of an infinitely large system.

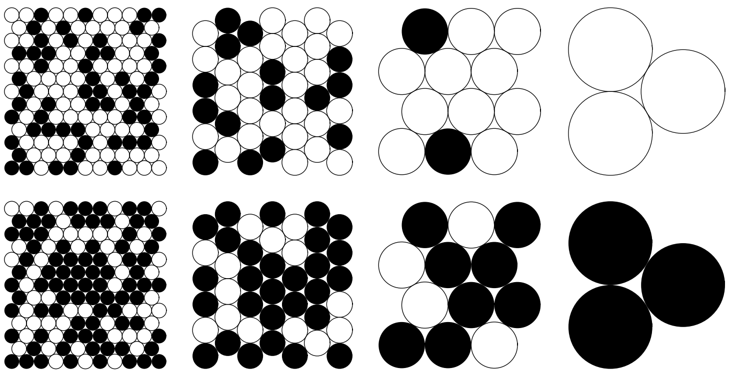

**Figure 2.12**: Renormalization of a percolation system at $p = 0.4$ (top row) and $p = 0.6$ (bottom row). Under renormalization $p$ flows towards the fixed points $p^* = 0$ and $p^* = 1$ respectively.

For the percolation problem on a triangular lattice the critical probability (density) is easily obtained by statistics. For a cell of three spheres to conduct current (i.e. percolate) we can have three metallic spheres or two metallic and one non-metallic sphere in three different configurations (see Fig. 2.11). This leads to the new probability $p'$ of the whole cell to be percolating,

$$p' = p^3 + 3p^2(1-p) \ . \tag{2.52}$$

There are three possibilities that the initial probability $p$ remains, $p' = p = p^*$, $p^* = 0, 1/2$, and 1. These points in parameter space are the fixed points and, as we saw in Fig. 2.12, $p^* = 0$ and 1 must be stable fixed points while $p^* = 1/2$ is an unstable fixed point. It is customary to describe the behavior under renormalization by a map in parameter space as in Fig. 2.13. We say that

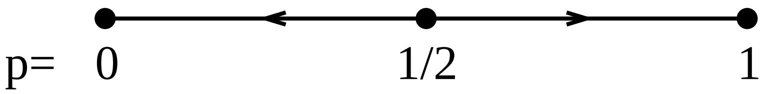


**Figure 2.13**: Renormalization flow for the percolation on a triangular lattice.

the system belongs to different universality classes depending on whether the system percolates or not, i. e. whether $p$ is greater or less than $p_c$.

We will soon see that a system described by the Hamiltonian in Eq. (2.51) also belongs to different universality classes depending on the values of the parameters $g_{1\perp}$ ($g_{3\perp}$) and $g_s$ ($g_c$) in Eq. (2.25)((2.24)).

As a last comment I want to emphasize that even though renormalization is a wonderful tool we have to pay a prize when using it. The detailed information contained in the original model gets lost under renormalization leaving only the leading behavior. In this respect renormalization is an irreversible process. In our example, the detailed information on the percolation model, for example, the path that the percolation (current) follows, is lost and only the overall behavior, percolation or not, is retained. When we now return to the Hubbard model we will see that under renormalization only information on the physics on large scales is retained. This means that, by this method, we have only access to the long-time, long-distance behavior (or equivalently the small momenta, low-energy physics) of the original lattice Hubbard model.

### 2.4.4 The Hubbard model: a Luttinger liquid

Now, let us return to the Hamiltonian in Eq. (2.51). When applying the renormalization group technique to a Hamiltonian system it is convenient to examine the partition function $Z = \langle \exp(-\beta H) \rangle$ since all correlation function can be derived from it (see for example [54, 55]). As already mentioned, the symmetry between the spin and charge channels permits us to examine only one of the channels, say the spin-channel (with the backscattering term). By treating the backscattering term as a perturbation Chui and Lee [56] mapped this system onto a system treated earlier by Kosterlitz and Thouless [57, 58]; the two-dimensional classical plasma consisting of an equal number of positively and negatively charged particles interacting with the logarithmic Coulomb potential. There are several other approaches to the renormalization group on the TLM, see for example [34].

It is found that the spin-channel part of the Hamiltonian in Eq. (2.51) gives rise to renormalization group equations as in Ref. [57], the Kosterlitz-Thouless renormalization group equations. The corresponding renormalization flow diagram is shown in Fig. 2.14. (Remember that these equations are derived within the perturbation theory and thereby only valid for small $g_{1\perp}$.) From Fig. 2.14 we conclude that the long distance, low energy physics of a system with parameters $g_{1\perp}$ and $g_s$ is the same as for a system with parameters $g'_{1\perp}$ and $g'_s$ *lying on the same trajectory.* In particular we find that the long distance, low energy physics of a system with parameters $g_{1\perp}$ and $-g_s \le |g_{1\perp}|$ is the same as for a system described by the TLM Hamiltonian *but with renormalized parameter* $-g_s \to -g_s^* = \sqrt{g_s^2 - g_{1\perp}^2}$. Systems that, in this way, can be mapped on the TLM are called *Luttinger liquids* in analogy with Fermi liquids that can be mapped on the Fermi gas, also by a renormalization group procedure [59].

From Fig. 2.14 we can also draw the important conclusion that the TLM

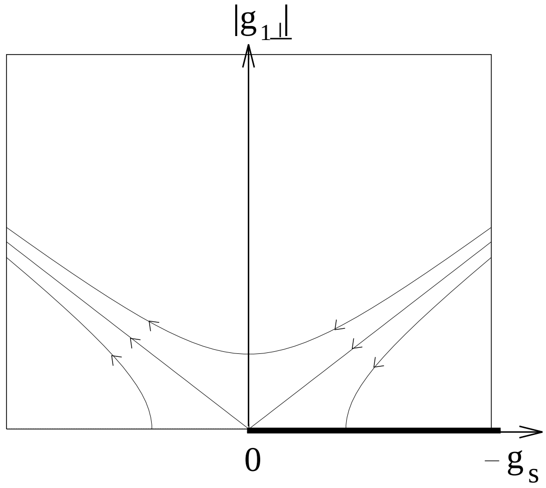


**Figure 2.14**: The renormalization flow for the spin-channel, in the parameter space of $g_{1\perp}$ and $g_s$. The thick line indicates the fixed line of the system, the TLM with $g_s \leq 0$.

is unstable to $g_{1\perp}$-interactions if $g_s > 0$. We also see that there are no single fixed *points* in Fig. 2.14, only a fixed line. This fixed line structure in the renormalization flow makes the exponents in the correlation functions non-universal, that is, dependent on the interaction parameters $g_{i,\perp}$ and $g_{i\|}$, $i = 1, 2, 3, 4$. This is in contrast to the Fermi liquid case where a renormalization flow analysis only reveals fixed points giving universal, integer exponents. This is yet another difference between Luttinger liquids and Fermi liquids.

The above mapping of the spin-channel part of the Hamiltonian onto the TLM (and thereby also the charge-channel part by the substitution $c \leftrightarrow s$) gives us the opportunity to calculate correlations functions also for systems with backscattering and Umklapp terms. Returning to the Hubbard model (Eq. (2.40)), renormalization allows us to extract the correlation functions (see Sec. 2.3.3) rather easily, at least compared to the prohibitively difficult task of using the wave functions of the exact *Bethe Ansatz* solution. However, the correlation functions determined by the combined use of bosonization and the renormalization group are only valid for low energy and small momenta. As experiments are typically carried out in these regimes, this is not, however, a serious constraint.

As we saw in Sec. 2.3.3 the correlation functions will depend on the four parameters $v_c$, $v_s$, $K_c$, and $K_s$, which in turn depend on the Fermi velocity, $v_F$, and the coupling constants $g_\nu$, $g_{4,\perp}$, and $g_{4\|}$ (see Eq. (2.28)). In Sec. 2.4.1 we gave the values of the parameters for the low-energy limit of the Hubbard model, derived within perturbation theory (with $U$ small), and from Eq. (2.25) we obtain $g_s = -g$ ($g \propto U$). We also obtain $g_c = g$ which implies that the charge channel is unstable to Umklapp processes: systems described by the

Hubbard model open up a gap in the charge channel in the presence of Umklapp. These systems cannot be described by the TLM and we thus restrict ourselves to the Hubbard model away from half-filling so that the Umklapp term can be safely neglected. By noting that $g_{1\perp} = g$ and $-g_s = g$ we conclude, from Fig. 2.14, that under renormalization $-g_s \rightarrow -g_s^* = 0$. From Eq. (2.28) and the parameters in Sec. 2.4.1 we obtain the appropriate values of the parameters describing the low-energy Hubbard model away from half-filling: $K_s^2 = 1$, $v_s = v_F - \frac{g}{2\pi}$, $K_c^2 = (1 + \frac{g}{\pi v_F})^{-1/2}$, and $v_c = (v_F + \frac{g}{\pi})K_c^2$. The parameters $g$ and $v_F$ are functions of the original lattice Hamiltonian parameters $U$ and $t$, and of the filling factor $n_e$, These are given in Sec. 2.4.1.

In the low-$U$ limit, perturbation theory can provide the values of $v_\nu$ and $K_\nu$, but for large $U$, perturbation theory breaks down. Since the exact solution of the Hubbard model shows no phase transition as $U > 0$ grows, one assumes that the low-energy properties of the large $U$ Hubbard model is also described by the TLM, that is, that the large $U$ Hubbard model is also a Luttinger liquid [60]. The parameters $v_\nu$ and $K_\nu$ must now be calculated nonperturbatively. One can show that the $SU(2)$-invariance of the Hamiltonian requires $g_s^* = 0$, thus giving $K_s = 1$. From the exact Bethe Ansatz solution, the three other

**Figure 2.15**: a) The charge and spin velocities $v_c$ (full line) and $v_s$ (dash-dotted line) for the Hubbard model as a function of band filling for different values of $U/t$: $U/t = 16, 8, 4, 2, 1$ for $v_c$, from top to bottom in the left part of the figure, and $U/t = 1, 2, 4, 8, 16$ for $v_s$, from top to bottom. b) The correlation exponent $K_c^2$ as a function of the band filling $n_e$ for different values of $U$: $U/t = 1, 2, 4, 8, 16$ from top to bottom. (Both figures are taken from [60].)

parameters, $v_c$, $v_s$, and $K_c$, can be extracted [61, 60]. The results are shown in Fig. 2.15.

## 2.5 Experimental realizations of Luttinger liquids

As we saw in the previous section the Hubbard model away from half-filling is a Luttinger liquid (LL). But this model is just a theoretical model. Is there any system in the real world that shows signs of being a Luttinger liquid? The answer is yes!

A natural candidate for a one-dimensional electron system is of course the quantum wire. A quantum wire can be formed by gating a two-dimensional electron gas at the interface between two different semiconductors such as $GaAs$ and $AlGaAs$. The one-dimensional electron gas is formed by depletion of electrons at both sides of a very narrow channel leading to discrete transverse momentum distributions inside the channel, in turn leading to localization of the transverse modes; the transport becomes purely one-dimensional. The problem has been to get samples pure enough so that backscattering against impurities does not destroy the collective modes. As a curiosity I can mention that the group performing the first successful experiment on the chiral Luttinger liquid in 1994 (see Sec. 2.5.1) had looked for similar behavior in a one-dimensional quantum wire but found the task formidable due to the impurities present [62]. Thanks to the fast development of nanostructure technology experiments based on quantum structures are nowadays a reality [63, 64, 65]. The "standard" experiment on a quantum wire is to measure the direct-current (dc) conductance which will be quantized in multiples of a universal value, $G_Q = 2e^2/h$, if the transport is ballistic with noninteracting electrons. In the experiments, a smaller value of $G_Q$ is measured and the predicted value above is recovered only for high temperatures. At a first glance this seems to agree with the Luttinger liquid predictions [66, 67, 68], but these predictions are made for an infinite wire, and recently several groups [69, 70, 71] have shown that for a finite (but clean) wire connected to 3D Fermi liquid leads, the ballistic value should be recovered. The issue is still unresolved and it is even questioned whether the experiments really probe the Luttinger liquid wire and not the (Fermi liquid) leads.

In the following subsections I will focus on two other types of system believed to show Luttinger liquid behavior. I will first discuss a newly discovered and very promising realization, the edge states of a fractional quantum Hall system. This subsection may appear to be outside the scope of this thesis since we have not considered this system at all in our work. However, as an example of a Luttinger liquid, the edge of a quantum Hall system is really worth studying. The main motivation for my own work has instead been the quasi-1D organic metals, and examples of these systems will be discussed in the subsequent subsection.

### 2.5.1 Quantum Hall edges

The Hall effect can be seen in a two-dimensional electron system pierced by a magnetic field. In the classical Hall effect, electrons moving in a magnetic field

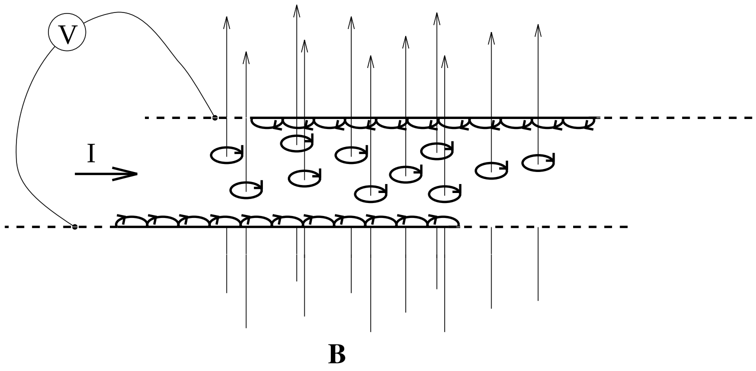


**Figure 2.16**: A pictorial Hall system. Sketched are orbiting electrons (around the magnetic flux lines) and the way in which they form a chiral liquid along the edges. The current is denoted $I$, $V$ is the transverse voltage and $\boldsymbol{B}$ is the magnetic field.

give rise to a potential difference between the two edges parallel to the current as seen in Fig. 2.16. The *quantum* Hall effect manifests itself by plateaus in the measured transverse resistivity ($V/I$) versus magnetic field $B$ (for notation, see Fig. 2.16). The magnetic field can be translated into a *filling fraction*, $\nu$, (measuring the fraction of available quantum states occupied by electrons) and plateaus of resistivity $\frac{1}{\nu}\frac{h}{e^2}$ appear around filling fractions with integer values, $\nu = 1, 2, 3, \ldots$ (the *integer effect*), and with fractional values, $\nu = 1/2, 1/3, \ldots, 2/3, \ldots$ (the *fractional effect*).

As I pointed out already in Chapter 1, the integer and the fractional quantum Hall effects are believed to have different origins. At the level of experiments this is signaled by the fact that the fractional effect is seen only in extremely pure samples, while the integer effect is obtained only in dirty samples (containing impurities). In the fractional case electron-electron interactions dominate the stage, while in the integer case it is the electron-impurity scattering that causes the observed behavior.

The integer quantum Hall effect can be explained within Fermi liquid theory and the edge excitations (see Fig. 2.16) can be seen as a chiral Fermi liquid [72], i.e. a Fermi liquid with only left- *or* right-moving quasiparticles. The fractional quantum Hall effect, in contrast, cannot be described by Fermi liquid theory, as the strong correlations between the electrons—revealed in the Laughlin wave function [73]—drive the system to a non-Fermi liquid phase. Wen has established that the edge state of the fractional quantum Hall system forms a chiral Luttinger liquid (for a review see [74]). The remarkable internal order in a fractional quantum Hall system (which is of topological character) is seen in the parameters of the chiral Luttinger liquid, as these parameters depend on the quantum numbers describing the bulk fractional quantum Hall system. By experimental studies of the chiral Luttinger liquid at the edge of a fractional quantum Hall system, information about the bulk can thus be extracted. In this context it is important to note that there is no backscattering present in a chiral Luttinger liquid since the chiralness forces all of the particles to move in the same direction, impurities merely making the edge of the 2D electron gas meander. This makes experimental studies of a chiral Luttinger liquid easier compared to an ordinary Luttinger liquid since one does not have to worry about impurities. Another remarkable fact, favorable for comparing theory to experiments, is that, in a quantum Hall edge system, the critical exponents appearing in various experimentally measured quantities are universal, only depending on the filling fraction $\nu$. In contrast, measurements on a quantum wire are sample dependent.

In an experiment done by Milliken et al. [75, 62], predictions made by Wen [76] and Moon et al. [77] were tested. In the experiment the tunneling between two edges of a quantum Hall system was measured as a conductance versus point-contact voltage for both a chiral Fermi liquid (integer quantum Hall edge) and a chiral Luttinger liquid (fractional quantum Hall edge). The conductance was found to vary with the temperature as $T^4$ for $\nu = 1/3$ as predicted by the chiral Luttinger liquid theory [77, 78], while for $\nu = 1$ the conductance was temperature-independent as predicted by the chiral Fermi liquid theory. The Milliken group also compared other experimental quantities with predictions from the Luttinger liquid theory and found fairly good agreement.

Chang and collaborators recently carried out another set of experiments, qualitatively confirming (establishing a $T$-dependence) the chiral Luttinger liquid character of the fractional quantum Hall edge [79, 63]. Using a different experimental design, the Chang group circumvented a weakness in the Milliken group experiment: the smoothness of the boundary potential. With a sharp boundary potential, the Chang group was able to extract quantitative results, in particular, the value of several power law exponents. For example, the temperature dependence of the tunneling conductance for $\nu = \frac{1}{3}$ (also considered by Milliken et al.) was extracted to be $T^{1.75\pm0.08}$ and $T^{1.5\pm0.08}$ for two different samples while theory predicts a universal $T^2$ dependence. (The exponent in this experiment should be half of the exponent in the experiment of Milliken et al. since the Chang experiment considers tunneling between a three-dimensional electron gas and a $\nu = \frac{1}{3}$ fractional quantum Hall edge.) At first glance the non-universal exponents are in discrepancy with the theory but the universality is expected only in the limit of vanishing temperature and voltage [63], why further theoretical considerations are needed.

To conclude, there are strong experimental indications that the edge states of a fractional quantum Hall system indeed form a chiral Luttinger liquid. There is a need for further investigations, though, and new predictions need to be tested [80].

### 2.5.2 Quasi-one-dimensional conductors

The Hubbard model in Eq. (2.40) is expected to be a good model for many quasi-one-dimensional conductors, and since the low-energy limit of the Hubbard model is a Luttinger liquid and therefore maps onto the TLM, experimental results on these compounds should show Luttinger liquid behavior.

There are different types of quasi-one-dimensional conductors, *organic* and *inorganic* metals. The inorganic metals are unstable due to phonons creating a Peierls instability as discussed in Sec. 2.2 and this instability makes experiments on these compounds problematic. More promising from an experimental point of view are the organic metals. In these materials the electronic correlations play the dominant role, in contrast to the inorganic metals, where different mechanisms for the behavior cannot be discriminated.

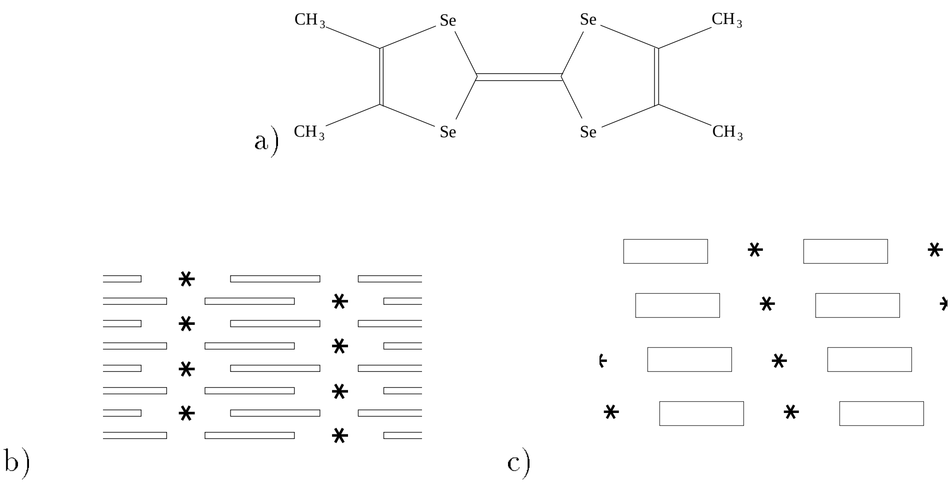


**Figure 2.17**: a) Flat $TMTSF$-molecules are forming b) zig-zag stacks which in turn form c) sheets which together with $PF_6$ sheets form the organic crystal.

The triclinic structure of the organic Bechgaard salts, $(TMTSF)_2X$, is shown in Fig. 2.17 for $X = PF_6$ and the structure is similar for other counter-ions (anions) $X$ [81]. The closed-shell and widely spaced anions do not influence the metallic phase we are interested in, even though they may have consequences for the extreme low-temperature phases. The one-dimensional electron liquid is formed from the molecular $\pi$-orbitals, generic to planar molecules, when these stack in a zig-zag pattern. Sheets of these $TMTSF$-stacks are formed by the $Se-Se$ inter-stack interaction (see Fig. 2.17) and finally sheets of $TMTSF$-molecules and counter-ions are forming the 3D structure [82, 83, 84]. Thus, the conducting axis is the stacking axis. The 1D electron liquid formed by molecular orbitals along the stacking axis suggests that a tight-binding model such as the 1D Hubbard model should be able to describe the behavior of the system, provided the weak coupling between chains may be neglected.

It is interesting to note that there is another series of salts, closely related to the Bechgaard salts, where the Selenium ions in the $TMTSF$-molecule in Fig. 2.17a is replaced by Sulfur ions. These salts are slightly dimerized in their stacking which leads to a half-filled band [85]. The Umklapp term then needs to be incorporated in the Hubbard Hamiltonian to describe this system and this complicates the interpretation of the experimental data. Let us instead restrict our attention to experiments done on the Bechgaard salts.

Two independent experiments on $(TMTSF)_2PF_6$ give evidence of Luttinger liquid behavior: a photoemission experiment performed by Dardel et al. [86] and an NMR experiment done by Wzietek et al. [85]. Let us focus on the photoemission (PES) experiment. In a photoemission experiment, light is directed onto a sample and the kinetic energies of the electrons that are kicked out by the photons are measured (see Fig. 2.18). The Dardel group found an

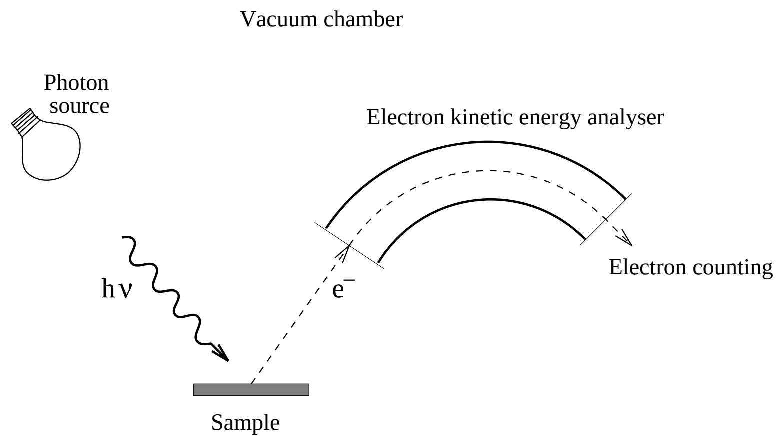


**Figure 2.18**: A photoemission experiment.

unusually low photoemission intensity (number of electrons) near the Fermi energy compared to metals in $D > 1$. This depletion of spectral weight at the Fermi level in the PES experiment can be seen from the spectral function [16] in Fig. 2.9. To obtain the photoemission intensity, $I(\omega)$, as a function of energy $\omega$ from the spectral function in Fig. 2.9, one first has to integrate over $k$ to obtain the total density of states, $N(\omega)$ in Eq. (2.37), and then convolute with the Fermi-Dirac distribution, $f_{FD}(\omega) = 1/(exp(\beta\omega) + 1)$:

$$I(\omega) = f_{FD}(\omega)N(\omega) \ . \tag{2.53}$$

In Fig. 2.9 we see that the spectral density for energies $\omega$ near the Fermi level, $\omega = 0$, is non-zero only for $k$-values near $k_F$. Thus only $k$-values near $k_F$ contribute to the integral giving $N(\omega)$. This is in contrast to the Fermi liquid case in Fig. 2.2 where all $|\boldsymbol{k}|$-values contribute to the spectral weight near the

Fermi energy giving a larger value of $N(\omega)$. We note that for a free electron gas $N(\omega) = 1$, since the $k$-integration in Eq. (2.37) will be over a $\delta$-function for every $\omega$. In the case of free electrons, the PES-intensity is thus a direct probe of the Fermi-Dirac distribution function. An important observation in connection to this is that, since electrons in 3D metals can often be described as a free electron gas, the PES-intensity for small $\omega$ of such a metal should be the Fermi-Dirac distribution function, yielding the Fermi edge cited above.

Several photoemission experiments have also been done on inorganic quasi-one-dimensional metals, such as $(TaSe_4)_2I$ and $BaVS_3$. Both angle-resolved photoemission (ARPES) experiments [87, 88, 89] and angle-integrated photoemission (PES) experiments [90] strongly support the conclusion drawn above that the very low spectral intensity at the Fermi energy and the non-existence of a metallic Fermi edge are indications of correlated electrons. Due to the practical problems connected to the inorganic structure of these materials, other mechanisms behind this unusual behavior cannot be ruled out, however.

As we have seen above, PES results for $(TMTSF)_2PF_6$ indicate that this compound can be seen as a Luttinger liquid, and the Wzietek group experiment [85] on this same compound supports this conclusion. The results suggest a value of the exponent $\alpha$ in Eq. (2.36) of about $\alpha = 1.25$ (for a free electron metal the exponent should be $\alpha = 0$ since $N(\omega) = 1 = \omega^0$, see Eq. (2.38)). Intriguingly, the experimental value of $\alpha$ is far to large to be consistent with theoretical predictions based on the conventional 1D bulk Hubbard model, although this model is expected to be applicable to this class of compounds. The maximum value of $\alpha$ obtained within the framework of the Hubbard model is $\alpha = 1/8$, which is obtained for $K_c^2 = 1/2$ and $K_s^2 = 1$ in Eq. (2.36). $SU(2)$-invariance requires, as we discussed in Sec. 2.4.4, that $K_s = 1$, and in Fig. 2.15 we can see that the minimum value of $K_c^2$ is $K_c^2 = 1/2$, obtained for $U \to \infty$. Many theorists have attempted to solve this mystery, and this is also one of our main motivations for studying the Luttinger liquid with boundaries.

Before going on presenting our work I will summarize some of the differences between Fermi liquids and Luttinger liquids.

## 2.6 Summary: Fermi liquids versus Luttinger liquids

Some of the properties of the TLM are the same as for the Fermi gas, such as the existence of a well-defined Fermi surface and the scaling behavior of thermodynamic quantities such as the specific heat and the magnetic susceptibility. Other properties are distinctly different and I will here focus on three of these properties: the spectral function, the momentum distribution, and the momentum-integrated spectral function (density of states). I have chosen these properties since they are related to my own work: they do not constitute a complete list of differences between Luttinger and Fermi liquids. For example, the transport properties of the two systems also differ dramatically [91].

As we have seen, the non-existence of quasiparticles in one dimension together with the spin-charge separation, implies the existence of a spectral function that differs in a fundamental way from that of a Fermi liquid. This is very well seen in Fig. 2.19. The double-peak structure in the Luttinger liquid

**Figure 2.19**: The spectral functions of a Fermi liquid (top) and a Luttinger liquid (bottom) (from Ref. [89]).

spectral function is due to spin-charge separation, and the vanishing spectral weight around the Fermi energy is a manifestation of the non-existence of quasi-particles. In principle this difference should be seen in angle-resolved photoemission (ARPES) experiments and work along this line is currently going on. For an early reference, see Ref. [89].

Another difference between a Fermi liquid and a Luttinger liquid is their momentum distribution functions (as implied by the different spectral functions, cf. Eq. (2.39)). While the Fermi liquid function shows a distinct quasiparticle jump at the Fermi momentum, the Luttinger liquid function is continuous as is seen in Fig. 2.20.

The difference in the density of states (integrated spectral function) for a

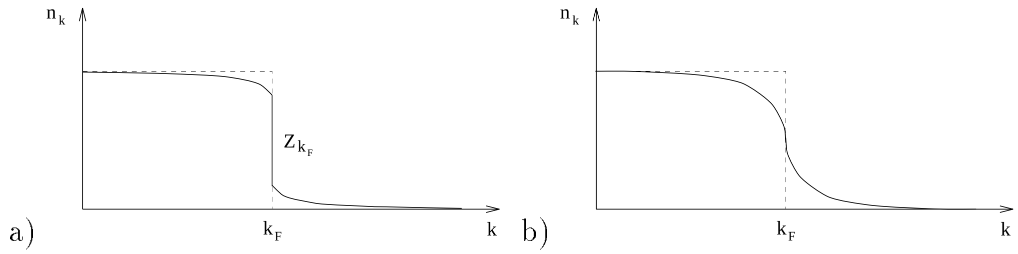


**Figure 2.20**: Momentum distribution function for a) interacting fermions in Fermi liquid theory (more than 1D), and b) interacting fermions in the TLM (1D).

Luttinger liquid and a Fermi liquid will dramatically influence the outcome of a photoemission experiment, which for a Luttinger liquid will show a depletion of spectral weight at the Fermi energy compared with the Fermi liquid. This is shown in Fig. 2.21.

**Figure 2.21**: Typical photoemission intensity as a function of energy for a Fermi liquid and a Luttinger liquid. Spectra of two quasi-one-dimensional compounds, $(TaSe_4)_2I$ and $K_{0.3}MoO_3$, are compared to the spectra for a two-dimensional, $(1T-TaSe_2)$, and a three-dimensional, $Rh$, metal. The depletion of spectral weight at the Fermi level $E_F$ is clearly seen. The picture is taken from Ref. [90].

For a catalogue of experimental signatures of Luttinger liquids vs. Fermi liquids I refer the interested reader to Ref. [41] which contains several papers summarizing the "state-of-the-art".

Next, I turn to my own work on Luttinger liquids.

# 3 Luttinger Liquids with Boundaries: My Work

Low-dimensional electron liquids in the real world, such as the quasi-one-dimensional conductors or the fractional quantum Hall edge states, considered in Sec. 2.5, show a behavior very different from Fermi liquids. As we have seen in Chapter 2, this contrasting behavior can be accounted for by Luttinger liquid theory, at least at a qualitative level. We also saw that when it comes to precise quantitative predictions, theory and experiment do not always agree. This is not at all strange since the theoretical predictions are based on simplified models where only the most important properties are included. For example, the predictions in Sec. 2.3.3 have all been based on the mode-expansion for the infinite (bulk) system (see Fig. 3.1a), that is, the one-dimensionality of the interacting fermion systems has been considered the "leading property" but the fact that the system is finite and confined by boundaries has been neglected. In a real experimental situation there are many features that can contribute to the experimental result even though the overall properties still may be described by the infinite Luttinger liquid. The task for theorists is then to include more effects in their models in order to make better predictions. Along this line a great deal of work has been done at different levels. Focusing on organic metals, people have coupled several infinite Luttinger liquids in order to model the *quasi*-one-dimensionality of these materials. Attempts to include long range Coulomb repulsion have also been made [92]. We have followed another line, based on the fact that photoemission experiments probe only electrons near the surface of a sample: We have introduced *boundaries* into the Tomonaga-Luttinger model, and explored the possible consequences for experiments. This is the topic to be discussed next.

There are several ways of including boundary effects. One approach is to assume that the specific boundary conditions are not important, only the resulting finite-size effects (due to the very presence of a boundary). This situation can be studied in a ring system of length $L$ depicted in Fig. 3.1b,

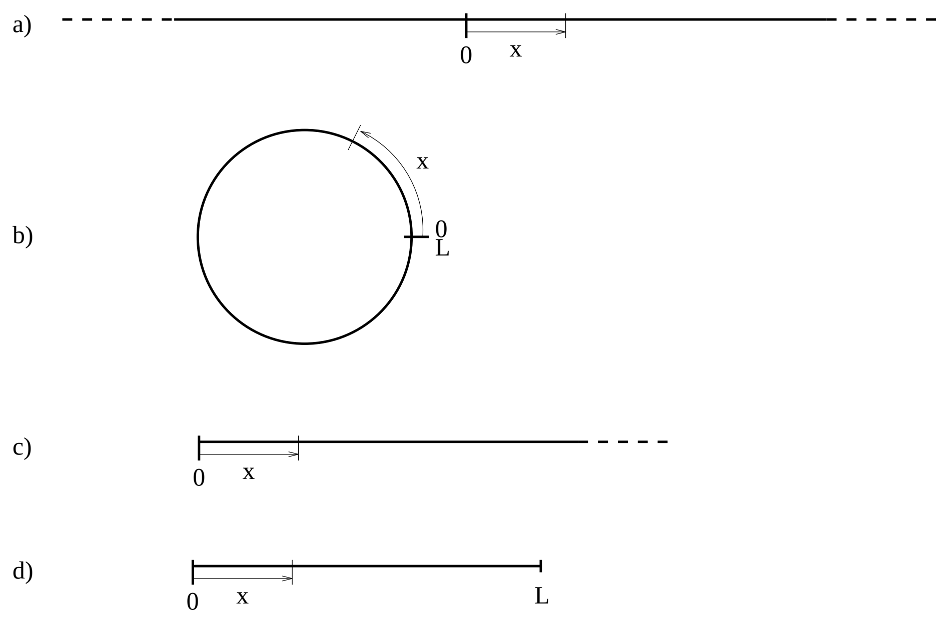


**Figure 3.1**: Different types of systems. a) infinite, b) periodic, c) semi-infinite, and d) finite system.

using periodic boundary conditions. Another approach is to assume that the boundary is the very thing to study while the finite size effects are negligible. The system to study then becomes the semi-infinite system which is shown in Fig. 3.1c. Finally the full effect of both boundaries and finite size can be studied in a finite-size system with boundaries as in Fig. 3.1d.

This chapter will be considerably more technical than the previous chapters. Theoretical research in physics is based on calculations, and information gained at different stages of the calculations build the final conclusion. The analysis of the outcome of a calculation must be done in several steps, and often the analysis must be revised when new calculations have provided new information. In this chapter I mark important features on the map around the path I have been walking but there are many blank areas left and there is certainly a need to go back later and fill these areas with information. A firm path all the way from common knowledge, as presented in Chapter 2, to predictions for the outcome of experiments is, for the moment, only available for the semi-infinite system.

## 3.1 Mode expansions

The bosonization formulas in Sec. 2.3.2 are derived within a formalism where no assumptions about boundary conditions are made. To make calculations we now need to take the next step and impose the proper boundary conditions. To retain a sufficiently powerful formalism, this will be done within a *mode expansion.* The mode expansion can be derived in a variety of ways but since they are mode expansions for *bosons* the method of canonical quantization provides a fast track.

### 3.1.1 Periodic boundary conditions

Let us start with the simplest case of periodic boundary conditions, that of the electron field satisfying

$$\Psi_\sigma(x+L) = \Psi_\sigma(x) \ , \tag{3.1}$$

$L$ being the length of the system. This is the case considered in Paper III. By decomposing the electron field in left- and right-moving components, Eq. (2.44), together with the "magic" formula connecting fermions to bosons, Eq. (2.33), we see that the corresponding boundary conditions for the bosons have the structure

$$\phi_\nu(x) = C_p + \phi_\nu(x+L) \qquad \tilde{\phi}_\nu(x) = \tilde{C}_p + \tilde{\phi}_\nu(x+L) \ , \tag{3.2}$$

where $C_p$ and $\tilde{C}_p$ are constant operators with eigenvalues to be determined. The solution for this bosonic problem has long been known [50] (and is a basic ingredient in string theory where the $C_p = \tilde{C}_p = 0$ case corresponds to a closed string [93]). Solving the classical Euler-Lagrange equation, Eq. (2.31), with the boundary conditions in Eq. (3.2) (treating $C_p$ and $\tilde{C}_p$ as ordinary constants) yields solutions that can be canonically quantized, with the result

$$\begin{aligned}
\phi_\nu(x,t) &= \phi_{\nu,0} + \hat{\Pi}_\nu \frac{v_\nu t}{L} + \hat{Q}_\nu \frac{x}{L} + \\
&\quad + \sum_{n=1}^{\infty} \frac{1}{\sqrt{4n\pi}} \left[ e^{-i\frac{2n\pi}{L}(v_\nu t + x)} a^\nu_{L,n} + e^{-i\frac{2n\pi}{L}(v_\nu t - x)} a^\nu_{R,n} + \text{h.c.} \right] \ , \qquad (3.3) \\
\tilde{\phi}_\nu(x,t) &= \tilde{\phi}_{\nu,0} + \hat{Q}_\nu \frac{v_\nu t}{L} + \hat{\Pi}_\nu \frac{x}{L} + \\
&\quad + \sum_{n=1}^{\infty} \frac{1}{\sqrt{4n\pi}} \left[ e^{-i\frac{2n\pi}{L}(v_\nu t + x)} a^\nu_{L,n} - e^{-i\frac{2n\pi}{L}(v_\nu t - x)} a^\nu_{R,n} + \text{h.c.} \right] \ , \qquad (3.4)
\end{aligned}$$

where the non-zero commutation relations are $[\phi_{\nu,0}, \hat{\Pi}_\nu] = i$, $[\tilde{\phi}_{\nu,0}, \hat{Q}_\nu] = i$ and $[a^\nu_{L/R,n}, {a^\nu_{L/R,n}}^\dagger] = 1$.

The boundary conditions for the chiral fields obtained from the boundary condition for the electron field, Eq. (3.1), provide us with gluing conditions on the eigenvalues $Q_\nu$ and $\Pi_\nu$ of the operators $\hat{Q}_\nu$ and $\hat{\Pi}_\nu$, respectively, (to be derived). Just a minor remark before we go on. In Paper III we explore *spinless* fermions in a periodic system and the connection between this system and the spinful one needs commenting upon. In the formula Eq. (2.22) we should insert a spinless current $J_{L/R}$ and this implies that the prefactor in the magic formula should be replaced according to $\sqrt{\pi/2} \to \sqrt{\pi}$, and that only one of the channels, charge or spin, should be kept. This will not affect the mode expansions; the boson fields are still boson fields even in the spinless fermion case. The gluing conditions, however, will not be the same for the two cases.

Let us now discuss the meaning of the expressions in Eqs. (3.3) and (3.4). Insertion into the Hamiltonian in Eq. (2.27) gives us[1]

$$H_{TLM} = \sum_{\nu=s,c} \left\{ \frac{v_\nu}{2L}(\hat{Q}_\nu^2 + \hat{\Pi}_\nu^2) + \sum_{n=1}^{\infty} \frac{2\pi v_\nu n}{L}(n_{L,n}^\nu + n_{R,n}^\nu + 1) \right\} , \tag{3.5}$$

where $n_{L/R,n}^\nu = a_{L/R,n}^{\nu}{}^\dagger a_{L/R,n}^\nu$. We thus note that $\phi_{\nu,0}$ and $\tilde{\phi}_{\nu,0}$ do not appear in the Hamiltonian, they are only needed in the mode expansion to yield the right commutation relations for the bosons, thereby making the magic formula, Eq. (2.33), valid. Their canonical conjugates, $Q_\nu$ and $\Pi_\nu$, on the other hand, do enter into the Hamiltonian and the inclusion of the zero mode terms (the terms outside the summations in Eq. (3.3) and Eq. (3.4)) is therefore crucial. The original expressions connecting fermions to bosons, derived by Luther and Peschel [29], and Mattis [28], did not have this zero mode but only the sum part. Haldane [30] and, independently, Heidenreich et al. [31] later introduced the zero modes in an appropriate way, making the magic formula into an exact operator identity. We note that the zero modes vanish in the thermodynamic limit, $L \to \infty$, but for a finite length they will certainly influence physical properties, examples of which are given in Paper III.

What then is the physical "meaning" of the zero modes? From Eq. (2.19) and Eq. (2.20) we see that

$$\hat{Q}_\nu = \sqrt{\pi} K_\nu^{-1} \int_0^L \left(J_L^\nu(x) + J_R^\nu(x)\right) dx \ , \tag{3.6}$$

$$\hat{\Pi}_\nu = \sqrt{\pi} K_\nu \int_0^L \left(J_L^\nu(x) - J_R^\nu(x)\right) dx \ . \tag{3.7}$$

From the definition of the chiral currents we conclude that $Q_\nu$ represents the total number of particles relative to the ground state, while $\Pi_\nu$ is a measure of the current in the ring. The gluing conditions relate these two quantities.

Finite-size effects modeled by fermions on a ring have been studied by many other people, usually exploiting the Haldane formalism [30]. Our motivation for using another approach has been that the Haldane formalism is developed within the ring system (periodic boundaries) and therefore not suitable for treating our main problem, fermions in a system with nontrivial boundaries. Let us now turn our attention to the finite fermion system with *open boundary conditions.*

[1] We neglect any constant terms which could be generated in the canonical quantization process [94, 95].

### 3.1.2 Open boundary conditions

In Papers I and II we study the effect of open boundaries on a Luttinger liquid i. e. we impose the condition

$$\Psi_\sigma(0) = \Psi_\sigma(L) = 0 \ , \tag{3.8}$$

on the electron fields, simulating a reflecting barrier or a sharp edge potential. (The notion of an "open" boundary simply means that the system terminates at $x = 0$ and $x = L$, with no coupling of the fields to the external sources.)

Starting from Eq. (3.8), the same procedure as above (in Sec. 3.1.1) yields the mode expansion for open boundary conditions (for details see Paper II)

$$\phi_\nu(x,t) = \phi_{\nu,0} + \hat{Q}_\nu \frac{x}{L} + \sum_{n=1}^{\infty} \frac{1}{\sqrt{n\pi}} \sin\frac{n\pi x}{L} \left[ -ie^{-i\frac{n\pi v_\nu t}{L}} a_n^\nu + \text{h.c.} \right] \ , \tag{3.9}$$

$$\tilde{\phi}_\nu(x,t) = \tilde{\phi}_{\nu,0} + \hat{Q}_\nu \frac{v_\nu t}{L} + \sum_{n=1}^{\infty} \frac{1}{\sqrt{n\pi}} \cos\frac{n\pi x}{L} \left[ e^{-i\frac{n\pi v_\nu t}{L}} a_n^\nu + \text{h.c.} \right] \ . \tag{3.10}$$

The non-zero commutation relations among the mode operators are now $[a_n^\nu, a_n^{\nu\dagger}] = 1$ and $[\tilde{\phi}_{\nu,0}, \hat{Q}_\nu] = i$, while $\phi_{\nu,0}$ are c-numbers. We note that the analog of the operator measuring the current in the ring does not exist in an open finite system, which is natural: since the electrons are *confined*, there is no current. The operator $\hat{Q}_\nu$ is present, however, and measures the number of particles relative to the ground state, as before.

The constants $\phi_{\nu,0}$ will be determined from the boundary conditions, as will the eigenvalues $Q_\nu$ of $\hat{Q}_\nu$. One finds:

$$\phi_{s,0} = 0 \ , \qquad \phi_{c,0} = \sqrt{\frac{\pi}{2}} K_c^{-1}(2l+1) \ , \tag{3.11}$$

where $l$ is an integer. This condition will have as a consequence that

$$\psi_{R,\sigma}(x,t) = -\psi_{L,\sigma}(-x,t) \, , \tag{3.12}$$

as can be seen by examining Eq. (2.33). This is one of the major differences between systems with and without boundaries. Introducing a boundary into the system connects right- and left-moving fields and, as we shall see, this will have some quite surprising consequences for the properties of the system.

The gluing conditions relating $Q_c$ and $Q_s$ take the form

$$K_c Q_c = \sqrt{\frac{\pi}{2}} \left( n + 1 + \frac{2k_F L}{\pi} \right) \ , \tag{3.13}$$

$$K_s Q_s = \sqrt{\frac{\pi}{2}} m \ , \tag{3.14}$$

where $n$ and $m$ are both odd or both even integers.

The Hamiltonian, finally, can be written as

$$H_{TLM} = \sum_{\nu=s,c} \left\{ \frac{v_\nu}{2L} \hat{Q}_\nu^2 + \sum_{n=1}^{\infty} \frac{\pi v_\nu n}{L} (n_n^\nu + \frac{1}{2}) \right\} , \tag{3.15}$$

where $n_n^\nu = a_n^{\nu\,\dagger} a_n^\nu$.

## 3.2 Exact single particle Green's function for a boundary system of finite size at finite temperature

From the mode expansions in Eqs. (3.9) and (3.10) and the magic formula in Eq. (2.33), one can in principle derive *any* correlation function and thus any experimental quantity. We have chosen to consider the finite-temperature single particle Green's function from which the spectral properties of the single electrons can be calculated (cf. our discussion in Sec. 2.3.3). The derivation of this Green's function is exact, no approximations are made. Let me here comment that the *single* effect of finite size *or* finite temperature can conveniently be studied by the method of conformally mapping the $\{z = x + it | x \geq 0\}$ complex semi-infinite plane onto a finite strip [96, 97], a method we use in Paper I to explore the combined effect of a boundary and finite size at $T = 0$. If we want to explore *both* finite size and temperature this route is not possible, however, and the calculations need to be done from "scratch".

From the decomposition of the electron field, Eq. (2.44), and the relation between left- and right-moving fields, Eq. (3.12), we find

$$\begin{aligned} & < \Psi_\sigma^\dagger(x,t)\Psi_\sigma(y,0) > \\ = \; & e^{ik_F(x-y)} G(x,y,t) \; + \; e^{-ik_F(x-y)} G(-x,-y,t) \\ - \; & e^{ik_F(x+y)} G(x,-y,t) \; - \; e^{-ik_F(x+y)} G(-x,y,t), \end{aligned} \tag{3.16}$$

where the chiral Green's function $G(x,y,t) \equiv < \psi_{L,\sigma}^\dagger(x,t)\psi_{L,\sigma}(y,0) > =$ $= < \psi_{L,\sigma}(x,t)\psi_{L,\sigma}^\dagger(y,0) >^*$. The last two terms in Eq. (3.16) originate from the connection between the chiral fields in Eq. (3.12) and they are thus a pure boundary effect. More dramatically, the presence of the boundaries is also seen in the chiral Green's function,

$$\begin{aligned} G(x,y,t) \; \propto H(x,y,t) \prod_{\nu=c,s} \; & (F_\nu(v_\nu t + x - y))^{-\frac{(K_\nu + K_\nu^{-1})^2}{8}} \\ \times \; & (F_\nu(v_\nu t - x + y))^{-\frac{(K_\nu - K_\nu^{-1})^2}{8}} \\ \times \; & \left( \frac{|F_\nu(2x)||F_\nu(2y)|}{F_\nu(v_\nu t + x + y)F_\nu(v_\nu t - x - y)} \right)^{\frac{K_\nu^{-2} - K_\nu^2}{8}} , \end{aligned} \tag{3.17}$$

where the spin and charge factors in the last line are due to the boundaries. That the presence of boundaries introduces new terms and factors into the Green's function has also been noted by Fuentes et al. [98], using a path integral approach. See also Ref. [99].

The function $H(x,y,t)$ comes from the zero modes and reads:

$$H(x,y,t) = \frac{\vartheta_2(u_c+\tau_c\pi\frac{k_F L}{\pi}|\tau_c)\vartheta_3(u_s|\tau_s)+\vartheta_3(u_c+\tau_c\pi\frac{k_F L}{\pi}|\tau_c)\vartheta_2(u_s|\tau_s)}{\vartheta_2(\tau_c\pi\frac{k_F L}{\pi}|\tau_c)\vartheta_3(0|\tau_s)+\vartheta_3(\tau_c\pi\frac{k_F L}{\pi}|\tau_c)\vartheta_2(0|\tau_s)} e^{i2u_c\frac{k_F L}{\pi}} \,, \quad (3.18)$$

where the Theta functions, $\vartheta_k(u|\tau)$, are defined in sections 8.18 and 8.19 in [100] and

$$u_\nu = -\frac{\pi}{2}\left(\frac{v_{Q_\nu}t+x-y}{L}\right) \,, \qquad \tau_\nu = i\beta\frac{v_{Q_\nu}}{L} \,, \qquad v_{Q_\nu} = v_\nu K_\nu^{-2} \,. \quad (3.19)$$

The parameters $K_\nu$ and $v_\nu$ are defined in Eq. (2.28), with $\beta^{-1}$ measuring the temperature. As the zero mode vanishes when $L\to\infty$, the function $H(x,y,t)$ is only present for a finite system. The Theta functions have periodic properties and from this one can deduce that $k_F L$ is defined only modulo $\pi$, as is also obvious from Eq. (3.13).

The function $F_\nu(z)$,

$$F_\nu(z) = i\frac{2L}{\pi}\sin\frac{\pi z}{2L}\prod_{k=1}^{\infty}\left[1+\left(\frac{\sin\frac{\pi z}{2L}}{\sinh k\frac{\pi v_\nu\beta}{2L}}\right)^2\right] \,, \quad (3.20)$$

comes from the oscillator part of the mode expansion with the argument $z$ carrying an implicit cut-off $z-i\alpha$. This function can also be written in terms of Theta functions and in Paper III the Theta form of the function is used, for convenience. The calculations of the functions $H(x,y,t)$ and $F_\nu(z)$ are presented in an appendix in Paper II. Using the same methods, similar expressions can be derived for spinless fermions on a ring and these are presented in Paper III.

We can compare this Green's function with the function derived by Fabrizio and Gogolin [99]. They map an open boundary system of length $L$ onto a periodic system with period $2L$ *under the assumption that* $k_F L = n\pi$. In Sec. 3.4 we will see that this assumption prohibits the prediction of Coulomb-blockade-like oscillations in a finite size system. Our approach is therefore more general and, in addition, is valid for all temperatures.

We have split the analysis of the full, finite-temperature and finite size single particle Green's function for a boundary system, into distinct parts where we consider one effect at the time. As we saw in connection to Fig. 3.1, the single effect of an open boundary can be studied in the semi-infinite system. In Paper I the semi-infinite system at $T=0$ is studied and the same system at finite temperature is considered in Paper II. The single effect of finite length can be studied in the ring system in Fig. 3.1b, and in Paper III we examine this system at finite temperature. I will here follow the same route and first consider the semi-infinite system and then in a following section turn to the finite length system. I will then briefly comment upon the finite size system with open boundaries *and* finite temperature; the complete analysis of this case, including implications for experiments, still remains to be done.

## 3.3 Open boundary effects: the semi-infinite system

We will first study the semi-infinite system at zero temperature in order to concentrate on the sole effect of a boundary in a Luttinger liquid.

### 3.3.1 New power law behavior near the boundary for a semi-infinite system at T=0

In order to analyze the Green's function in Eq. (3.17) we begin by taking the limit of infinite length, $L \to \infty$, and zero temperature, $\beta \to \infty$, thus obtaining the desired semi-infinite system at zero temperature. In this limit the Green's function becomes

$$\begin{aligned} G(x,y,t) \;\propto\; \prod_{\nu=c,s} \quad & (v_\nu t + x - y)^{-\frac{(K_\nu + K_\nu^{-1})^2}{8}} \\ \times \quad & (v_\nu t - x + y)^{-\frac{(K_\nu - K_\nu^{-1})^2}{8}} \\ \times \quad & \left(\frac{4xy}{[(x+y)^2 - v_\nu^2 t^2]}\right)^{\frac{K_\nu^{-2} - K_\nu^2}{8}} \quad . \end{aligned} \tag{3.21}$$

where the time $t$ carries a cut-off, $t - i\alpha$, and measures the time difference between two events at $x$ and $y$. We note that in the limit $xy \gg |(x-y)^2 - v_\nu^2 t^2|$, corresponding to the situation in Fig. 3.2a, or equivalently the "high-energy limit"[2], the last factor in Eq. (3.21) goes to unity and we recover the zero-temperature bulk correlation function in Eq. (2.34) as expected. The boundary-dominated regime ("low-energy limit"[2]) depicted in Fig. 3.2b, $t \gg x = y$, gives us

$$G(x,x,t) \propto |t|^{2\Delta_\parallel} \tag{3.22}$$

[2]By high- (low-) energy limit we mean that we probe events separated by short (long) time intervals on the scale set by the characteristic time to reach the boundary from where the events take place. Cf. Fig. 3.2.

with $\Delta_{||} = (K_c^{-2} + K_s^{-2})/4$, which is a *boundary scaling dimension* characterizing the low-energy limit. As we shall see next this exponent will show up in the spectral properties of a Luttinger liquid with an open boundary.

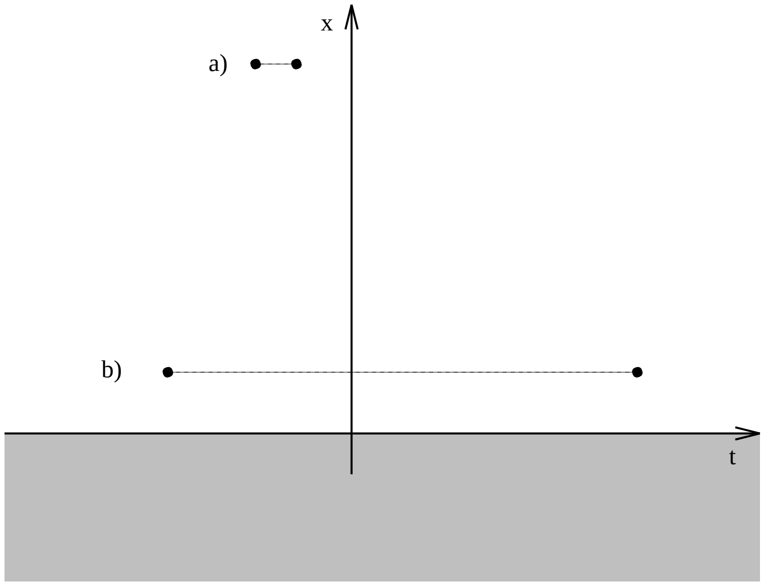


**Figure 3.2**: Two pairs of points in the $x - t$ plane that will show a) bulk and b) boundary correlations.

To summarize: When the distance between two points in the parameter space of position $x$ and time $t$ is much smaller than the distance to the boundary, i.e. the situation given in Fig. 3.2a, the influence of the boundary will be small and we will obtain the same correlations as in the bulk case. If two points are far from each other with respect to the boundary, as is the situation in Fig. 3.2b, the boundary will certainly influence their correlation. Since the long time behavior governs the low-energy properties, it is not farfetched to believe that the low-energy properties of a Luttinger liquid with a boundary will be different from the ordinary bulk Luttinger liquid properties. Indeed they are, as we have seen above.

To compare with experiments, we need to translate our results into some observable. Intrigued by the "$\alpha$-exponent puzzle" discussed in Sec. 2.5.2 we have chosen to analyze our work in the context of photoemission spectroscopy (PES) on the Bechgaard salts and have translated our Green's function into a *local spectral density*, $N(\omega, r)$ with $r$ measuring the distance to the boundary. As PES only probes electrons close to a boundary, $N(\omega, r)$ contains more relevant information than the bulk spectral density $N(\omega)$ considered in Sec. 2.3.3 (Eq. (2.38)). The local spectral density can be derived from the spectral function according to Eq. (2.37) but we will instead use the formula connecting the local spectral density directly to the full electron Green's function:

$$N(\omega,r)=\frac{1}{2\pi}\int_{-\infty}^{\infty}e^{i\omega t}\langle\Big\{\Psi_\sigma^\dagger(r,0),\Psi_\sigma(r,t)\Big\}\rangle dt, \qquad (3.23)$$

where $\omega$ is measured relative to the Fermi energy. The electron Green's function in Eq. (3.23) is connected to the chiral Green's function through Eq. (3.16), and from Eq. (3.22) we obtain the low-energy behavior

$$N(\omega,r)\propto|r\omega|^{\alpha_{bound}} \qquad (3.24)$$

where $\alpha_{bound}=2\Delta_{||}-1$ is the *boundary exponent*:

$$\alpha_{bound}=\frac{K_c^{-2}+K_s^{-2}}{2}-1\ . \qquad (3.25)$$

A thorough analysis of the local spectral density (see Paper II) reveals that the boundary behavior will be seen for $\omega \ll v_c/r$ and this implies that irrespective of the distance to the boundary there will *always* be a low-energy region where the scaling of the local spectral density is dominated by the boundary exponent $\alpha_{bound}$.

In Fig. 3.3 we see the local spectral density as a function of $r\omega$ for the large $U$ Hubbard model away from half filling. We clearly see the crossover from boundary behavior at low energies, dominated by the power law with exponent $\alpha_{bound}=1/2$, to bulk behavior at high energies, following the bulk power law with exponent $\alpha=1/8$ [35].

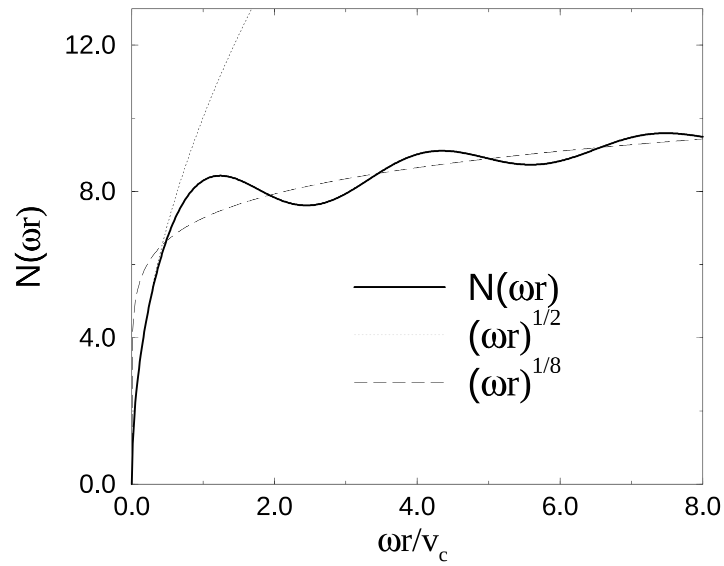


**Figure 3.3**: The local spectral density vs. $r\omega$ at $T=0$. The asymptotic power laws for bulk and boundary regions are superimposed.

Let us consider the implications of this new power law behavior on the outcome of a photoemission experiment. The photoemission intensity is obtainable from Eq. (2.53) but we now have to consider the distance to the boundary. In a photoemission experiment (see Fig. 2.18), photons impinge on a sample producing emission of electrons. The electrons can be emitted only if they are sufficiently close to the boundary and we have to integrate over this escape region:

$$I(\omega) \propto \int dr f_{FD}(\omega) N(\omega, r) \ . \tag{3.26}$$

This adaptation to reality is not enough, though; we also have to consider the experimental resolution. This is necessary since the spectral density of the Luttinger liquid (in contrast to that of a Fermi liquid) vanishes as a power law for small $\omega$ according to Eq. (2.38) (Eq. (3.24)) in the bulk (boundary) case. The experimental resolution effectively introduces an averaging over an energy interval of order $\Delta$ and we take this into account by a Gaussian average,

$$I_{obs}(\omega) \equiv \frac{1}{\sqrt{2\pi}\Delta} \int e^{-(\omega-x)^2/2\Delta^2} I(x) dx \ . \tag{3.27}$$

(In the 3D (Fermi liquid) case the spectral density is energy independent ($\alpha = 0$) and this averaging procedure is therefore not needed.)

Inserting experimentally relevant values of various parameters (for details, see Paper I) allows us to make a prediction for the observed photoemission intensity and in Fig. 3.4 we show the result for different exponents $\alpha$. We

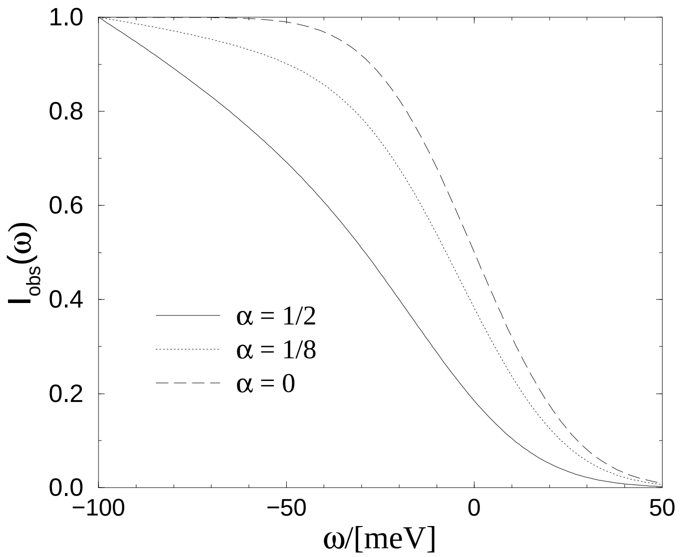


**Figure 3.4**: The predicted photoemission intensity $I_{obs}$ in arbitrary units as a function of energy $\omega$.

clearly see a depletion of spectral weight at the Fermi level for the the boundary case with exponent $\alpha = 1/2$. Unfortunately the energy range over which the depletion occurs is far too small compared to the experimental curve even though our predictions are much better than the conventional predictions based on the bulk Luttinger liquid maximum value of the exponent, i.e. $\alpha = 1/8$ [35].

Our conclusion is that, even though a boundary Luttinger liquid system clearly shows a larger depletion of spectral weight at the Fermi level than a bulk Luttinger liquid, the effect of a boundary cannot fully explain the discrepancy between theory and experiment.

In the above considerations, the temperature dependence has only been taken care of in the Fermi-Dirac distribution in Eq. (3.26) and the possible temperature shift in $N(\omega, r)$ has been neglected. In the next section we will study the influence of temperature on the semi-infinite system and thus be able to conclude if this approximation is acceptable.

### 3.3.2 $\omega^2$ behavior for small $\omega$ in a semi-infinite system at $T > 0$

Let us explore a system that is large compared to the inverse temperature scale, $L \to \infty$ with $\frac{\pi v_\nu \beta}{2L} \to 0$. Carefully taking this limit in Eq. (3.17) yields

$$
\begin{aligned}
G(x,y,t) \propto \prod_{\nu=c,s} & \left( \frac{v_\nu \beta}{\pi} \sinh \frac{\pi(v_\nu t + x - y)}{v_\nu \beta} \right)^{-\frac{(K_\nu + K_\nu^{-1})^2}{8}} \\
\times & \left( \frac{v_\nu \beta}{\pi} \sinh \frac{\pi(v_\nu t - x + y)}{v_\nu \beta} \right)^{-\frac{(K_\nu - K_\nu^{-1})^2}{8}} \\
\times & \left( \frac{\sinh \frac{\pi 2x}{v_\nu \beta} \sinh \frac{\pi 2y}{v_\nu \beta}}{\sinh \frac{\pi(x+y+v_\nu t)}{v_\nu \beta} \sinh \frac{\pi(x+y-v_\nu t)}{v_\nu \beta}} \right)^{\frac{K_\nu^{-2} - K_\nu^2}{8}} .
\end{aligned}
\tag{3.28}
$$

The corresponding local spectral density is again obtained via Eq. (3.23) and an analysis reveals that the temperature only affects the low-energy part, $\omega < \frac{2\pi}{\beta}$, of the spectral density, while the high energy part is unaffected. This is clearly seen in Fig. 3.5 where again we have considered the large $U$ Hubbard model away from half-filling. For low energies the local spectral density is proportional to the square of the energy, $N(\omega) \propto \omega^2$, and this behavior is also present in the bulk case. The bulk Luttinger liquid at finite temperature was considered by Meden and Schönhammer [47] and the $\omega^2$-behavior is seen in Fig. 4 of Ref. [47].

The implications for the photoemission experiment predictions in Fig. 3.4 will evidently be a further depletion of spectral weight at the Fermi level. However, the effect will not be sufficiently large to account for the discrepancy between experiment and theory.

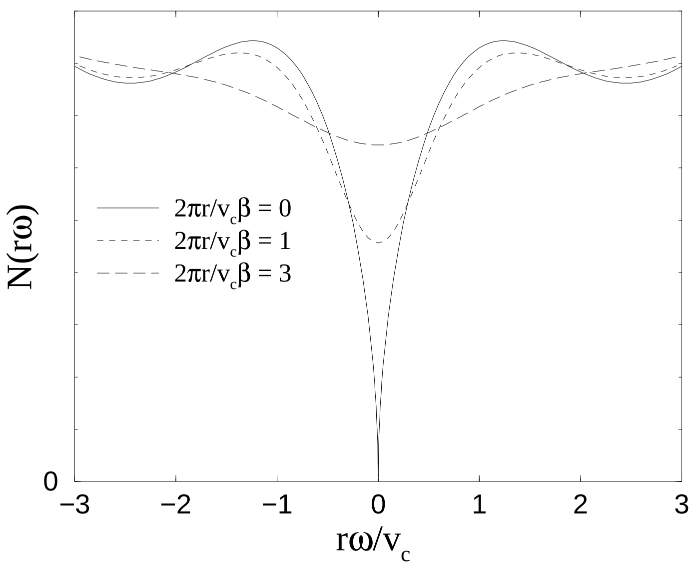


**Figure 3.5**: Local spectral density vs. $\omega$ at different temperatures. For small $\omega$ we obtain $\omega^2$ behavior.

## 3.4 Finite size effects: the periodic system

As a spin off from the calculations of the chiral Green's function in Eq. (3.17), we recognized that the same method could be used to study the properties of spinless fermions on a ring *at finite temperature*. The finite length system at zero temperature can be obtained by a conformal mapping of the infinite system but, as I have already pointed out, the simultaneous effect of finite length and finite temperature can not be reached with this method. Our interest was primarily to numerically confirm our exact analytical expression for the finite-length, finite-temperature density-density correlation function and, indeed, the agreement between our analytical expression and the expression obtained by numerical simulations on the test system, spinless fermions on a ring, is excellent (see Paper III). We also discovered that the part of the Green's function originating from the zero mode (corresponding to $H(x,y,t)$ in Eq. (3.18)) gives rise to Coulomb-blockade-like oscillations. These oscillations stem from the fact that a finite length system has regular energy-level spacings. The Coulomb-blockade-like oscillations are observed in experiments where the Fermi energy can be changed, for example, by applying a gate-voltage. As our formalism is valid for any value of the Fermi wave vector $k_F$, and thereby for any value of the Fermi energy, the Coulomb-blockade-like oscillations are indeed obtained within our theory.

At this point, let us focus on the finite-size effects on the spectral properties. For simplicity, I will use the results obtained for the Green's function for spinless fermions on a ring in Paper III to illustrate the finite size effects on the spectral density.

The calculations proceed as before. The mode expansion to use for the spinless fermion system on a ring can be adapted from the corresponding spinful case, as explained in Sec. 3.1.1. In this way the chiral Green's function, $G(x,t) = \langle \psi_L(x,t)^\dagger \psi_L(0,0)\rangle$ at $T=0$ is calculated,

$$G(x,t) \propto e^{i(n_0 \bmod 2)x_Q} \left[\frac{L}{\pi}\sin\left(\frac{\pi}{L}(vt+x)\right)\right]^{\frac{-(K+K^{-1})^2}{4}} \left[\frac{L}{\pi}\sin\left(\frac{\pi}{L}(vt-x)\right)\right]^{\frac{-(K-K^{-1})^2}{4}}, \tag{3.29}$$

where $n_0 = \frac{k_F L}{\pi} + 1$, $x_Q = \frac{\pi}{L}(x + vt/K^2)$ and $t$ carries a cut-off, $t - i\alpha$, as before. We note that there are no terms in this expression corresponding to the terms on the last line of the boundary analog in Eq. (3.17): there is no boundary in a ring system!

The analysis of the Green's function in Eq. (3.29) is intricate since its periodicity introduces new aspects to consider as compared to the analysis of the semi-infinite system in Sec. 3.3. By the use of a Taylor expansion,

$$\left(i\sin\frac{\pi v}{L}t\right)^{-\gamma} = \left(\frac{e^{i\frac{\pi v}{L}t}}{2}\right)^{-\gamma} \sum_{n=0}^{\infty} c_n(\gamma) e^{-i\frac{2n\pi v}{L}t} \tag{3.30}$$

with

$$c_n(\gamma) = \frac{\Gamma(n+\gamma)}{\Gamma(\gamma)\Gamma(n+1)} \tag{3.31}$$

the spectral density can still be derived. (Note that the expansion in Eq. (3.30) is valid since we have the small cutoff $i\alpha$ present in the time variable $t$.) Using the definition of the spectral density in Eq. (3.23) (with $x = r - r = 0$, due to translational invariance) we obtain

$$\begin{aligned} N(\omega) \propto & \sum_{n=0}^{\infty} c_n\left(\tfrac{K^2+K^{-2}}{2}\right) \times \\ & \left\{\delta\left(\omega + (n_0 \bmod 2)\frac{\pi v}{L}K^{-2} - \frac{\pi v}{2L}(K^2+K^{-2}) - 2n\frac{\pi v}{L}\right) + \right. \\ & \left. + \quad (\omega \to -\omega) \qquad \right\}, \end{aligned} \tag{3.32}$$

where $\omega$ is measured with respect to the Fermi energy $E_F$, that is, $\omega = E - E_F$. Note that the spectral density is discrete in $\omega$, consistent with the finite length of the system. We also note that for noninteracting fermions, that is $K=1$, the argument of the $\delta$-function is $(\omega - vk_F^0 - 2n\frac{\pi v}{L})$ where $k_F$ is shifted so as to be in the interval $0 < k_F^0 \le 2\pi/L$, $k_F + k_F^0 = N\frac{\pi v}{L}$, $N$ being an integer (see Fig. 3.6). We conclude that the phase originating from the zero mode shifts the energy scale in the spectral density so as to correspond to the Fermi wave vector, see Fig. 3.6. If the Fermi level $E_F = vk_F$ is chosen (by the aid of a gate-voltage for example) so as to not correspond to an energy level of the system, the first peak in the spectral density will not appear at $\omega = 0$ but at

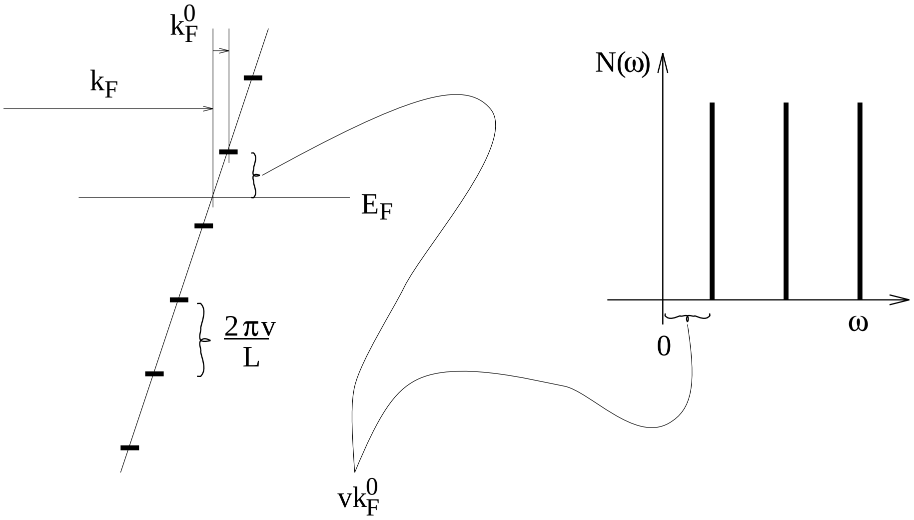


**Figure 3.6**: The position of the first peak of the spectral density at positive energies is dependent on our choice of $k_F$ in the expansion of the electron field in chiral fields Eq. (2.44). Here $K = 1$ (free fermions).

$\omega = vk_F^0$. The position of the first peak is clearly affected by the interactions via the parameter $K$, which could then be measured experimentally.

We have analyzed two systems, the semi-infinite system with new power law behavior for low energies, and the finite length system showing a discrete spectral density. In the treatment of the semi-infinite system with an open boundary we have focused on the boundary effects while in the treatment of the periodic system we focused on the finite-size effects. We are now prepared to combine the two analyses and consider the finite-length system *with* open boundaries.

## 3.5 Combined effects from boundaries and finite size

An analysis of the full formula in Eq. (3.17) reveals that it has a complicated time dependence originating from the spin-charge separation. In Sec. 3.4 we studied the spectral density for spinless fermions on a ring, where only one velocity governed the time dependence of the Green's function, leading to a single periodicity of the spectral density. In this subsection we will study the case where *two* velocities influence the periodicity of the local spectral density.

Let us restrict ourselves to the zero temperature case. Taking the zero temperature limit ($\beta \to \infty$ in Eq. (3.20)) of the formula Eq. (3.17), we obtain

(up to an overall phase)

$$
\begin{aligned}
G(x,y,t) \;\propto\; \prod_{\nu=c,s} \quad & \left(\frac{2L}{\pi}\sin\frac{\pi(v_\nu t + x - y)}{2L}\right)^{-\frac{(K_\nu+K_\nu^{-1})^2}{8}} \\
\times \quad & \left(\frac{2L}{\pi}\sin\frac{\pi(v_\nu t - x + y)}{2L}\right)^{-\frac{(K_\nu-K_\nu^{-1})^2}{8}} \\
\times \quad & \left(\frac{\sin\frac{\pi x}{L}\sin\frac{\pi y}{L}}{\sin\frac{\pi(x+y+v_\nu t)}{2L}\sin\frac{\pi(x+y-v_\nu t)}{2L}}\right)^{\frac{K_\nu^{-2}-K_\nu^2}{8}} .
\end{aligned}
\tag{3.33}
$$

Using the same method as in Sec. 3.4, expanding each factor in a Taylor series by the use of Eq. (3.30), gives us a local spectral density as a double sum over a $\delta$-function:

$$
\begin{aligned}
N(\omega,r) \;\propto\; & \sum_{n=0}^{\infty}\sum_{m=0}^{\infty} f_n(a_c,b_c,r) f_m(a_s,b_s,r) \times \\
& \times \Bigg(\delta(\omega - \frac{\pi v_c k_c}{2L} - \frac{\pi v_s k_s}{2L} - n\frac{\pi v_c}{L} - m\frac{\pi v_s}{L}) \\
& \quad + \delta(\omega + \frac{\pi v_c k_c}{2L} + \frac{\pi v_s k_s}{2L} + n\frac{\pi v_c}{L} + m\frac{\pi v_s}{L})\Bigg) ,
\end{aligned}
\tag{3.34}
$$

where $a_\nu = (K_\nu^2 + K_\nu^{-2})/4$, $b_\nu = (K_\nu^{-2} - K_\nu^2)/8$, $k_\nu = a_\nu + 2b_\nu$ and

$$
f_s(k_1,k_2,r) = \sum_{p=0}^{s} c_{s-p}(-k_1)\sum_{q=0}^{p} c_q(-k_2)c_{p-q}(-k_2)\cos\left((p-2q)\frac{\pi 2r}{L}\right) . \tag{3.35}
$$

We see that the spinful system still shows a discrete spectrum but the positions of the peaks[3] are now determined by two integers, $n$ and $m$, instead of a single integer as in the spinless fermion case in Eq. (3.32). This is due to the spin-charge separation of the spinful model with *two* velocities, $v_c$ and $v_s$, governing the positions of the peaks.

It is instructive to plot the argument of the $\delta$-function in a two-dimensional plot with $n$ and $m$ indexing the different points as shown in Fig. 3.7. The line connecting $(\omega,0)$ and $(0,\omega)$ indicates where the argument of the delta-function vanishes, and hence selects the terms to be included in the double sum in Eq. (3.34). When $v_s/v_c$ is a rational number the spectrum separates into distinct peaks of equal spacing. The distance between the peaks gets compressed for large values of $\omega$ when $v_s/v_c$ is irrational, leading to a quasi-continuum. Although the effect clearly is not possible to observe directly, it

[3] Here, we do not consider the offset, since we have not included the phase originating from the zero-mode in Eq. (3.33).

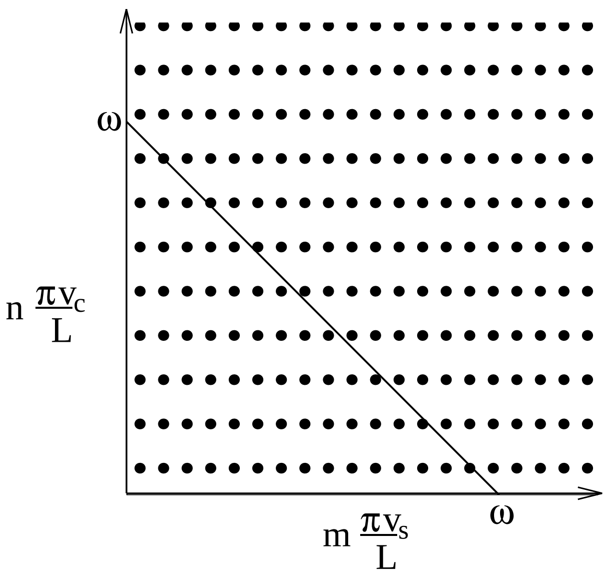


**Figure 3.7**: Illustration of how to calculate the local spectral density from the expression in Eq. (3.34). The coordinates $n$ and $m$ are the summation indices.

may nonetheless suggest some kind of resonant interference between "standing waves" of charge and spin for certain privileged values of $v_s$ and $v_c$.

A complete understanding of the *combined* effects of nontrivial boundaries and finite size, in particular their role in PES experiments, requires much more work, theoretical as well as experimental. As we have seen, at a theoretical level the problem is intricate already for zero temperature, and becomes even more so when including finite-temperature effects.

There is more to be done.

# Part II

# Antiferromagnets

# 4 Antiferromagnets: Introduction

Antiferromagnetism is a young subject, compared to its more well-known relative, ferromagnetism. Before neutron scattering experiments became available in 1949 antiferromagnetism was an unknown phenomenon in Nature, although the French physicist Louis Néel had hypothesized its existence some 15 years earlier. Nowadays antiferromagnetism is extensively studied and, as we saw in Chapter 1, it is even considered a possible ingredient in the mechanism behind superconductivity in the high-$T_c$ superconductors. In this chapter I will begin with a short overview of magnetic phenomena, including antiferromagnetism, and I will then attempt to explain the origin of magnetic interactions and specifically motivate why the Heisenberg model is the model of choice for describing antiferromagnetic correlations in insulating compounds.

In Sec. 4.3, I will introduce the two-dimensional (2D) Heisenberg model, the model most studied in connection to the high temperature superconductors, focusing on properties influencing the character of the ground state, such as the magnitude of the spin and frustration. Different lattice types also influence the degree of order or disorder in a magnetic system and in connection to a discussion of this I introduce the two systems studied in Papers IV and V: the 2D Heisenberg model on a triangular and honeycomb lattice, respectively.

In contrast to the one-dimensional model, the Heisenberg model in two dimensions is not exactly solvable. Instead, approximate theories have to be used. I will review two such theories, the Spin-Wave Theory in Sec. 4.4 and the Schwinger-Boson Mean-Field Theory in Sec. 4.5, which can be used to extract information from the model.

I will end this chapter with a discussion on the connection to experiment, as coded in the dynamic structure factor.

## 4.1 Magnetism: a short introduction

Magnetic phenomena are purely quantum mechanical in origin. Before quantum mechanics entered the stage in the beginning of the 20th century no microscopic explanation of magnetism was available. There is even a theorem, the Bohr-van Leeuwen theorem (see Ref. [21] for an outline of the proof), according to which one cannot obtain any magnetization at all using classical statistical mechanics. This theorem was originally stated by Niels Bohr in his doctoral thesis in 1911 and was then rediscovered by J. H. Leeuwen in her thesis in 1919, and it marks the end of the classical era of magnetism. With quantum mechanics a new era opened, with much successful work in explaining the origin of magnetic interactions. As usual, however, many new questions were posed, and the study of quantum magnets is still a very active area of research. For an excellent review of the history of magnetism I refer the interested reader to Ref. [101].

Let us now consider the different sorts of magnetism familiar from the textbooks, in order to introduce antiferromagnetism on the stage.

### 4.1.1 Dia- and paramagnetism

*Diamagnetism* is a property of all matter. When exposed to a magnetic field $\boldsymbol{H}$, matter responds with a magnetization $\boldsymbol{M}$ according to $\boldsymbol{M} \propto -\boldsymbol{H}$. The origin of diamagnetism is the effect of an applied field on the motion of electrons. A single electron moving in its atomic orbital can be viewed as a resistance-less current loop giving rise to an associated magnetic moment: an applied field *reduces* the magnetization due to back e.m.f.. *Paramagnetism* occurs when matter responds to an applied field according to $\boldsymbol{M} \propto \boldsymbol{H}$. This behavior is caused by the spin and the orbital angular momentum together in the total angular momentum. The origin of paramagnetic behavior is thus the coupling of an applied field to permanent dipoles.

Let us first consider *insulating solids*, i.e. solids composed of non-interacting ions. If the ions in the solid have all their electronic shells filled, we have no net spin, no net orbital momentum and thereby no total angular momentum. As a consequence, the solid will not have any paramagnetic behavior, it will only exhibit *Larmor diamagnetism* (also called "Langevin" or "core diamagnetism"). This behavior is seen in solid noble gases and alkali halides.

If the solid is composed of ions with shells one electron short of being half filled, we still have no total angular momentum, but the non-vanishing spin and orbital momentum independently gives rise to a weak paramagnetic behavior, *Van Vleck paramagnetism.* The net magnetic behavior of these ions will be determined by a balance between the Larmor diamagnetism and the Van Vleck paramagnetism.

*Ideal paramagnetism* is supported very well by insulating crystals containing rare earth ions. Rare earth ions have partially filled *f*-shells and thereby non vanishing total angular momentum. The *f*-shell lies deep in the electron cloud surrounding the nuclei, and in crystals these shells are only weakly affected by the crystalline environment. ("Ideal paramagnetic" means an ideal (non interacting) gas of magnetic moments.)

Turning to *metallic solids* it is easy to see, using the free electron gas model, that the conduction electrons exhibit both diamagnetic and paramagnetic responses. *Landau diamagnetism* is due to the orbital electronic motion induced by the field. *Pauli paramagnetism*, on the other hand, is due to the Zeeman splitting of the free electron energy band into two parts, one for spin up and one for spin down. The electrons flip their spins in order to minimize the free energy and this leads to a net magnetization.

Fig. 4.1 shows how different sorts of magnetism are related in the "family tree" of magnetism.

**Figure 4.1**: The family tree of magnetism (from Ref. [102])

As a last point it must be mentioned that, of course, most of the substances present in nature do not show only one sort of magnetism. In estimating the net effect of an applied field on the magnetization, one therefore needs to take several of the above effects into account.

### 4.1.2 Spontaneous magnetic order

In the above discussion we neglected any magnetic interaction between the individual magnetic moments. This implies that in zero applied field the net magnetization averages out to zero because of thermal disorder. However, there are solids that do possess magnetization even if we do not apply any external magnetic field. This is known as *spontaneous magnetization*. The two different kinds of such magnetism are *ferromagnetism* and *ferrimagnetism*. There is also a third class of magnets, the *antiferromagnets*, which do not possess any net magnetization. In Fig. 4.2, 1D arrays illustrate the different types of magnetic order.

**Figure 4.2**: Linear arrays of spins illustrating possible (a) ferromagnetic, (b) antiferromagnetic, and (c) ferrimagnetic orderings (from Ref. [21]).

All spontaneous magnetic order is due to the electrostatic interaction between the constituents of the matter which are carrying permanent moments (e.g. electrons), together with the statistics of these constituents (for electrons, Fermi statistics, or equivalently, the Pauli principle). The direct magnetic dipole-dipole interaction is far too weak to be the source of spontaneous magnetization. The intricate mechanism causing ferro- and antiferromagnetic interactions will be reviewed in the next section.

## 4.2 From electron systems to spin models: the physical origin of magnetic interactions

In this section I will motivate the use of the Heisenberg Hamiltonian when studying antiferromagnets. The theory of the origin of magnetic interactions is one of the less well developed fundamental areas of condensed matter physics. In fact, the formulation of a theory of magnetic *metals*, describing both the electronic spin correlations *and* the transport properties, remains an unsolved problem of modern condensed matter theory.

In the following, however, we shall concentrate on magnetic insulators, that is, solids with narrow bands, where the absence of charge transport is due to electron correlations. These materials are known as Mott insulators [104], and experiments show that they are quite common in nature[1].

The task to explain magnetism in insulators is not an easy one. We can not use band theory, with its impressive successes to account for non-magnetic properties, since being magnetic solids, they clearly do not have filled bands. On the other hand they are insulators and therefore non-conducting. In fact, the band theory can not account for any magnetic properties, not even in metals, since band theory is based on the independent electron model, while magnetism is a collective phenomenon driven by electron correlations.

Instead the usual approach to magnetic interaction is to bring magnetic atoms together, assuming that their electronic wave functions are more or less unchanged. This is a good starting point when dealing with Mott insulators.

Here it must again be emphasized that the most important source of magnetic interaction is the ordinary *electrostatic* electron-electron interaction, not the dipole-dipole or spin-orbit coupling. One says that magnetic interaction is due to *Coulomb interaction together with the Pauli exclusion principle.*

The effective Hamiltonian that models this interplay between quantum statistics and electrostatics is the famous Heisenberg Hamiltonian [105, 106]. It is written in terms of the spin exchange operator,

$$\mathcal{H} \propto \boldsymbol{S}_i \cdot \boldsymbol{S}_j\,, \tag{4.1}$$

with the magnetic interaction described by using spin operators $\boldsymbol{S}$ *localized* on the different lattice points $i$ and $j$. In the following I shall try to explain the mechanism behind this spin exchange interaction.

### 4.2.1 Electron wave functions: the role of the Pauli principle

The Pauli exclusion principle requires that the total wave function of an electron (fermion) must be antisymmetric under simultaneous interchange of both space and spin coordinates. This has dramatic consequences for the behavior of a many-electron system.

As a tutorial example, let us consider the simplest many-electron system, that of two electrons. The total wave function can be written as a product of

[1] The undoped high-$T_c$ compounds are believed to be examples of Mott insulators

a spin and a space (orbital) wave function,

$$\psi = |\text{space}\rangle \times |\text{spin}\rangle. \tag{4.2}$$

The spin state is made up from the individual spin states of each electron. We define spin operators for each electron, $\boldsymbol{S}_1 = (S_1^x, S_1^y, S_1^z)$ and $\boldsymbol{S}_2 = (S_2^x, S_2^y, S_2^z)$, obeying the usual spin commutation relations

$$\left[S_i^x, S_j^y\right] = iS_i^z\delta_{ij}\,, \tag{4.3}$$

and cyclic permutations of $xyz$. Here and in the following we put $\hbar = 1$. The four possible spin states formed out of the eigenstates of the spin operators $S_1^z$ and $S_2^z$ are

$$|\uparrow\uparrow\rangle\,,\ |\uparrow\downarrow\rangle\,,\ |\downarrow\uparrow\rangle\,,\ |\downarrow\downarrow\rangle\,. \tag{4.4}$$

where $|\uparrow\uparrow\rangle$ is short for $|\uparrow\rangle_1 \otimes |\uparrow\rangle_2$, 1 and 2 referring to the two different electrons. The proper linear combinations that are eigenstates of the operators $\boldsymbol{S}^2$ and $S^z$, with $\boldsymbol{S} = \boldsymbol{S}_1 + \boldsymbol{S}_2$ the total spin, are given by

$$|S\rangle = \quad \tfrac{1}{\sqrt{2}}(|\downarrow\uparrow\rangle - |\uparrow\downarrow\rangle) \qquad S = 0 \text{ (singlet)} \tag{4.5}$$

$$|T\rangle = \left\{ \begin{array}{c} |\uparrow\uparrow\rangle \\ \tfrac{1}{\sqrt{2}}(|\downarrow\uparrow\rangle + |\uparrow\downarrow\rangle) \\ |\downarrow\downarrow\rangle \end{array} \right. \qquad S = 1 \text{ (triplet)}\,. \tag{4.6}$$

We shall see later (Sec. 4.2.5) that the singlet state corresponds to an antiferromagnetic state and that the three triplet states correspond to ferromagnetic ones. If we perform a permutation of the spin coordinates in (4.5) and (4.6), we see that these states are eigenstates of the permutation operator; the singlet state has eigenvalue $-1$ and the three triplet states have eigenvalues 1. The Pauli principle then implies that a permutation of the coordinates in the space part of the total wave function must yield a plus sign for the singlet state but minus signs for the three triplet states. The singlet state then corresponds to a symmetric space wave function and the triplet states to an antisymmetric one.

We thus see that the Pauli exclusion principle connects the spin and space parts of the total wave function. Even a Hamiltonian that has no explicit spin dependence, thus acting only on the space part of a state, is in fact spin dependent through the Pauli principle. One example, studied in most textbooks (see e.g. Ref. [107]), is the helium atom. Here a seemingly spin independent Hamiltonian, with the potential made up of the three Coulomb terms originating from interactions between the two electrons and the nucleus, gives a singlet ground state, "parahelium", and a triplet first excited state, "orthohelium".

At this point, let us look a little closer at the space part of the total wave function in (4.2), using the language of *quantum chemistry* [109]. The spin states in (4.5) and (4.6) only require the space functions to be either symmetric or antisymmetric. (We will deal only with spin independent Hamiltonians, which implies that the three triplet states will all have the same space function giving them the same energy: the triplet states are degenerate.) Assuming the two electrons to be localized (remember that we are interested in insulators), we start with two atomic orbitals $\phi_l(\boldsymbol{r})$ and $\phi_r(\boldsymbol{r})$, satisfying the Schrödinger equations

$$\left(\frac{p_1^2}{2m} - \frac{e^2}{r_{1l}}\right)\phi_l(\boldsymbol{r}_1) = \epsilon\phi_l(\boldsymbol{r}_1) \tag{4.7}$$

and

$$\left(\frac{p_2^2}{2m} - \frac{e^2}{r_{2r}}\right)\phi_r(\boldsymbol{r}_2) = \epsilon\phi_r(\boldsymbol{r}_2)\,, \tag{4.8}$$

Here $r_{ik} = |\boldsymbol{r}_i - \boldsymbol{R}_l|$ $(i = 1, 2)$, with $\boldsymbol{R}_l$ ($\boldsymbol{R}_r$) being the location of the "left" ("right") nucleus, and with $\boldsymbol{r}_1$ and $\boldsymbol{r}_2$ being the two electron coordinates. This "baby" insulator is of course nothing but the hydrogen molecule $H^2$. Out of these two single electron functions we can form four two electron functions,

$$\phi_l(\boldsymbol{r}_1)\phi_r(\boldsymbol{r}_2)\,,\ \phi_r(\boldsymbol{r}_1)\phi_l(\boldsymbol{r}_2)\,,\ \phi_l(\boldsymbol{r}_1)\phi_l(\boldsymbol{r}_2)\,,\ \phi_r(\boldsymbol{r}_1)\phi_r(\boldsymbol{r}_2)\,, \tag{4.9}$$

or in obvious "short-hand" notation

$$|lr\rangle\,,\ |rl\rangle\,,\ |ll\rangle\,,\ |rr\rangle. \tag{4.10}$$

Here $\phi_l(\boldsymbol{r})$ and $\phi_r(\boldsymbol{r})$ can be taken to be real functions, giving equivalences like $\langle ll|A|rr\rangle = \langle rr|A|ll\rangle = \langle rl|A|lr\rangle$, where $A$ denotes an arbitrary operator.

The only antisymmetric state that can be constructed out of the states in equation (4.10) is

$$|ASym\rangle = \frac{1}{\sqrt{2(1-X^2)}}\left(|lr\rangle - |rl\rangle\right) \tag{4.11}$$

where $X = \langle l|r\rangle = \int d^3r\phi_l(\boldsymbol{r})\phi_r(\boldsymbol{r})$ is the *overlap* between left and right orbitals. The prefactor simply makes the state normalized, which is easily checked. There are more ways of constructing a symmetric function, but first an observation: the first two *covalent* states in (4.10) are quite different from the last two *ionic* states. In these last states the two electrons are located at the same nucleus, the states then having ionic ($H^-$) character. (That these states do not appear in the triplet state in equation (4.11) is the well-known consequence of the Pauli principle; two electrons with the same spin cannot occupy the same orbit.) For nuclei far apart, the ionic terms must be given rather small probabilities, while if the nuclei are close to each other the terms have large probabilities. In the "general valence bond" (GVB) theory, one optimizes the amount of ionic character in the wave-function for a given internuclear distance by minimizing the energy with respect to a parameter $\lambda$, using the normalized function

$$|Sym\rangle^{GVB} = \frac{1}{N(\lambda)} \left( \left(1+\lambda^2\right) (|lr\rangle + |rl\rangle) + 2\lambda \left(|ll\rangle + |rr\rangle\right) \right). \tag{4.12}$$

The two limiting theories, $\lambda = 0$ and $\lambda = 1$ are called the valence bond (VB) (Heitler-London) theory and the molecular orbital (MO) theory, respectively. The VB state corresponds to having one electron in each of the atomic orbitals,

$$|Sym\rangle^{VB} = \frac{1}{\sqrt{2(1+X^2)}} \left(|lr\rangle + |rl\rangle\right), \tag{4.13}$$

with $|ASym\rangle^{VB} = |ASym\rangle$ in equation (4.11). The MO approach, on the other hand, starts from the two orbitals of the $H_2^+$ molecule (for a review see Ref. [110]):

$$\begin{aligned} \phi_g(\boldsymbol{r}) &= \frac{1}{\sqrt{2(1+X)}} \left(\phi_l(\boldsymbol{r}) + \phi_r(\boldsymbol{r})\right), & (4.14)\\ \phi_u(\boldsymbol{r}) &= \frac{1}{\sqrt{2(1-X)}} \left(\phi_l(\boldsymbol{r}) - \phi_r(\boldsymbol{r})\right), & (4.15) \end{aligned}$$

where the index $g$ means "even" (*gerade*) and the index $u$ means "odd" (*ungerade*). This gives

$$|Sym\rangle^{MO} = |gg\rangle = \frac{1}{2(1+X)} \left(|lr\rangle + |rl\rangle + |ll\rangle + |rr\rangle\right) \tag{4.16}$$

and

$$|ASym\rangle^{MO} = \frac{1}{\sqrt{2}} \left(|gu\rangle - |ug\rangle\right). \tag{4.17}$$

It is easily seen that $|ASym\rangle^{MO} = |ASym\rangle$ as well. Note that $\phi_g(\boldsymbol{r})$ and $\phi_u(\boldsymbol{r})$ are orthogonal and that we do not use the symmetric state $\propto (|gu\rangle + |ug\rangle)$ because it does not treat left and right on an equal basis.

In figure 4.3 we can see how the singlet energy $E_S = \langle Sym|H|Sym\rangle$ for the different states varies with the distance between the nuclei, $H$ being the spin independent Hamiltonian for the hydrogen molecule,

$$\begin{aligned} H &= h_1 + h_2 + \frac{e^2}{r_{12}} + \frac{e^2}{r_{lr}}, & (4.18)\\ h_i &= \frac{p_i^2}{2m} - \frac{e^2}{r_{ir}} - \frac{e^2}{r_{il}}, \qquad i = 1,2. \end{aligned}$$

The curve indicated by $HF$ is from an improved MO calculation, however the description at large distances is still poor.

**Figure 4.3**: Singlet energies $E_S$ (from Ref. [109]).

### 4.2.2 Exchange

Assuming the nuclear distance to be rather large we can use the VB states to extract the essential information. To decide whether we have a ferromagnetic triplet spin state or an antiferromagnetic singlet spin state as the ground state for the hydrogen molecule, we calculate the energy difference between the two states

$$-2J \equiv E_T - E_S = {}^{VB}\langle ASym|H|ASym\rangle^{VB} - {}^{VB}\langle Sym|H|Sym\rangle^{VB}\,, \quad (4.19)$$

with $H$ the Hamiltonian in (4.18). If $J < 0$ we have an antiferromagnetic ground state, while if $J > 0$ we have a ferromagnetic ground state. It is straightforward to calculate that

$$-2J_{lr} = -2\frac{(\mathcal{K}_{lr} - X^2\mathcal{J}_{lr}) - 2X(1-X^2)t_{lr}}{1-X^4} \quad (4.20)$$

where

$$2t_{lr} \equiv E_u - E_g = -2\frac{h_{lr} - Xh_{ll}}{1-X^2} \quad (4.21)$$

with

$$h_{lr} = \int d^3r\phi_l(\boldsymbol{r})h(\boldsymbol{r})\phi_r(\boldsymbol{r}) \quad (4.22)$$

$$h_{ll} = \int d^3r\phi_l(\boldsymbol{r})h(\boldsymbol{r})\phi_l(\boldsymbol{r}) \quad (4.23)$$

and

$$\mathcal{J}_{lr} = \int\int d^3r_1d^3r_2\frac{[\phi_l(\boldsymbol{r}_1)]^2[\phi_r(\boldsymbol{r}_2)]^2}{r_{12}} \quad (4.24)$$

$$\mathcal{K}_{lr} = \int\int d^3r_1d^3r_2\frac{[\phi_l(\boldsymbol{r}_1)\phi_r(\boldsymbol{r}_1)][\phi_l(\boldsymbol{r}_2)\phi_r(\boldsymbol{r}_2)]}{r_{12}}\,. \quad (4.25)$$

The indices $lr$ indicate which atomic functions that are included in the integrals. $\mathcal{J}_{lr}$ is called the Coulomb Integral and $\mathcal{K}_{lr}$ the Exchange Integral. All three quantities $t_{lr}$, $\mathcal{K}_{lr}$ and $\mathcal{J}_{lr}$ can be shown to be positive. (For example the ground state of the $H_2^+$ molecule is the gerade state in equation (4.14), implying that $t_{lr}$ is positive.) Assuming no overlap, $X = 0$, equation (4.20) gives $J_{lr} = \mathcal{K}_{lr}$, and since $J$ is positive the triplet state must be the ground state, implying ferromagnetism. To obtain antiferromagnetism we must have an overlap. Assuming a small overlap, retaining terms up to order $X$, we find

$$J_{lr} = \mathcal{K}_{lr} - 2Xt_{lr} \, . \tag{4.26}$$

We conclude that if the overlap is large enough we will have negative $J_{lr}$ thus finally obtaining an antiferromagnetic state.

### 4.2.3 Superexchange

Given the fact that we need an overlap of electronic orbitals to obtain an antiferromagnetic state, the problem arises how to explain that most of the antiferromagnets have a rather large distance between their magnetic ions. As an example, the magnetic $Cu^{++}$ ions in the copper-oxide planes in the high-$T_c$ superconductors are typically separated by $4 - 5$ Å, the distances between ions in different planes being even larger. This gives minute overlaps, but the ground state at low temperatures is 3D antiferromagnetically ordered anyway, as seen in Fig. 1.1. To understand how this is possible, we need to introduce the idea of *superexchange* [112]. This concept originated with Kramers [113] who tried to understand the early results of adiabatic demagnetization, which indicated that small exchange couplings existed even between ions separated by one or several diamagnetic groups. Kramers pointed out that the magnetic ions could cause spin-dependent perturbations in the wave functions of intervening ions, thereby transmitting the exchange effect over large distances, but no specific mechanisms were discussed. In the light of our present understanding, that we need an overlap to obtain antiferromagnetism, it is clear that we should use other starting wave functions instead of the atomic ones (the $d_{x^2-y^2}$ orbitals in case of the $Cu^{++}$ ion in the $CuO$ planes in the high-$T_c$ superconductors). It is not far-fetched to assume the intervening diamagnetic (filled shells) ions (the $O^{--}$ in the $CuO$ planes) to perturb the atomic orbitals in such a way that the new wave functions do have a rather large overlap. There are various methods of calculating the new wave functions. One way is to reduce the problem to *one* magnetic ion surrounded by a lattice of non-magnetic ions, another to do some sort of cluster calculation. The task of calculating these wave functions in a more and more refined way is still an active area of research. The wave functions in figure 4.4 is the result of a cluster calculation [109]. We see that the wave functions are mostly located at the $Cu^{++}$ ions but some parts are located at the $O^{--}$ ions, producing the required overlap leading to superexchange.

**Figure 4.4**: Some of the orbitals in a $Cu_3O_{10}$ cluster (from Ref. [109]).

### 4.2.4 The spin Hamiltonian

As discussed in Sec. 4.2.1, a spin independent Hamiltonian gives rise to spin and space dependent eigenstates. Of course the opposite is also true; the spin eigenstates of a spin Hamiltonian (as the Heisenberg Hamiltonian) requires certain symmetries of the space part to form the total wave function. If we are only interested in the spin properties of a system, it is sufficient to work with a spin Hamiltonian. Then, which spin Hamiltonian is applicable to the two electron problem? Since

$$\boldsymbol{S}^2 = (\boldsymbol{S}_1 + \boldsymbol{S}_2)^2 = \boldsymbol{S}_1^2 + \boldsymbol{S}_2^2 + 2\boldsymbol{S}_1 \cdot \boldsymbol{S}_2 \tag{4.27}$$

we see that

$$\langle \text{triplet}|2\boldsymbol{S}_1 \cdot \boldsymbol{S}_2|\text{triplet}\rangle = 1(1+1) - \frac{1}{2}(\frac{1}{2}+1) - \frac{1}{2}(\frac{1}{2}+1) = \frac{1}{2}, \tag{4.28}$$

and

$$\langle \text{singlet}|2\boldsymbol{S}_1 \cdot \boldsymbol{S}_2|\text{singlet}\rangle = 0(0+1) - \frac{1}{2}(\frac{1}{2}+1) - \frac{1}{2}(\frac{1}{2}+1) = -\frac{3}{2}. \tag{4.29}$$

The energy difference between the triplet and singlet states can then be written as

$$-2J = E_T - E_S = \langle T|H_{\text{spin}}|T\rangle - \langle S|H_{\text{spin}}|S\rangle \tag{4.30}$$

where

$$H_{\text{spin}} = -2J\boldsymbol{S}_1 \cdot \boldsymbol{S}_2 \tag{4.31}$$

is the Heisenberg Spin Hamiltonian for the two-electron problem.

### 4.2.5 The Heisenberg model

It is a nontrivial task to extend the results above for the two electron system to an $N$-body system, and it would go far beyond the scope of this thesis to discuss the difficulties involved. Let it suffice to say that the "naive extension" of (4.31) to a system of $N$ localized electrons, obtained by summing over pairs of spin operators, in fact is the right one. One thus obtains the Heisenberg Hamiltonian [105, 106]

$$\mathcal{H} = \sum_{\langle ij \rangle} J_{ij} \boldsymbol{S}_i \cdot \boldsymbol{S}_j \,. \tag{4.32}$$

The notation $\langle ij \rangle$ means the link between two lattice points, and the sum is then over all links of the lattice. From now on we redefine the coupling $J_{ij}$ by absorbing the minus sign in (4.31) and dividing by 2. The Heisenberg model is a quantum model, with $\boldsymbol{S}_i$ ($i = 1, \ldots, N$) being vector operators with elements $\boldsymbol{S} = (S^x, S^y, S^z)$ obeying the $SU(2)$ algebra in (4.3). But we can also obtain a classical model by regarding $\boldsymbol{S}$ as a classical vector. The classical model is the limiting model for large spins. This can be seen by writing $\boldsymbol{S}_i$ in terms of the normalized spin operator $\boldsymbol{\Omega}_i$, $\boldsymbol{S}_i = S\boldsymbol{\Omega}_i$, which makes (4.3) to be

$$[\Omega_i^x, \Omega_j^y] = \frac{i}{S} \Omega_i^z \delta_{ij} \,. \tag{4.33}$$

Taking the limit of large spin makes the normalized spin operators commute, i.e. they become classical vectors. One uses this limit to check that approximations made in a calculation are valid at least for large spins.

It is easy to check that the classical ground state of the Heisenberg model is ferromagnetic when $J_{ij} < 0$; any vector pointing in another direction than the rest raises the energy. Already in the classical model, the positive $J_{ij}$ is a trickier problem, but assuming nearest neighbor interaction to be $J_1$, next nearest neighbor interaction to be $J_2$ and so on, and then taking $J_1$ to be much larger than the rest, we obtain an antiferromagnetic ground state. The classical antiferromagnetic ground state is then a state where all nearest neighboring sites have spins (vectors) pointing in opposite directions (assuming a bipartite lattice, see Sec. 4.3.3). For the quantum model, though, this cannot be the appropriate ground state. We can see the problem directly, using the Heisenberg model. By introducing the ladder operators $S^\pm = S^x \pm iS^y$, and writing

$$2\boldsymbol{S}_1 \cdot \boldsymbol{S}_2 = 2S_1^z S_2^z + S_1^+ S_2^- + S_1^- S_2^+ \,, \tag{4.34}$$

it is easy to verify that

$$2\boldsymbol{S}_1 \cdot \boldsymbol{S}_2 | \uparrow\downarrow \rangle = \frac{1}{4} | \uparrow\downarrow \rangle + | \downarrow\uparrow \rangle \,. \tag{4.35}$$

Hence, the "classical antiferromagnetic state" $| \uparrow\downarrow \rangle$ is not an eigenstate of the Heisenberg Hamiltonian.

The quantum analog to the classical antiferromagnetic state is instead defined as a spin eigenstate to the Heisenberg Hamiltonian with a sublattice magnetization different from zero. The sublattice magnetization, $m^{\uparrow\downarrow}$, is in turn defined as the expectation value

$$m^{\uparrow\downarrow} \equiv \sum_i \frac{\langle \epsilon_i S_i^z \rangle}{N} \tag{4.36}$$

with $\epsilon_i$ equal to $+1$ on one sublattice and $-1$ on the other. For the classical state, we can easily see that the sublattice magnetization is $\frac{1}{2}$ (assuming the spin to be that of an electron).

The classical antiferromagnetic ground state is called a *Néel state*, after L. Néel who in 1932 [114] proposed the possibility of antiferromagnetic order. Since the ordered quantum and classical states are quite different, one often specifies the quantum one as a *quantum Néel state*. It is interesting to recall that an antiferromagnet does not have any macroscopic magnetization. In fact it was not until neutron scattering was made available in 1949 that one could detect this type of spontaneous order (see also Sec. 4.6). This is in contrast to ferromagnets which have fascinated and intrigued people from ancient times. (The ferromagnet, in the form of loadstone, appeared in Greek writings around 800 B.C.. In the form of a magnetized needle (compass) it appeared in Chinese writings as early as in the Third Millennium B.C.!)

This thesis, though, concentrates on antiferromagnets and we will now specifically leave place for the fascinating 2D Heisenberg antiferromagnet.

## 4.3 The 2D Heisenberg antiferromagnet

In the preceding sections in this chapter we have discussed how the electron-electron interactions together with the Pauli exclusion principle can give rise to magnetic interactions. The appropriate model to study for an insulating material with magnetic correlations is, as we have seen, the Heisenberg model. In Chapter 1 it was stated that the appropriate magnetic model to study in the context of high-$T_c$ superconductors is the 2D Heisenberg antiferromagnetic model and I also discussed the importance of disordering effects.

I will here continue by introducing the different disordering mechanisms that can drive a transition from an ordered to a disordered state. In this context I will introduce the two models that we have studied, the frustrated 2D Heisenberg model on a honeycomb lattice and the (intrinsically frustrated) 2D Heisenberg model on a triangular lattice.

In contrast to one dimension, where the Heisenberg model is exactly solvable by Bethe's famous Anzats [8], we need to solve these 2D models within some approximate theory and I will motivate our choice of theory in this section.

Let us for the sake of clarity restate Eq. (4.32) in a slightly different form,

$$\mathcal{H} = J_1 \sum_{\substack{\langle ij \rangle \\ nn}} \boldsymbol{S}_i \cdot \boldsymbol{S}_j + J_2 \sum_{\substack{\langle ii' \rangle \\ nnn}} \boldsymbol{S}_i \cdot \boldsymbol{S}_{i'} + \cdots \quad , \tag{4.37}$$

with $J_1, J_2, \ldots$ being the couplings between nearest neighbors (nn), next nearest neighbors (nnn), and so on. The first sum is over links between nearest neighbors (nn), the second is over links between next nearest neighbors (nnn) and so on (see Fig. 4.5).

**Figure 4.5**: Frustrating couplings on a square lattice

We have studied the Heisenberg model on different 2D lattices: in Paper V we studied the model on a honeycomb lattice with $J_1$ and $J_2$ non-zero, while in Paper IV we considered the model on a triangular lattice retaining only the $J_1$ coupling. This difference in the number of couplings included may seem arbitrary, but there are reasons for this as we shall see in the following sections. But before we go one let us first consider the role of the spin magnitude.

### 4.3.1 Magnitude of the spin

As we have already mentioned, fluctuations are enhanced in a quantum antiferromagnet with respect to a classical system which, in fact, has no fluctuations at all (at $T = 0$ where no *thermal* fluctuations are present). The more an antiferromagnetic system is "quantum mechanical" the larger the quantum fluctuations become. This is because the *order parameter* defining the antiferromagnetic state, i.e. the sublattice magnetization in Eq. (4.36), does not commute with the Heisenberg Hamiltonian. The dynamics of a quantity, like the order parameter, is described by the Heisenberg equation of motion,

$$\frac{dm^{\uparrow\downarrow}}{dt} \propto [m^{\uparrow\downarrow}, \mathcal{H}] \tag{4.38}$$

and if the quantity does not commute with the Hamiltonian it is not conserved but is fluctuating. This is exactly what happens in our case. In Eq. (4.33) we saw that, only if the magnitude of the spin, $S$, is infinitely large, the Heisenberg model turns into a classical model where all spin components commute, yielding an order parameter that is conserved. For every finite spin we will have a non-commuting order parameter and thus fluctuations. The importance of quantum fluctuations in a system is thus governed by the magnitude of the spin. The extreme quantum limit, where fluctuations are most pronounced, is when the spin is that of an electron, $S = \frac{1}{2}$. Having established the importance of the magnitude of the spin let us now consider the notion of frustrations.

### 4.3.2 Frustrations

If we examine the Heisenberg antiferromagnet on a *square* lattice, we see, in Fig. 4.5, that with the nearest neighbor (nn) coupling $J_1 > 0$, neighboring spins will align anti-parallel. However, if the next nearest neighbor (nnn) coupling $J_2$ is positive as well, this coupling will also strive towards nnn spins becoming anti-parallel, which is in conflict with the nn coupling. This competition between the nn and the nnn coupling is called *frustration*. Now one could argue that the nnn coupling will probably be ferromagnetic since the overlap between nnn orbitals must be small. This is *not* the case in all compounds, though, as calculations on $La_2CuO_4$ show [115]. These calculations give antiferromagnetic nnn couplings of about $5\% - 8\%$ of the nn couplings[2].

Leaving aside the microscopic origin of frustration, we shall from now on focus on its effects on the order-disorder properties of the system. Let us return to the Heisenberg model on a square lattice in Fig. 4.5. As the nnn coupling is turned larger and larger with respect to the nn coupling, it will eventually drive the initially ordered system to become disordered, with a ground state carrying zero sublattice magnetization. In the limit of $J_2 \gg J_1$ we get a new ordered ground state with each of the two sublattices antiferromagnetically ordered independently. The order-disorder transition of an antiferromagnet is an archetype example of a *quantum phase transition* (for a recent review, see [118]), driven by the enhanced zero-temperature quantum fluctuations due to the competition between nn- and nnn couplings. This transition and the nature of the disordered quantum phase has been an active area of research

[2]People have also proposed that a positive nnn coupling could model the presence of vacancies in the $CuO$ planes of the high-$T_c$ superconductor [116]. Still, the subject is controversial [117].

during the last 5-10 years, and still remains so. In particular, the problem has been extensively studied for the square lattice Heisenberg antiferromagnet. For a review see Ref. [119].

In our work on the honeycomb lattice, Paper V, we explicitly include frustrating couplings of the kind discussed here. However, there are also other ways a system can be frustrated as we shall see next.

### 4.3.3 Lattices

In Sec. 1.1.1 we saw that a 3D antiferromagnet is ordered at zero temperature, whereas the 1D antiferromagnet is disordered. This can be thought of as follows. A spin that is coupled to *many* neighboring spins is less sensitive to a fluctuation of *one* of those spins, as the other (non-fluctuating) neighbors will keep it aligned. The number of nearest neighbors to a lattice point is called the *coordination number* $z$. The smaller the coordination number, the more important are the fluctuations[3]. In 1D the coordination number is always 2, while for a 3D simple cubic lattice it is 6. A 2D square lattice has $z = 4$ and it has been proved that the (unfrustrated) antiferromagnet orders on this lattice for spins $S \geq 1$ [120, 121]. For spin $S = \frac{1}{2}$ there is also believed to be order [122], although no rigorous proof exists. Thus, $z = 2$ gives disorder while $z = 4$ (probably) gives order. What about $z = 3$, then?

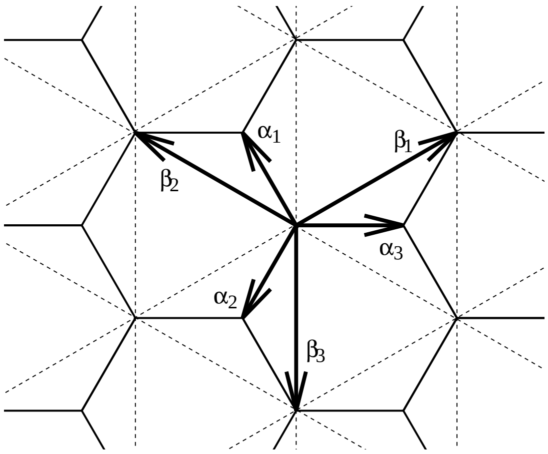


**Figure 4.6**: The honeycomb lattice. One of the two triangular sublattices is marked. The vectors $\boldsymbol{\alpha}$ point to the nearest neighbors of a site while the vectors $\boldsymbol{\beta}$ point to half the number of second nearest neighbors.

[3]Remember that the spin lattice is not always equal to the crystal lattice. This is evident for the solids exhibiting magnetic order by the process of superexchange since every magnetic ion (carrying spin) is surrounded by non magnetic ions which do not carry spin.

The lattice with $z = 3$ is called a *honeycomb lattice*, for obvious reasons, as can be seen in Fig. 4.6[4]. It is a non-Bravais lattice; we have *two* lattice points in each unit cell. Two lattice points in each unit cell imply that the lattice is *bipartite*, i.e. we can divide it in two inter-penetrating sublattices. Each of the sublattices is a triangular Bravais lattice, one of which is indicated in Fig. 4.6. It follows that the classical ground state is a Néel state with neighboring spins oriented 180° relative to each other. It is less clear, however, what happens in the quantum case. Is the 2D honeycomb quantum antiferromagnet ordered or disordered at $T = 0$? This is one of the questions addressed in Paper V.

In Sec. 4.3.2 we talked about frustration; when we let the nnn coupling be much larger than the nn coupling on the square lattice, the two sublattices decouple and become Néel ordered independently. This is also true for the honeycomb lattice with the modification that, since the sublattices are triangular (with $z = 6$, see Fig. 4.7) and therefore *tripartite*, the classical Néel state on each sublattice has a so-called $\sqrt{3} \times \sqrt{3}$ order. In such a state neighboring

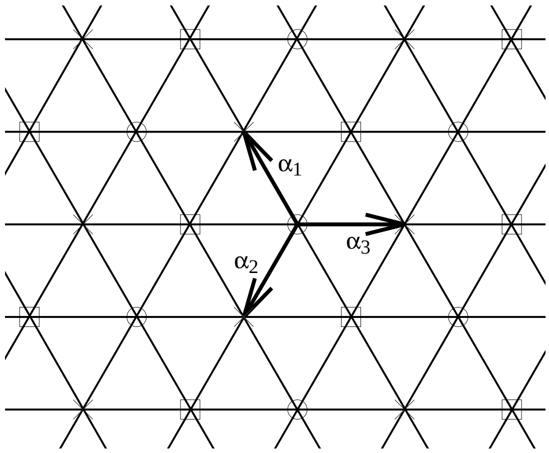


**Figure 4.7**: The triangular lattice. The vectors $\alpha$ are pointing to half the number of nearest neighbors of a site. Sites of the three sublattices are indicated by crosses, squares, and circles, respectively.

spins have an angle of 120° instead of 180° as for the bipartite lattice.

The quantum mechanical ground state of a tripartite lattice such as the triangular is *intrinsically frustrated*. Let us look at it in this way. According to quantum mechanics, only one component of the spin vector can be specified as being either "up" or "down". If we try to place up and down spins in an antiferromagnetic array at the corners of a plaquette on a tripartite lattice

[4]We have here rotated the lattice with respect to the lattice in Paper V for the purpose of making the similarities with the triangular lattice more transparent.

(thus trying to minimize the energy), we can place an up-spin on the first, a down-spin on the second but on the third we do not know whether to place an up- or down-spin. Whatever we do, the resulting state becomes "frustrated" and since the frustration is not due to the couplings but to the very structure of the lattice we call it *intrinsically frustrated*. As we saw above, frustration can drive an ordered quantum state to become disordered, and tripartite lattices (with $\sqrt{3} \times \sqrt{3}$ order in the classical limit) have been studied because of the possibility that they are yet other candidates for 2D disordered quantum antiferromagnets. This is one of the reasons why we have studied the 2D Heisenberg model on the triangular lattice, in Paper IV. (Since the model is already frustrated with a single positive $J_1$-coupling, we do not include further couplings.)

There are other intrinsically frustrated lattices e.g. the *kagomé* lattice shown in figure 4.8. The kagomé lattice has coordination number 4, and is thus

**Figure 4.8**: The kagomé lattice

an even better candidate for a disordered 2D antiferromagnet. The kagomé lattice is tripartite like the triangular lattice, and like the honeycomb lattice the kagomé lattice is non-Bravais. This is another reason for studying the Heisenberg 2D antiferromagnet on triangular and honeycomb lattices. By exploring, one by one, the complications that arise from the fact that the lattice is non-Bravais and non-bipartite, we take a step closer to understanding the intriguing kagomé antiferromagnet [123].

### 4.3.4 The frustrated 2D Heisenberg model on a honeycomb lattice

Let me now introduce the Hamiltonian for the frustrated 2D Heisenberg model on a honeycomb lattice:

$$\mathcal{H} = J_1 \sum_{\boldsymbol{r},\boldsymbol{\alpha}} \boldsymbol{S}_{\boldsymbol{r}} \cdot \boldsymbol{S}_{\boldsymbol{r}+\boldsymbol{\alpha}} + J_2 \sum_{\boldsymbol{R},\boldsymbol{\beta}} \boldsymbol{S}_{\boldsymbol{R}} \cdot \boldsymbol{S}_{\boldsymbol{R}+\boldsymbol{\beta}} \quad , \tag{4.39}$$

with $J_1, J_2 \geq 0$. The first sum runs over all sites $\boldsymbol{r}$ of one sublattice and over the three nearest-neighbor vectors $\boldsymbol{\alpha}$. The next sum, on the other hand, runs over all lattice sites $\boldsymbol{R}$ as well as over three of the six second-nearest-neighbor vectors $\boldsymbol{\beta}$ (see Fig. 4.6).

The honeycomb (spin) lattice is not only interesting as a model candidate for a 2D disordered quantum antiferromagnet. In fact, there exists at least one experimental realization, the compound $BaNi_2(PO_4)_2$ [124]. The crystallographic structure of this compound can be described as a stacking of honeycomb nickel planes, well separated from each other, with the in-plane and inter-plane distances 2.8 and 7.8 Å, respectively. The magnetic $Ni^{2+}$ ions carry spin $S = 1$. The experimental results from this compound cannot, however, be directly compared with our theoretical results, partly because the next next nearest neighbor (nnnn) coupling is shown to be large while in our model we have assumed this coupling to be zero[5].

To “pull out the physics” from the Hamiltonian in Eq. (4.39) is a difficult problem. As we have already mentioned there are (as yet) no exact methods available in two dimensions. Instead one is forced to do some sort of approximation.

The problem stated in Eq. (4.39) has been treated by several methods; extrapolations of finite-lattice diagonalizations [125], Monte Carlo simulations [126], series expansions around the Ising limit [127], and first-order corrections to the spin-wave theory [128]. We have studied the frustrated 2D Heisenberg model on a honeycomb lattice, Eq. (4.39), with the Schwinger-Boson Mean-Field Theory [129, 130] (SBMFT), a theory that has proved successful in incorporating quantum fluctuations. The basic features of the SBMFT will be reviewed in Sec. 4.5.

### 4.3.5 The intrinsically frustrated 2D Heisenberg model on the triangular lattice

The Hamiltonian for the intrinsically frustrated 2D Heisenberg model on the triangular lattice is:

$$\mathcal{H} = J_1 \sum_{\boldsymbol{R},\boldsymbol{\alpha}} \boldsymbol{S}_{\boldsymbol{R}} \cdot \boldsymbol{S}_{\boldsymbol{R}+\boldsymbol{\alpha}} \quad , \tag{4.40}$$

[5]It should in principle be possible to extend our analysis to the case with an added nnnn coupling, allowing for future comparisons with the experimental results.

with $J_1 \geq 0$. The sums run over all lattice sites $\boldsymbol{R}$ and three of the six nearest-neighbor vectors $\boldsymbol{\alpha}$.

This model has been more extensively studied than the model on the honeycomb lattice, and the question whether the ground state is ordered or not has been studied by many authors. Early papers on the triangular HAFM [131, 132] suggested that the spin-$\frac{1}{2}$ ground state is a spin liquid, lacking long-range order (LRO). More recent studies [122, 133, 134, 135, 136, 137] point to the scenario of an ordered ground state possibly quite close to a disordering transition. Yet other studies support the original proposal of a disordered ground state [138, 139].

Efforts to understand the spin dynamics of the model in Eq. (4.40) has been made using a variety of methods, like the linear spin-wave theory (LSWT) [133], a nonlinear $\sigma$-model approach [140], and the Schwinger-boson mean-field theory (SBMFT) [134, 141]. As we have already pointed out, the SBMFT has proved successful in incorporating quantum fluctuations, but the choice of mean-field parameters to be included in this theory for the triangular lattice is a delicate matter [142, 143]. I will return to this problem in the next chapter (in Sec. 5.1.1).

Before we turn to the Schwinger-boson Mean-Field Theory (SBMFT), however, I will shortly describe the more traditional approach of Spin-Wave Theory (SWT).

## 4.4 Spin-wave theory

The Heisenberg model in Eqs. (4.39) and (4.40) is written in terms of the ordinary spin operators $\boldsymbol{S}_i = (S_i^x, S_i^y, S_i^z)$ obeying commutation relations (4.3). Common to both SBMFT and LSWT is a transformation to bosonic degrees of freedom, that is, the Heisenberg Hamiltonian is rewritten in terms of operators obeying the boson commutation relation

$$\left[a_i, a_j^\dagger\right] = \delta_{ij}\,. \tag{4.41}$$

There are different types of SWT starting from different representations of the spin operators. I will here present the most common version based on the Holstein-Primakoff transformation [144].

### 4.4.1 Holstein-Primakoff transformation

The Holstein-Primakoff transformation is defined in terms of the spin-deviation operators $n_i$ as

$$n_i \equiv S - S_i^z \tag{4.42}$$

with eigenvalues $0, 1, \ldots, 2S$. In evaluating the ladder operators in the basis consisting of the eigenvectors of $n_i$, it is convenient, as a bookkeeping device, to introduce operators $a_i$, $a_i^\dagger$ defined by their action on the eigenvectors of $n_i$,

$$\begin{aligned} a_i^\dagger|n_i\rangle &= \sqrt{n_i+1}|n_i+1\rangle\,, \\ a_i|n_i\rangle &= \sqrt{n_i}|n_i-1\rangle\,. \end{aligned} \tag{4.43}$$

One can then show that the $a_i$ are bosons and that

$$S_i^+ = \sqrt{2S}f_S(n_i)a_i\,, \qquad S_i^- = \sqrt{2S}a_i^\dagger f_S(n_i)\,, \qquad S_i^z = S - n_i\,, \tag{4.44}$$

with

$$n_i = a_i^\dagger a_i\,, \tag{4.45}$$

$$f_S(n_i) \equiv \left(1 - \frac{n_i}{2S}\right)^{1/2}\,. \tag{4.46}$$

It is straightforward to show that the Holstein-Primakoff transformation preserves the spin commutation relations in (4.3). In equation (4.43) the eigenvalues $n_i$ are free to take any value from 0 to $\infty$, rather than from 0 to $2S$. There is no contradiction in this, though. The physical states with $0 \le n_i \le 2S$ are not connected with the unphysical ones with $n_i > 2S$ since

$$S_i^-|n_i = 2S\rangle = 0\,, \tag{4.47}$$

as is immediately seen from Eqs. (4.44) and (4.46). This equation for SWT is equivalent to the statement that the Holstein-Primakoff transformation conserves the total spin:

$$\boldsymbol{S}^2 = S(S+1)\,, \tag{4.48}$$

where the identity operator on the right hand side is implicit.

Applying SWT to an antiferromagnetic problem is not completely trivial. We need to take into account that $n_i$ is a spin *deviation* operator and that the deviation should be measured from an appropriate state. If we restrict ourselves to considering deviations from the classical antiferromagnetic state, we must divide the lattice into sublattices with each sublattice having all spins in the classical state pointing in the same direction. Each sublattice in this way needs to have their own set of deviation operators measured from the classical spin. For example, if the lattice is bipartite, the deviation operators can be defined as in Eq. (4.42) for one of the sublattices, while it has to be defined according to $n_j = -S - S_j^z$ on the other sublattice. This *spin rotation* can be done without danger if we at the same time rotate the eigenstates accordingly. We will return to the subject in Sec. 5.1.

The Hamiltonian written in terms of the boson operators in Eq. (4.43), using Eq. (4.44), is a good starting point when doing approximations: first one expands the operator $f_S(n_i)$,

$$f_S(n_i) = 1 - \frac{n_i}{4S} - \frac{n_i^2}{32S^2} - \cdots\,, \tag{4.49}$$

and then truncates the expansion.

### 4.4.2 Linear spin-wave theory

In the linear spin-wave approximation introduced by P. W. Anderson in 1952 [145], one retains in the Hamiltonian only terms up to quadratic in the boson operators. This implies that $f_S(n_i) = 1$, and from Eq. (4.49) we see that this is a good approximation for large spin $S$ (compared to the deviation $n_i$). Since the Heisenberg Hamiltonian by this approximation always becomes quadratic in the bosons it also becomes exactly solvable by the use of a Bogoliubov transformation. The simplicity of the LSWT lies in this fact, and LSWT has been used extensively in all kinds of problem involving the Heisenberg Hamiltonian.

There are problems, though; the LSWT operators only preserve the commutation relations in Eq. (4.3) if $n_i \ll S$. Another drawback of LSWT is that Eq. (4.47) is no longer fulfilled since $f_S(2S)|2S\rangle \neq 0$, and physical and unphysical states become connected. We then have to include the local constraints $0 \leq n_i \leq 2S$ in some other way. This is not easy since the constraints are inequalities and cannot be included with Lagrange multipliers or in any other simple way. One then just ignores including them, relying on the ground state expectation values of $n_i$ to be small, thereby justifying the approximation. The LSWT is then only justified when we have small deviations from the classical Néel state.

I will not state any results for the honeycomb or the triangular lattice here, but leave these results for Chapter 5 where we use LSWT to check our SBMFT results in the large-$S$ limit. We have to compare our results with *some* limit where we have reliable and established results since this is the only way to motivate the validity of an approximate solution. Since for large spin $S$, LSWT should be valid, our SBMFT results must in this limit approach the LSWT results.

## 4.5 Schwinger-boson mean-field theory: introduction

The two models introduced in Sec. 4.3.4 and Sec. 4.3.5 can be studied by several methods. We have chosen to use SBMFT as this approach has proved successful in incorporating quantum fluctuations for the square lattice problem.

The Schwinger-boson mean-field theory is based on the Schwinger boson representation of the spin operators $\boldsymbol{S}$, first formulated by Schwinger in 1952 [146]. The theory was introduced in 1988 by Arovas and Auerbach who used a path-integral formulation to study the square lattice antiferromagnet [129, 130]. The path-integral method was later shown to be equivalent to a Hartree-Fock decoupling of the boson interaction, followed by a mean-field approximation [147, 148]. In the presence of frustrating couplings, the path-integral formulation is not well-defined (due to a "sign problem") and one is forced to use the direct Hartree-Fock decoupling method [149]. This is the approach used in the following.

### 4.5.1 Spin representation by Schwinger bosons

The Schwinger boson representation can be written in a compact form

$$\boldsymbol{S}_i = \frac{1}{2} b^\dagger_{\mu i} \boldsymbol{\sigma}_{\mu\nu} b_{\nu i} \quad , \tag{4.50}$$

where $\boldsymbol{\sigma} = (\sigma^x, \sigma^y, \sigma^z)$ is the vector of Pauli matrices, $b_{\mu i}$ are the *Schwinger bosons* ($\mu = 1, 2$), and summation over repeated (Greek) indices is implied. This form we use in both Papers IV and V. When expanded it becomes

$$S_i^+ = b^\dagger_{1i} b_{2i} \,, \quad S_i^- = b_{1i} b^\dagger_{2i} \,, \quad S_i^z = \frac{1}{2}\left( b^\dagger_{1i} b_{1i} - b^\dagger_{2i} b_{2i} \right) \,, \tag{4.51}$$

where $b_{1i}$ and $b_{2i}$ are independent bosons obeying the commutation relation in (4.41). As is easily checked, the Schwinger boson representation preserves the commutation relations in Eq. (4.3). We also have the constraints

$$b^\dagger_{1i} b_{1i} + b^\dagger_{2i} b_{2i} = 2S \,, \tag{4.52}$$

which follow from requiring Eq. (4.48) to be fulfilled. For a more complete treatment of the Schwinger bosons (or Schwinger oscillators as they are also called), see Ref. [107].

Using Eq. (4.51) to trade the spin operators for bosons, each term in the Heisenberg Hamiltonian (Eq. (4.37)) will consist of two-boson interactions. Note that the constraints in Eq. (4.52) can easily be included in the Hamiltonian in Eq. (4.37) by Lagrange multipliers. The next step is to introduce *link operators* in order to write the Hamiltonian on the form (neglecting constant terms)

$$\begin{aligned} \mathcal{H} &= C_{\mathcal{A}} \sum_{\langle ij \rangle_{\mathcal{A}}} \mathcal{W}^{\mathcal{A}}_{ij} + C_{\mathcal{B}} \sum_{\langle ij \rangle_{\mathcal{B}}} \mathcal{W}^{\mathcal{B}}_{ij} + \cdots + \\ & \quad + \sum_i \lambda_i [b^\dagger_{\mu i} b_{\mu i} - 2S] \,, \end{aligned} \tag{4.53}$$

where we have included the constraints by Lagrange multipliers $\lambda_i$ on every site, $C_{\mathcal{X}}$, $\mathcal{X} = \mathcal{A}, \mathcal{B}, \ldots$ are constants, and

$$\mathcal{W}^{\mathcal{X}}_{ij} \propto \mathcal{X}^\dagger_{ij} \mathcal{X}_{ij} \quad , \tag{4.54}$$

with $\mathcal{X}_{ij}$ a link operator composed of terms *quadratic* in the bosons. The summations in Eq. (4.53) are over links $\langle ij \rangle_{\mathcal{X}}$ where the link operator $\mathcal{X}_{ij}$ is defined. As an example, in the unfrustrated model on the square lattice [129, 130] the link operator

$$\mathcal{A}_{ij} \equiv b_{1i}b_{1j} + b_{2i}b_{2j} \,. \tag{4.55}$$

is a standard choice and the summation is over nearest-neighbor links. To arrive at the form of the Hamiltonian in Eq. (4.53) is not entirely trivial; one needs to perform a proper spin rotation and also exploit the constraint in Eq. (4.52). The link operators can more generally be chosen in several ways and sometimes the choice is intricate. Not to complicate matters, let us here leave the discussion of this point to Sec. 5.1.1 and for now simply assume the Hamiltonian to be of the form in Eq. (4.53).

### 4.5.2 Hartree-Fock decoupling

We now introduce the first SBMFT approximation, a Hartree-Fock decoupling, and write the link operators $\mathcal{X}_{ij}$ in Eqs. (4.53) and (4.54) as

$$\mathcal{X}_{ij} = \langle \mathcal{X}_{ij} \rangle + (\mathcal{X}_{ij} - \langle \mathcal{X}_{ij} \rangle) \;. \tag{4.56}$$

By neglecting the terms

$$(\mathcal{X}_{ij} - \langle \mathcal{X}_{ij} \rangle)^2 \;, \tag{4.57}$$

we arrive at

$$\mathcal{X}_{ij}^\dagger \mathcal{X}_{ij} \to \mathcal{X}_{ij}^\dagger \langle \mathcal{X}_{ij} \rangle + \langle \mathcal{X}_{ij}^\dagger \rangle \mathcal{X}_{ij} - \langle \mathcal{X}_{ij}^\dagger \rangle \langle \mathcal{X}_{ij} \rangle \,. \tag{4.58}$$

Let us examine what this approximation implies. Taking the expectation value of (4.57),

$$\langle (\mathcal{X}_{ij} - \langle \mathcal{X}_{ij} \rangle)^2 \rangle = \langle \mathcal{X}_{ij}^2 \rangle - \langle \mathcal{X}_{ij} \rangle^2 \,, \tag{4.59}$$

we see that it is equivalent to assuming that the variance of the link field is sufficiently small to be neglected. Note that the variance is an expectation value and thus independent of any spin rotation. In the classical limit the Hartree-Fock decoupling is exact since the variance of a classical quantity is zero. However, the more the system is quantum mechanical, the larger the variance may be. If the state $|\;\;\rangle$ is an eigenstate of the operator $\mathcal{X}_{ij}$, though, the variance is always zero also in the extreme quantum limit $S = \frac{1}{2}$. If we have an eigenstate of the Hamiltonian that is not a simultaneous eigenstate of the link operators (as we usually have due to additional approximations as well as the addition of the constraint to the Hamiltonian), the important thing to notice is that our approximation only needs to be valid *locally*, since the link field is a local object. This is in contrast to the LSWT where the approximation only is valid if the deviations from a *global* quantization axis are small. In Fig. 4.9 I have tried to illustrate the difference between deviations from global and local order.

**Figure 4.9**: Examples of (a) global and (b) local Néel order

### 4.5.3 Mean-field theory

The next approximations are to take the expectation values of the link fields to be real and uniform over the lattice,

$$\langle \mathcal{X}_{ij} \rangle = Q_{\mathcal{X}} \, , \tag{4.60}$$

and to replace the local constraints by a global one by taking

$$\lambda_i = \lambda \, , \tag{4.61}$$

$Q_{\mathcal{X}}$ and $\lambda$ being real constants. This last approximation is a dangerous one. In fact, for some of the calculated values, we have to compensate for this approximation "by hand", guided by certain sum rules [129, 130]. The other approximation in Eq. (4.60) only tells us that the local order is the same all over the lattice, which is a reasonable assumption for a homogeneous system.

Using the above approximations, we will always arrive at a Hamiltonian quadratic in the bosons and, as we stated in the case of LSWT, Hamiltonians quadratic in the bosons can always be diagonalized by a Bogoliubov transformation.

### 4.5.4 Free energy

Our mean-field treatment above introduced parameters $Q_{\mathcal{X}}$, and $\lambda$ which must be determined. The way to determine them is to give them the values that minimize the free energy of the system. The free energy is defined as

$$F = -\frac{1}{\beta} \ln Z \, , \tag{4.62}$$

where $Z$ is the partition function

$$Z = \sum_{(\text{states})} \exp(-\beta E_n), \tag{4.63}$$

$\beta$ being the inverse temperature and $E_n$ the energy of state $n$. Already here we see that SBMFT yields a temperature dependence in the theory. As we are mainly interested in the $T = 0$ properties of the system, these will have to be determined by extrapolating the results to zero temperature, or, alternatively by doing the extrapolation already in the equations that determine the mean-field parameters. On the other hand, having access to the finite-$T$ equations gives us the opportunity to also determine certain finite-temperature properties of the system, important for comparison with experiments. In particular one can calculate the dynamic structure factor which can be used to predict the outcome of neutron scattering experiments as we shall see next.

## 4.6 Dynamic structure factor: connection to experiment

Neutron scattering is a standard experimental tool for the study of magnetic properties of condensed matter. Thermal neutrons have both wavelength and energy comparable to the wavelength and energy of, for example, spin-wave excitations. Neutrons are charge neutral and therefore not affected by charge distributions, but a neutron possesses spin and can therefore probe spin distributions.

In an experiment, neutrons (from e. g. a nuclear reactor) with well defined energy and momentum are scattered against a sample, and the momentum and energy distributions of the outgoing neutrons are measured. The observed spectra are proportional to the *differential scattering cross section* which is defined as the scattering intensity per unit solid angle per unit incident flux. Neutrons will be scattered by the crystal ions even if these have no net spin (via nuclear scattering), but our interest is the other way in which a neutron can interact with the crystal, that is, magnetic dipole-dipole interaction. For such an interaction the differential scattering cross section becomes proportional to the *dynamic structure factor*, $\mathcal{S}_{\nu\mu}(\boldsymbol{q}, \omega)$, (for details, see [150])

$$\frac{d^2\sigma}{d\Omega dE} \propto \sum_{\nu,\mu} (\delta_{\nu\mu} - \hat{q}_\nu \hat{q}_\mu) \mathcal{S}_{\nu\mu}(\boldsymbol{q}, \omega) \tag{4.64}$$

where the proportionality constant is dependent on the (known) properties of the incoming and outgoing neutrons, $\boldsymbol{q}$ is the momentum difference and $\omega$ the energy difference between incoming and outgoing neutrons. Here $\nu, \mu =$

$x, y, z$ and $(\hat{q}_x, \hat{q}_y, \hat{q}_z)$ is a unit vector along $\boldsymbol{q}$. The dynamic structure factor, $\mathcal{S}_{\nu\mu}(\boldsymbol{q}, \omega)$, is defined as

$$\mathcal{S}_{\nu\mu}(\boldsymbol{q}, \omega) \equiv \frac{1}{2\pi} \int dt e^{i\omega t} \langle S_\nu(\boldsymbol{q}, t) S_\mu(-\boldsymbol{q}, 0) \rangle \tag{4.65}$$

where $S_\nu(\boldsymbol{q}, t)$ is the $\nu$-component of the spin

$$\boldsymbol{S}(\boldsymbol{q}, t) = \sum_{\boldsymbol{R}} e^{i\boldsymbol{q}\cdot\boldsymbol{R}} \boldsymbol{S}_{\boldsymbol{R}}(t) \,. \tag{4.66}$$

Here the sum runs over *all* sites of the lattice (implying that $\boldsymbol{S}(\boldsymbol{q}, t)$ is a spatial Fourier transform of $\boldsymbol{S}_{\boldsymbol{R}}(t)$ *only* if the lattice is Bravais). Note that the three different coordinate systems, the spin coordinates $\boldsymbol{S}$, the lattice coordinates $\boldsymbol{R}$, and the neutron scattering coordinates $\boldsymbol{q}$, are connected to each other by these equations. The neutron spectrum will thus depend on the relative orientation of the spin, the lattice and the neutron scattering vector.

It is customary to divide the differential scattering cross section into two parts, the Bragg part and the diffuse part:

$$\left(\frac{d^2\sigma}{d\Omega dE}\right)_{\text{Bragg}} \propto \sum_{\nu,\mu} (\delta_{\nu\mu} - \hat{q}_\nu \hat{q}_\mu) \delta(\omega) \langle S_\nu(\boldsymbol{q}) \rangle \langle S_\mu(-\boldsymbol{q}) \rangle \,, \tag{4.67}$$

$$\begin{aligned} \left(\frac{d^2\sigma}{d\Omega dE}\right)_{\text{diffuse}} \propto & \sum_{\nu,\mu} (\delta_{\nu\mu} - \hat{q}_\nu \hat{q}_\mu) \frac{1}{2\pi} \int dt e^{i\omega t} \times \\ & \times \left[ \langle S_\nu(\boldsymbol{q}, t) S_\mu(-\boldsymbol{q}, 0) \rangle - \langle S_\nu(\boldsymbol{q}) \rangle \langle S_\mu(-\boldsymbol{q}) \rangle \right] \,. \end{aligned} \tag{4.68}$$

To elucidate the role of the Bragg contribution we note that in the classical Heisenberg model this will be the only contribution, as we have a static non-fluctuating ground state in the classical limit of large spin. Moreover, the classical Néel-ordered state on the honeycomb and on the triangular lattices will both have Bragg peaks according to

$$\left(\frac{d^2\sigma}{d\Omega dE}\right)_{\text{Bragg}} \propto \delta(\boldsymbol{q} - \boldsymbol{K}) \left\{ \begin{array}{lll} 0 & 2m_1 + m_2 & = 3n \\ \frac{3}{2} & 2m_1 + m_2 & = 3n \pm 1 \end{array} \right. \tag{4.69}$$

where $\boldsymbol{K}$ is a reciprocal lattice vector, $\boldsymbol{K} = m_1 \frac{4\pi}{3} \hat{x} + m_2 \frac{4\pi}{3} (\frac{1}{2}\hat{x} - \frac{\sqrt{3}}{2}\hat{y})$ with $m_1$ and $m_2$ integers.[6] We see that the neutron scattering spectrum will show peaks at well defined values of $\boldsymbol{q}$, the antiferromagnetic points $2m_1+m_2 = 3n\pm 1$. It is not surprising that the two lattices show similar neutron scattering spectra for their antiferromagnetic states since both lattices show similar *magnetic* structures (see Fig. 4.10). Both lattices have ferromagnetically arranged triangular

[6] We have here assumed the classical spin vectors of the honeycomb lattice to be orthogonal to the lattice plane thereby avoiding any coincidental washing out of peaks due to a vanishing prefactor. We thus obtain the maximum number of peaks: If some of the peaks are missing in the spectrum this can give information about the orientation of the spins. For the triangular lattice the prefactor can never vanish.

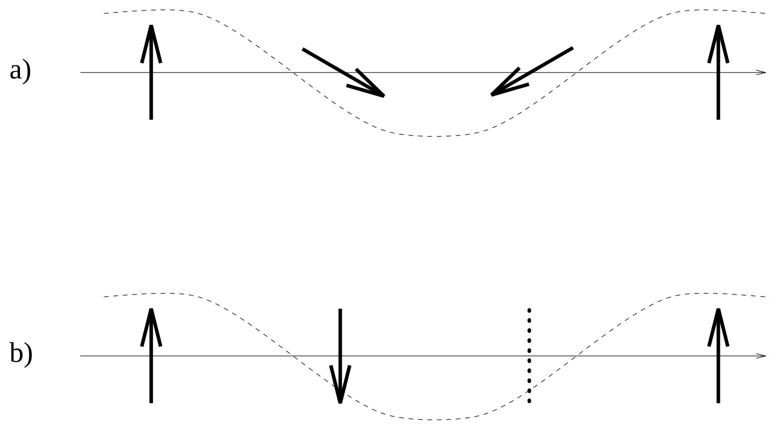


**Figure 4.10**: A neutron wavelength giving constructive interference for both a) triangular and b) honeycomb lattices with classical antiferromagnetic ground states. Note the missing spin in b) indicating the missing sublattice in the honeycomb lattice with respect to the triangular lattice.

sublattices of the same size (we have assumed the nearest neighbor distance to be equal on the two lattices). We will return to the similar antiferromagnetic structure of the two lattices in Sec. 5.1.2.

For a ferromagnetic ground state, in contrast, the Bragg peaks will differ for a honeycomb and a triangular lattice. This is due to the lack of a sublattice in the honeycomb lattice which will ruin the perfect destructive interference at the antiferromagnetic points obtained for the triangular lattice. Both lattices will have their strongest peaks at the ferromagnetic points, $2m_1 + m_2 = 3n$.

In a real experiment the neutron scattering spectrum will also show contributions from the neutrons scattering against the nuclei, and the geometrical difference of the honeycomb and the triangular lattices will, of course, show up in the total spectrum even though the contributions from the magnetic scattering of an antiferromagnetic state will be identical (up to an overall factor). The different contributions to the total spectrum can be separated by several means, for example, by measurements on the sample at two different temperatures. Provided the crystal structure is the same at the two temperatures the spectra well above and below the Néel temperature will only differ in terms of magnetic contribution. Below the Néel temperature, the Bragg peaks should be seen while well above the Néel temperature, where no antiferromagnetic order is present, no Bragg peaks will appear.

We have until now discussed the classical contribution to the Bragg peaks of the magnetic spectrum. The classical Bragg peaks in the spectrum will remain as long as we have an ordered state. However, due to quantum fluctuations always present in the antiferromagnetic state, the peaks will broaden as a result of contributions from the diffuse part.

The diffuse part of the neutron spectrum will also show contributions from *excitations* and in this context we will return to the dynamic structure factor in 5.4.2.

# 5 Antiferromagnets: My Work

In the previous chapter we have seen that the order-disorder transition at $T = 0$ in the Heisenberg antiferromagnet is governed by the magnitude of the spin, the frustrating couplings, and the coordination number of the lattice. In this chapter I will present our work in this context. We have studied the 2D Heisenberg antiferromagnet on two different lattices: the honeycomb lattice (Paper V) and the triangular lattice (Paper IV). The honeycomb lattice is the 2D lattice with the smallest possible coordination number, $z = 3$, and is thus the best candidate for exhibiting a disordered ground state. In the honeycomb lattice antiferromagnet we have also included frustrating next-nearest neighbor couplings in order to more fully explore the stability of the classical Néel state against quantum fluctuations. The model on the triangular lattice is intrinsically frustrated and thus also a candidate for displaying a disordered ground state, although the coordination number here is $z = 6$. Both models are investigated for all magnitudes of spin with emphasis on $S = \frac{1}{2}$, the extreme quantum limit where quantum fluctuations are most pronounced.

We have attacked the problem by using two different approaches: the Schwinger-boson mean-field theory (SBMFT) and the linear spin-wave theory (LSWT). The SBMFT is an improvement compared to LSWT since the theory is spin rotationally invariant and only requires *local* antiferromagnetic order. In contrast, in LSWT one assumes small deviations from a (global) classical Néel state, which is a much stronger assumption, possibly valid only at $T = 0$ (recall the Mermin-Wagner theorem that states that, in 2D, order can only exist at $T = 0$). We have used the large-spin LSWT as a test of our SBMFT results. As we discussed in the previous chapter, in the limit of large spin we must reproduce the LSWT results since here LSWT is the correct solution. Most of the LSWT results are known from the literature, but the calculation of the critical spin vs. frustration on the honeycomb lattice (Fig. 5.4, Fig. 5 of Paper V) is here done for the first time.

Our SBMFT study of the 2D Heisenberg model on a honeycomb lattice is the first of its kind performed on a non-Bravais lattice. As we shall see in Sec. 5.1.2, the breaking of translational invariance requires certain new elements in the analysis. In contrast, SBMFT studies of the 2D Heisenberg model on the triangular lattice have been performed previously [134, 141] but since these studies do not recover the LSWT results (or any other known solution) in the classical limit of large spin, their validity remains an open question. At a theoretical level, to recover a known solution in some limit is a way of justifying approximations made. Comparison with experiments can lead us to reject or accept (provisionally) a theoretical *model* but does not bear directly on the validity of an approximation scheme used to pull out the observables from the model. This must instead be decided *within* a theoretical or mathematical framework.

Our first aim is to construct the proper mean-field Hamiltonians for the honeycomb and triangular lattice Heisenberg antiferromagnets, using SBMFT. The special features that show up for each case (the non-bipartite structure of the triangular lattice and the non-Bravais character of the honeycomb lattice) will be discussed in the next section. In Sec. 5.2, I then discuss some properties of the diagonal mean-field Hamiltonians thus obtained, as well as how to determine the relevant SBMFT parameters. The main results generated by our approach are discussed in Sec. 5.3 (triangular lattice) and Sec. 5.4 (honeycomb lattice). I close the chapter with some conclusions regarding the models studied, as well as regarding the SBMFT.

## 5.1 Schwinger-boson mean-field theory adapted to honeycomb and triangular lattices

In short, the SBMFT is a method to obtain a solvable (mean-field) Hamiltonian, with only terms quadratic in bosons, from the Heisenberg Hamiltonian. The key to success is to rewrite the Heisenberg Hamiltonian in terms of link operators (see Eq. (4.53)), exploiting the Schwinger representation of the spin operator $\boldsymbol{S}$. In the next section (Sec. 5.1.1) I will discuss spin rotations and in this context I will motivate our choice of link operators, in particular for the 2D Heisenberg model on the triangular lattice where this choice is tricky.

Throughout the thesis I have emphasized that a Hamiltonian quadratic in boson fields can always be diagonalized. This is done by going over to $\boldsymbol{k}$-space via Fourier transforms, and in Sec. 5.1.2 I will discuss some special features connected to Fourier transforms on a non-Bravais lattice, such as the honeycomb lattice. Later in the diagonalization process the non-Bravais character of the honeycomb lattice forces us to use a *complex* Bogoliubov transformation which is shortly reviewed in Sec. 5.1.3. The resulting diagonal Hamiltonians for the 2D Heisenberg model on honeycomb and triangular lattices derived within SBMFT and LSWT are presented in Sec. 5.2.

### 5.1.1 Spin rotation: with the example of the triangular lattice, a non-bipartite lattice

The Heisenberg antiferromagnetic model on the triangular lattice has been studied with SBMFT by Yoshioka and Miyazaki [134] and Lefmann and Hedegård [141]. Yoshioka and Miyazaki use a link operator connected to a so-called resonant valence bound ground state, while Lefmann and Hedegård in addition include a ferromagnetic link operator. Both approaches have the drawback that the large spin limit (classical magnetism) does not come out right. Specifically, none of the studies recover the three massless modes in the LSWT dispersion relation for large spin.

We have used another choice of link operators, better suited for investigating the spin-wave dynamics when the ground state is assumed to be close to the classical ground state (see Fig. 4.10). The classical ground state for a tripartite lattice is, as we saw in Sec. 4.3.3, the $\sqrt{3}\times\sqrt{3}$-state where neighboring spins have an angle of 120° with respect to each other. The link operators are identified from the spin rotated Hamiltonian which is obtained by rotating spins on neighboring sublattices by +120° around the $y$ axis when going from $\boldsymbol{R}$ to $\boldsymbol{R}+\boldsymbol{\alpha}$:

$$
\begin{aligned}
S^x_{\boldsymbol{R}} &\rightarrow \cos(\boldsymbol{Q}\cdot\boldsymbol{R})S^x_{\boldsymbol{R}} + \sin(\boldsymbol{Q}\cdot\boldsymbol{R})S^z_{\boldsymbol{R}} \ , && (5.1)\\
S^y_{\boldsymbol{R}} &\rightarrow S^y_{\boldsymbol{R}} \ , && (5.2)\\
S^z_{\boldsymbol{R}} &\rightarrow \cos(\boldsymbol{Q}\cdot\boldsymbol{R})S^z_{\boldsymbol{R}} - \sin(\boldsymbol{Q}\cdot\boldsymbol{R})S^x_{\boldsymbol{R}} \ , && (5.3)
\end{aligned}
$$

where $\boldsymbol{Q}$ is defined by $\boldsymbol{Q}\cdot\boldsymbol{\alpha} = \frac{2\pi}{3} + 2\pi n$, $n$ being an integer and $\boldsymbol{\alpha}$ the nearest neighbor vectors in Fig. 4.7. This implies that the summand of the Hamiltonian in Eq. (4.40) transforms according to

$$
\begin{aligned}
\mathbf{S}_{\boldsymbol{R}}\cdot\mathbf{S}_{\boldsymbol{R}+\boldsymbol{\alpha}} \rightarrow\ & \frac{\sqrt{3}}{2}\left(S^z_{\boldsymbol{R}}S^x_{\boldsymbol{R}+\boldsymbol{\alpha}} - S^x_{\boldsymbol{R}}S^z_{\boldsymbol{R}+\boldsymbol{\alpha}}\right)\\
& - \frac{1}{2}\left(S^z_{\boldsymbol{R}}S^z_{\boldsymbol{R}+\boldsymbol{\alpha}} + S^x_{\boldsymbol{R}}S^x_{\boldsymbol{R}+\boldsymbol{\alpha}}\right) + S^y_{\boldsymbol{R}}S^y_{\boldsymbol{R}+\boldsymbol{\alpha}} \,. \qquad (5.4)
\end{aligned}
$$

The basis states are transformed accordingly, thus making the rotated and unrotated model equivalent. The choice of basis is just a matter of convenience and gives us the opportunity to identify which terms in the Hamiltonian that are relevant, as we shall see now. Let us pick a specific classical Néel state, with the (unrotated) spins on the first sublattice pointing in the $z$-direction while on the other two sublattices they span the $x-z$ plane with directions −120° (+120°) with respect to the $z$-axis when going in the $\boldsymbol{\alpha}$ ($-\boldsymbol{\alpha}$) direction in the lattice (see Fig. 4.10). We immediately see that the spin rotation in Eqs. (5.1)-(5.3) transfers this classical Néel state into a ferromagnetic state with quantization axis lying in the $x-z$ plane. The first term in Eq. (5.4) vanishes when acting on a ferromagnetic state, and we may hence neglect it when modeling states with a local structure close to a 120° state. This gives us an *effective* Hamiltonian for the triangular lattice antiferromagnet:

$$\mathcal{H} = J_1 \sum_{\boldsymbol{R},\boldsymbol{\alpha}} -\frac{1}{2}\left(S^z_{\boldsymbol{R}} S^z_{\boldsymbol{R}+\boldsymbol{\alpha}} + S^x_{\boldsymbol{R}} S^x_{\boldsymbol{R}+\boldsymbol{\alpha}}\right) + S^y_{\boldsymbol{R}} S^y_{\boldsymbol{R}+\boldsymbol{\alpha}}\,. \tag{5.5}$$

This Hamiltonian can now be written on the SBMFT form in Eq. (4.53) using the two link operators,

$$\mathcal{A}_{\boldsymbol{R},\boldsymbol{\alpha}} \equiv b_{1\boldsymbol{R}} b_{1\boldsymbol{R}+\boldsymbol{\alpha}} + b_{2\boldsymbol{R}} b_{2\boldsymbol{R}+\boldsymbol{\alpha}}\,, \tag{5.6}$$

$$\mathcal{B}_{\boldsymbol{R},\boldsymbol{\alpha}} \equiv b^\dagger_{1\boldsymbol{R}} b_{1\boldsymbol{R}+\boldsymbol{\alpha}} + b^\dagger_{2\boldsymbol{R}} b_{2\boldsymbol{R}+\boldsymbol{\alpha}}\,. \tag{5.7}$$

The model on the honeycomb lattice can in a similar way be written in terms of properly chosen link operators. In this case the procedure is less involved and after a rotation of the spins of $\pi$ around the $y$-axis on one of the sublattices, the Hamiltonian for the honeycomb lattice can be written in terms of link operators with the same form as in Eqs. (5.6) and (5.7), the only difference being that the nearest neighbor vector $\boldsymbol{\alpha}$ in Eq. (5.7) is replaced by the next-nearest neighbor vector $\boldsymbol{\beta}$, $\mathcal{B}_{\boldsymbol{R},\boldsymbol{\beta}}$. By this we conclude that the link operator in Eq. (5.7), $\mathcal{B}$, represents the frustration while the link operator in Eq. (5.6), $\mathcal{A}$, represents the quantum antiferromagnetic order corresponding to the *bipartite* classical Néel state. Note that in the model on the triangular lattice, both link operators are present although no explicit frustrating coupling is included. This is of course a manifestation of the intrinsic frustration of the triangular lattice.

By a Hartree-Fock decoupling and a mean-field approximation, as described in Secs. 4.5.2 and 4.5.3, we arrive at Hamiltonians quadratic in the bosons. Such quadratic Hamiltonians are also obtained within LSWT (see Sec. 4.4.2) and in the next section I will briefly describe the diagonalization procedure for this type of Hamiltonians.

### 5.1.2 Fourier transform: with the example of the honeycomb lattice, a non-Bravais lattice

The next step is to Fourier transform the bosons. In the case of a *non-Bravais* lattice this requires some care since a Fourier transform needs to be defined on a Bravais lattice in order to be well-defined. We thus need to have different Fourier transforms on the different Bravais sublattices of the full non-Bravais lattice. Since every sublattice is Bravais also for a Bravais lattice, such as the triangular lattice, we can, in fact, use different Fourier transforms on the different sublattices when diagonalizing the Hamiltonian for this case as well (and this will turn out to be useful).

We thus use

$$b_{\mu \boldsymbol{R}_r} = \frac{1}{\sqrt{N_0}} \sum_{\boldsymbol{k}} e^{-i\boldsymbol{k}\cdot\boldsymbol{R}_r} a_{r\mu\boldsymbol{k}} \quad , \quad r = 1, \ldots, R \quad , \tag{5.8}$$

with $\boldsymbol{R}_r$ on the $R$ different sublattices, respectively, and $N_0$ the number of sites on one sublattice[1]. In LSWT one boson on each site of the lattice is used and this implies $\mu = 1$. In SBMFT, in contrast, two bosons per site are used and $\mu = 1, 2$. In Fig. 5.1, the small hexagon represents the Brillouin zone

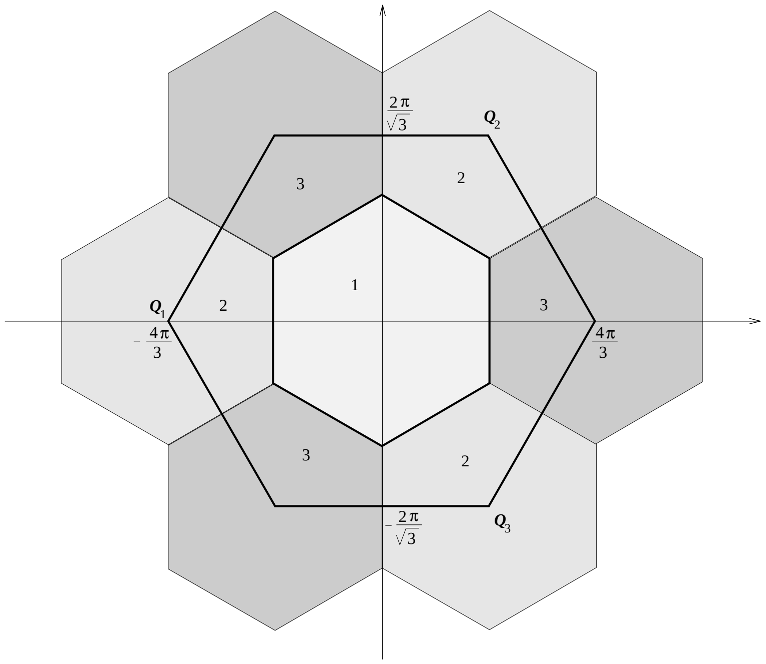


**Figure 5.1**: The Brillouin zones of the honeycomb lattice (small) and the triangular lattice (large). The numbers 1 to 3 indicate the parts of the single triangular mode in the large Brillouin zone that correspond to the three different triangular modes in the small Brillouin zone. The three vectors $\boldsymbol{Q}$ are magnetic reciprocal lattice vectors, pointing to three of the antiferromagnetic points.

of the honeycomb lattice, that is, the reciprocal Wigner-Seitz unit cell of a triangular sublattice. The Brillouin zone of the full triangular lattice is the large hexagon but since we use independent Fourier transforms on the different sublattices also in the triangular case we obtain *three modes* in the smaller cell, equivalent to having one mode in the larger cell. In Fig. 5.1 are also shown three possible vectors $\boldsymbol{Q}$ fulfilling the requirement stated in connection to Eqs. (5.1), (5.2), and (5.3). These vectors are reciprocal lattice vectors for the magnetic structure and are chosen to correspond to antiferromagnetic points as described

[1]The prefactor in Eq. (11) in Paper IV should be $\frac{1}{\sqrt{N/3}}$ since $N_0 = N/3$ on a tripartite lattice.

in Sec. 4.6. Since the antiferromagnetic structures of the lattices are connected to the sublattices we can interpret the honeycomb and the triangular lattices as *the same lattice but with different bases* (see Fig. 5.2). In this picture the

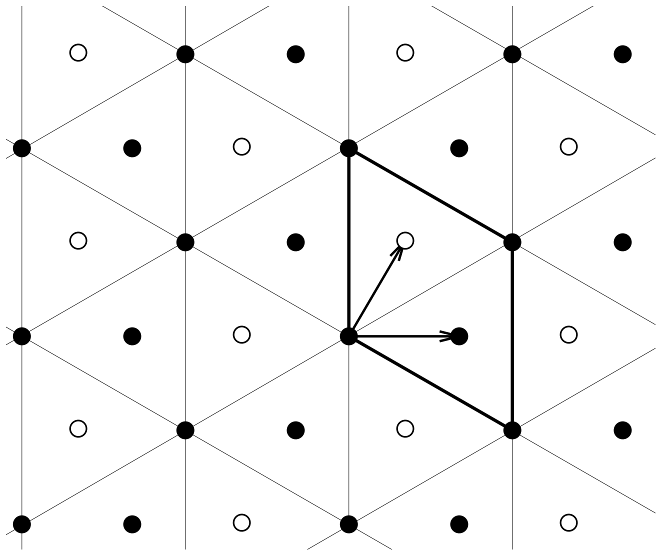

**Figure 5.2**: The triangular and the honeycomb lattices constructed from the same lattice with different bases. The two black lattice points in the unit cell define the basis for the honeycomb lattice while the addition of the white lattice point gives the basis for the triangular lattice.

magnetic structure is connected to the magnetic reciprocal lattice unit cell, the small hexagon, while the basis gives a *magnetic structure factor* that vanishes at the ferromagnetic points (see Sec. 4.6). The larger Brillouin zone of the full triangular lattice sets the upper limit of momenta that is needed to probe the smallest length of both systems and, thus, all information about the systems will be seen inside the larger zone. The information provided by the dynamic structure factor for the honeycomb lattice near the antiferromagnetic points will be discussed in Sec. 5.4.2.

### 5.1.3 Complex Bogoliubov transformation

After this tour in $\boldsymbol{k}$-space we return to the issue of how to diagonalize Hamiltonians quadratic in bosons. After Fourier transforming we have Hamiltonians that are diagonal in the $\boldsymbol{k}$-index but we still have off-diagonal elements in the different kinds of boson (indexed by $r$ and $\mu$, see Eq. (5.8)). To get rid of these we have two tools at our disposal: ordinary unitary transformations among the creation operators and Bogoliubov transformations among pairs of a creation *and* an annihilation operator. The unitary transformations are well-known as are the standard Bogoliubov transformations. In the case of the honeycomb lattice, however, a *complex* Bogoliubov transformation is needed which I will briefly describe. At this stage in the diagonalization process we have a Hamiltonian composed of terms of the type

$$\mathcal{H}_{\boldsymbol{k}} = A_{\boldsymbol{k}} \left( a_{\boldsymbol{k}}^\dagger a_{\boldsymbol{k}} + b_{\boldsymbol{k}} b_{\boldsymbol{k}}^\dagger \right) + B_{\boldsymbol{k}} a_{\boldsymbol{k}} b_{\boldsymbol{k}} + B_{\boldsymbol{k}}^\dagger a_{\boldsymbol{k}}^\dagger b_{\boldsymbol{k}}^\dagger \,, \tag{5.9}$$

where $a_{\boldsymbol{k}}$ and $b_{\boldsymbol{k}}$ denote bosons with different sets of indices $r$ and $\mu$ (on the honeycomb (triangular) lattice we have four (six) kinds of boson in SBMFT, while we have two (three) in LSWT). As is well-known, a Hamiltonian must be Hermitian, which implies that $A_{\boldsymbol{k}}$ must be real. But we also see that $B_{\boldsymbol{k}}$ is *not* required to be real by Hermiticity and, actually, the non-Bravais structure of the honeycomb lattice manifests itself in complex parameters $B_{\boldsymbol{k}}$. This is so since the phase acquired when Fourier transforming a link in the $\boldsymbol{\alpha}$ direction is not paired with a phase of opposite sign from a link in the opposite direction in the lattice (see Fig. 4.6). The appearance of complex $B_{\boldsymbol{k}}$ implies that we need a complex Bogoliubov transformation to diagonalize this kind of Hamiltonian. Such a Bogoliubov transformation can be written as

$$\begin{aligned} a_{\boldsymbol{k}} &= \exp\left(-i\phi_{\boldsymbol{k}}\right) \cosh\theta_{\boldsymbol{k}} c_{\boldsymbol{k}} - \sinh\theta_{\boldsymbol{k}} d_{\boldsymbol{k}}^\dagger \\ b_{\boldsymbol{k}} &= \exp\left(-i\phi_{\boldsymbol{k}}\right) \cosh\theta_{\boldsymbol{k}} d_{\boldsymbol{k}} - \sinh\theta_{\boldsymbol{k}} c_{\boldsymbol{k}}^\dagger \,. \end{aligned} \tag{5.10}$$

By checking the commutation relation (4.41) we see that $c_{\boldsymbol{k}}$ and $d_{\boldsymbol{k}}$ are boson operators, irrespective of the values of $\phi_{\boldsymbol{k}}$ and $\theta_{\boldsymbol{k}}$. Thus, the Bogoliubov transformation is a *canonical* transformation making bosons (*bogolons*) out of bosons[2]. If we take $\phi_{\boldsymbol{k}}$ to be the phase of $B_{\boldsymbol{k}}$ and let

$$\tanh 2\theta_{\boldsymbol{k}} = \frac{|B_{\boldsymbol{k}}|}{A_{\boldsymbol{k}}} \,, \tag{5.11}$$

the Hamiltonian in (5.9) turns to the harmonic oscillator form,

$$\mathcal{H}_{\boldsymbol{k}} = \omega_{\boldsymbol{k}} \left( c_{\boldsymbol{k}}^\dagger c_{\boldsymbol{k}} + d_{\boldsymbol{k}} d_{\boldsymbol{k}}^\dagger \right) \,, \tag{5.12}$$

with

$$\omega_{\boldsymbol{k}} = \sqrt{A_{\boldsymbol{k}}^2 - |B_{\boldsymbol{k}}|^2} \,. \tag{5.13}$$

For further details on the diagonalization process see Papers IV and V.

[2]In the standard Bogoliubov transformation the new bosons, $c_{\boldsymbol{k}}$ and $d_{\boldsymbol{k}}$, are sometimes called *bogolons* and we use this terminology also for the resulting bosons of the complex Bogoliubov transformation.

## 5.2 Diagonal Hamiltonians from SBMFT and LSWT for the 2D Heisenberg models on triangular and honeycomb lattices

The resulting diagonal Hamiltonians (obtained either from SBMFT or LSWT) can be written as a sum over harmonic oscillators of types $m = 1, \ldots, M$ with $M$ counting the total number of modes ($M = 2R$ in SBMFT and $M = R$ in LSWT with $R$ the number of sublattices, see Eq. (5.8)):

$$\mathcal{H} = E_0 + \sum_{m=1}^{M} \sum_{\boldsymbol{k}} \omega_{\boldsymbol{k},m} \left( \hat{n}_{\boldsymbol{k},m} + \frac{1}{2} \right) , \tag{5.14}$$

where $\hat{n}_{\boldsymbol{k},m} = g^{\dagger}_{\boldsymbol{k},m} g_{\boldsymbol{k},m}$ is the number operator composed of bogolons $g_{\boldsymbol{k},m}$. The expressions for the dispersion relations $\omega_{\boldsymbol{k},m}$ for the respective cases will be given below.

### 5.2.1 Dispersion relations for the honeycomb lattice

The dispersion relations for the honeycomb lattice are given by ($M = 4$ in Eq. (5.14), four degenerate modes from two Schwinger bosons on two sublattices)

$$\omega_{\boldsymbol{k}}^{\mathrm{SBMFT}} = \sqrt{(\lambda + 3J_2 Q_{\mathcal{B}} \eta_{2,\boldsymbol{k}})^2 - |\tfrac{3}{2} J_1 Q_{\mathcal{A}} \eta_{1,\boldsymbol{k}}|^2} \ , \tag{5.15}$$

in SBMFT, and by ($M = 2$ in Eq. (5.14), two degenerate modes from two sublattices)

$$\omega_{\boldsymbol{k}}^{\mathrm{LSWT}} = 3SJ_1 \sqrt{\left(1 - 2\tfrac{J_2}{J_1} \left(1 - \eta_{2,\boldsymbol{k}}\right)\right)^2 - |\eta_{1,\boldsymbol{k}}|^2} \, . \tag{5.16}$$

in LSWT. The geometrical factors, $\eta_{1,\boldsymbol{k}}$ and $\eta_{2,\boldsymbol{k}}$, for the honeycomb lattice are

$$\eta_{1,\boldsymbol{k}} = \frac{1}{3} \sum_{\boldsymbol{\alpha}} e^{i\boldsymbol{k}\cdot\boldsymbol{\alpha}} \ , \tag{5.17}$$

$$\eta_{2,\boldsymbol{k}} = \frac{1}{3} \sum_{\boldsymbol{\beta}} \cos(\boldsymbol{k} \cdot \boldsymbol{\beta}) \ . \tag{5.18}$$

The non-Bravais structure of the honeycomb lattice shows up by $\eta_{1,\boldsymbol{k}}$ in Eq. (5.17) being complex.

### 5.2.2 Dispersion relations for the triangular lattice

The dispersion relations for the triangular lattice are given by ($M = 6$ in Eq. (5.14), two degenerate Schwinger boson modes on each of the three sublattices)

$$\omega_{m\boldsymbol{k}}^{\mathrm{SBMFT}} = \sqrt{(\lambda + \tfrac{3}{2} J_1 Q_{\mathcal{B}} \gamma_{m,\boldsymbol{k}})^2 - (\tfrac{9}{2} J_1 Q_{\mathcal{A}} \gamma_{m,\boldsymbol{k}})^2} \ , \quad m = 1, 2, 3 \ , \tag{5.19}$$

in SBMFT, and by ($M = 3$ in Eq. (5.14), one from each sublattice)

$$\omega^{\text{LSWT}}_{m\boldsymbol{k}} = 3SJ_1\sqrt{(1+\gamma_{m,\boldsymbol{k}})^2 - (3\gamma_{m,\boldsymbol{k}})^2} \quad , \quad m = 1,2,3 \quad , \tag{5.20}$$

in LSWT. The geometrical factors for the triangular lattice are given by

$$\gamma_{1,\boldsymbol{k}} = \frac{1}{6}\sum_{\boldsymbol{\alpha}} \cos(\boldsymbol{k}\cdot\boldsymbol{\alpha}) \quad , \tag{5.21}$$

$$\gamma_{2,\boldsymbol{k}} = \frac{1}{6}\sum_{\boldsymbol{\alpha}} \cos(\boldsymbol{k}\cdot\boldsymbol{\alpha} + \frac{2\pi}{3}) \quad , \tag{5.22}$$

$$\gamma_{3,\boldsymbol{k}} = \frac{1}{6}\sum_{\boldsymbol{\alpha}} \cos(\boldsymbol{k}\cdot\boldsymbol{\alpha} - \frac{2\pi}{3}) \quad . \tag{5.23}$$

### 5.2.3 Determining the SBMFT parameters: minimizing the free energy

The parameters in the SBMFT dispersion relations are most conveniently determined from minimizing the free energy as described in Sec. 4.5.4. The energy to be inserted into Eq. (4.63) is given by the expectation value of the Hamiltonian in Eq. (5.14), and recognizing that the energy of a harmonic oscillator is $\epsilon_n = \omega(n+\frac{1}{2})$, we can interpret the systems described by the Hamiltonian in Eq. (5.14) as oscillators labeled by $\boldsymbol{k}$ and $m$, each contributing to the energy with

$$\epsilon_{n_{\boldsymbol{k},m}} = \omega_{\boldsymbol{k},m}\left(n_{\boldsymbol{k},m} + \frac{1}{2}\right) , \tag{5.24}$$

where $n_{\boldsymbol{k},m} = \langle \hat{n}_{\boldsymbol{k},m}\rangle$. The different states are then labeled by the values of $n_{\boldsymbol{k},m}$, ranging from 0 to $\infty$, and the sum in (4.63) can be written as

$$\sum_{\text{(states)}} = \prod_{m=1}^{M}\prod_{\boldsymbol{k}}\sum_{n_{\boldsymbol{k},m}} . \tag{5.25}$$

This gives

$$\begin{aligned} Z &= \sum_{\text{(states)}} \exp\left(-\beta\left(E_0 + \sum_{m=1}^{M}\sum_{\boldsymbol{k}}\epsilon_{n_{\boldsymbol{k},m}}\right)\right) \\ &= \exp(-\beta E_0)\prod_{m=1}^{M}\prod_{\boldsymbol{k}}\sum_{n_{\boldsymbol{k},m}}\exp\left(-\beta\epsilon_{n_{\boldsymbol{k},m}}\right) \\ &= \exp(-\beta E_0)\prod_{m=1}^{M}\prod_{\boldsymbol{k}}\left(\frac{1}{2\sinh(\beta\omega_{\boldsymbol{k},m}/2)}\right) , \end{aligned}$$

where in the third identity we have used $\sum_{n=0}^{\infty} e^{-nx} = (1-e^{-x})^{-1}$. We now insert $Z$ in the expression for the free energy Eq. (4.62), which then becomes

$$F = E_0 + \frac{1}{\beta}\sum_{m=1}^{M}\sum_{\boldsymbol{k}}\ln\left(2\sinh(\beta\omega_{\boldsymbol{k},m}/2)\right) . \tag{5.26}$$

By inserting the proper expressions for $E_0$ and the dispersion $\omega_{\boldsymbol{k},m}$ and then minimizing with respect to $\lambda$, $Q_{\mathcal{A}}$ and $Q_{\mathcal{B}}$ we obtain the desired minimization equations. To arrive at the results given in Papers IV and V we have converted the sum to an integral over the Brillouin zone, and used the Bose-Einstein distribution function

$$n_{\boldsymbol{k}} = \frac{1}{\exp(\beta\omega_{\boldsymbol{k}}) - 1}\,. \tag{5.27}$$

We note that the minimization equations will be temperature dependent and we will take advantage of this fact when we calculate the dynamic structure factor for the honeycomb lattice in Sec. 5.4.2. However, to investigate the ordering properties we need to investigate the $T = 0$ limit since, according to the Mermin-Wagner theorem [9], we already know that the $T \neq 0$ system is disordered. The question is whether the $T = 0$ ground state is ordered or not. One possible route is to carefully extrapolate the finite temperature result to zero temperature. This is the route we actually follow when determining the zero temperature uniform susceptibility for the honeycomb lattice in Sec. 5.4.3.

There is, however, another way to arrive at the $T = 0$ case which requires a careful analysis of the dispersion relations in terms of spin-waves, to be discussed next.

### 5.2.4 Spin-wave velocity and spin-wave "mass"

The elementary excitations of a spin system are called spin-waves. In our case the spin-waves are described by the harmonic oscillators in Eq. (5.14), the bogolons. Like all waves, spin-waves are collective phenomena, with many spins fluctuating in a correlated way to build up the wave.

We are interested in spin-waves (excitations) of the antiferromagnetic state, and since we have done a spin rotation we will look for these waves at the "ferromagnetic point" in the Brillouin zone, that is, at $\boldsymbol{k} \to \mathbf{0}$. The dispersion relation is *not* an observable (i.e. an expectation value) and this is why the spin rotation does make a difference. All observables must of course be evaluated at "antiferromagnetic points"[3].

Evaluating the LSWT dispersions in Eqs. (5.16) and (5.20) for small $\boldsymbol{k}$ gives us

$$\omega^{\text{LSWT}}_{m\boldsymbol{k}} = c^{\text{LSWT}}_{m}|\boldsymbol{k}| \tag{5.28}$$

with

$$c^{\text{LSWT}} = \frac{3J_1 S}{\sqrt{2}}\sqrt{1 - 6\tfrac{J_2}{J_1}}\,, \tag{5.29}$$

[3]We have here rotated the honeycomb lattice with respect to Paper V for pedagogical reasons to allow comparison with the triangular lattice. All lattice vectors (direct and reciprocal) mentioned in Paper V must therefore be rotated by $\pi$ around the $z$-axis to correspond to vectors in the present text.

in the honeycomb case, and

$$c_1^{\text{LSWT}} = \frac{3J_1S\sqrt{3}}{2}, \qquad c_2^{\text{LSWT}} = c_3^{\text{LSWT}} = \frac{c_1^{\text{LSWT}}}{\sqrt{2}} \tag{5.30}$$

in the triangular case.

From Eqs. (5.15) and (5.19) we find that also in SBMFT the dispersion relation for small $\boldsymbol{k}$ takes a relativistic form

$$\omega_{m\boldsymbol{k}}^{\text{SBMFT}} = c_m^{\text{SBMFT}} \sqrt{(M_m c_m^{\text{SBMFT}})^2 + |\boldsymbol{k}|^2}, \tag{5.31}$$

with $c_m^{\text{SBMFT}}$ and $\Delta_m \equiv M_m(c_m^{\text{SBMFT}})^2$ given by

$$c^{\text{SBMFT}} = \frac{3}{2}\sqrt{\tfrac{1}{2}J_1^2Q_{\mathcal{A}}^2 - 2J_2Q_{\mathcal{B}}(\lambda + 3J_2Q_{\mathcal{B}})}\ , \tag{5.32}$$

$$\Delta = \sqrt{(\lambda + 3J_2Q_{\mathcal{B}})^2 - (\tfrac{3}{2}J_1Q_{\mathcal{A}})^2}\ . \tag{5.33}$$

in the honeycomb case, and

$$c_1^{\text{SBMFT}} = \sqrt{(\tfrac{9}{4}J_1Q_{\mathcal{A}})^2\tfrac{1}{2} - \tfrac{3}{8}J_1Q_{\mathcal{B}}(\lambda + \tfrac{3}{4}J_1Q_{\mathcal{B}})}\ , \tag{5.34}$$

$$c_2^{\text{SBMFT}} = c_3^{\text{SBMFT}} = \sqrt{(\tfrac{9}{8}J_1Q_{\mathcal{A}})^2\tfrac{1}{2} + \tfrac{3}{16}J_1Q_{\mathcal{B}}(\lambda - \tfrac{3}{8}J_1Q_{\mathcal{B}})}\ , \tag{5.35}$$

and

$$\Delta_1 = \sqrt{(\lambda + \tfrac{3}{4}J_1Q_{\mathcal{B}})^2 - (\tfrac{9}{4}J_1Q_{\mathcal{A}})^2}, \tag{5.36}$$

$$\Delta_2 = \Delta_3 = \sqrt{(\lambda - \tfrac{3}{8}J_1Q_{\mathcal{B}})^2 - (\tfrac{9}{8}J_1Q_{\mathcal{A}})^2}\ . \tag{5.37}$$

in the triangular case. Once we have determined the SBMFT parameters $\lambda$, $Q_{\mathcal{A}}$, and $Q_{\mathcal{B}}$ by minimization of the free energy in Eq. (5.26), the spin-wave velocities and spin-wave masses can be evaluated (see Papers IV and V for further details, including graphs of the velocities and "masses" of the spin-waves).

The appearance of a mass term in Eq. (5.31) needs some comments. One can show, on general grounds, that the "mass" of an elementary excitation measures the inverse correlation length over which the microscopic degrees of freedom (here: the spins) are correlated [151]. A zero mass then indicates long range order (LRO). The Mermin-Wagner theorem tells us that we cannot have LRO at finite temperatures in 2D, and this is indeed vindicated in our numerical calculations of the masses; we find finite masses for all $T \neq 0$. At $T = 0$, though, we do get a zero mass for the triangular lattice and the honeycomb lattice at low frustration. This then indicates that *we have antiferromagnetic long range order at zero temperature* for both triangular and honeycomb lattices (as long as the frustration of the latter is sufficiently small).

For another perspective on this, let us look at the Bose-Einstein distribution function in (5.27). This is the distribution function for the spin-waves. We can directly see two things; if $\beta < \infty$ ($T \neq 0$) and $\omega_{\boldsymbol{k}} \neq 0$ we have a finite number of excited spin-waves, but if $\beta = \infty$ ($T = 0$) and $\omega_{\mathbf{0}} = 0$, the bosons (bogolons, spin-waves) *condense* at $\boldsymbol{k} = \mathbf{0}$. A condensate of bosons at $\boldsymbol{k} = \mathbf{0}$ means antiferromagnetic long range order. We will use the fact that we have LRO and that the bosons condense at $\boldsymbol{k} = \mathbf{0}$ when we rewrite the minimization equations so as to apply to the $T = 0$ case.

### 5.2.5 $T = 0$ formalism

As we have mentioned before, the values of the SBMFT parameters, $\lambda$, $Q_{\mathcal{A}}$, and $Q_{\mathcal{B}}$, can also be determined directly at $T = 0$. This is done via the substitution

$$\frac{n_{s\boldsymbol{k}}}{\omega_{s\boldsymbol{k}}} \rightarrow S_s^* \delta^{(2)}(\boldsymbol{k} - \boldsymbol{K}_s) \ , \tag{5.38}$$

where $S_s^*$ is a new unknown quantity measuring a Bose condensate and $\boldsymbol{K}_s$ are points in the Brillouin zone where we have condensation of bosons. A procedure for determining if and where in the Brillouin zone the bosons condense is thoroughly described in Paper IV. The condensation of the bosons implies that there is no gap in the spin-wave spectrum (i.e. $\omega_{s\boldsymbol{k}=\boldsymbol{K}_s} = 0$ in (5.31)) at $T = 0$: These $s$ equations together with the three minimization equations are sufficient to determine the $3 + s$ parameters $\lambda$, $Q_{\mathcal{A}}$, $Q_{\mathcal{B}}$ and $S_s^*$.

## 5.3 Results for the triangular lattice

Our aim has been to obtain an effective theory that recovers the LSWT results in the limit of infinite spin, thus justifying our choice of link operators in this limit. We indeed *exactly* recover the LSWT results in the limit of infinite spin and our solution is thus close to the correct large spin solution, i.e. for ground states close to the classical 120° ground state. Our solution might give valuable information also for smaller spin considering the fact that the favored candidate for the ground state for these spins is also the 120° state, consistent with our choice of link operators.

Next I will discuss the particulars of our solution, focusing on the dispersion relation for the spin-waves.

### 5.3.1 The dispersion relation

Following the procedure described in Paper IV, we find that bosons of the first mode condense at $\boldsymbol{K}_1 = \mathbf{0}$ for all values of the spin. As we pointed out in Sec. 5.2.4, condensation of bosons indicates that we have long range order. Leaving aside the type of order, we can immediately conclude that *the ground state of the 2D Heisenberg model on a triangular lattice is ordered.* The two other modes only condense in the limit of infinite spin, $S \rightarrow \infty$, and in this limit we exactly recover the LSWT result and the antiferromagnetic long range order indicated by the three massless modes. This justifies our choice of link operators.

Using the $T = 0$-formalism described in Sec. 5.2.5 we can determine the SBMFT parameters for $T = 0$. Inserting these values into Eq. (5.19) gives us the dispersion relation for the three spin-wave modes. In Fig. 5.3 we show

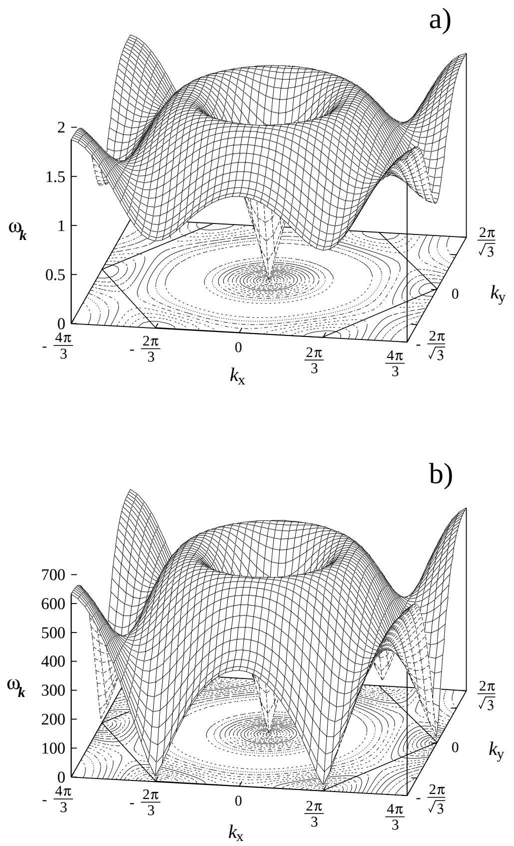


**Figure 5.3**: The dispersion relation for the 2D Heisenberg model on a triangular lattice for a) $S = 0.5$ and b) $S = 200$ at zero temperature. The gap at the ferromagnetic point is always zero while the gap at the antiferromagnetic points only tends to zero for large spin.

the dispersion relation for two values of the spin. In these pictures we have shifted the modes according to Fig. 5.1, obtaining only one mode in the larger Brillouin zone corresponding to the full triangular lattice.

As is clearly seen in Fig. 5.3, gaps open up at the corners of the Brillouin zone corresponding to two of the modes (the *corner modes*) acquiring mass. What does the massiveness of the corner modes reflect? Is their massiveness a signature that the ordered state is close to disorder? To understand how the corner modes become massive we need to consider the symmetry of the Hamiltonian. The effective Hamiltonian in Eq. (5.5) is invariant under $U(1)$ transformations, or, to be specific, rotations of the spins in the $x$-$z$-plane. The 120°-state, in contrast, does not have this symmetry and according to Goldstone's theorem, the spontaneous breaking of $U(1)$ symmetry should manifest itself in *one* massless *Goldstone mode*. This is indeed the case; we have one massless mode. The original Hamiltonian in Eq. (4.40) is $SU(2)$-invariant which should result in three Goldstone modes if the ground state is a 120°-state. Referring to these considerations we conclude that the massiveness of the corner modes does not indicate strong quantum fluctuations of the 120° ground state. Instead the massiveness of the corner modes is an artifact of the $SU(2)$ symmetry of the original theory having been replaced by the $U(1)$ symmetry of the effective theory. If the effective Hamiltonian had preserved the original $SU(2)$-symmetry, all three modes should have been massless at $T = 0$, indicating a long-range ordered ground state of the 120° type.

Interestingly, the first term in Eq. (5.4) that we neglected in obtaining the effective Hamiltonian is also neglected in LSWT (since it is cubic in the Holstein-Primakoff bosons, see Sec. 4.4.1 and Sec. 4.4.2). The three massless modes in LSWT are thus *not* due to LSWT preserving the $SU(2)$ symmetry of the Hamiltonian but rather a consequence of the neglect of energy terms proportional to $S^n$, $n < 1$ (such as the first term in Eq. (5.4)). In our SBMFT we can show (see Paper IV for details) that the energy gaps at the corners of the Brillouin zone scales as $S^{0.5}$. Neglecting energy terms of the same order as in LSWT should thus give a solution with three massless modes and, in the same sense as LSWT is correct for large spin, our SBMFT approach is valid if neglecting energy terms of the order of the mass gap. The SBMFT is an improvement of the LSWT, though, since the SBMFT approach only assumes local order while LSWT requires global order.

## 5.4 Results for the honeycomb lattice

In contrast to the model on the triangular lattice we have included a frustrating next-nearest neighbor term in the Hamiltonian for the honeycomb model (Eq. (4.39)) allowing us to drive the system "by hand" through a transition to a disordered state. This is explored in Sec. 5.4.1, where the stability of the Néel state against frustration is investigated. To connect to experiments we have calculated the dynamic structure factor and the results are presented in Sec. 5.4.2. In addition to the spin-wave velocity considered in Sec. 5.2.4, we have also studied the uniform susceptibility, presented in Sec. 5.4.3.

### 5.4.1 Stability of the Néel state

In figure 3 in Paper V we have plotted the logarithm of the mass vs. frustration at finite temperature. We see that turning on frustration makes the system more and more uncorrelated since the mass becomes enhanced by increasing frustration and the correlation length hence decreases (recall that mass $\sim$ (correlation length)$^{-1}$). At zero temperature this behavior eventually results in a phase transition from the LRO system at low frustration to a disordered system at high frustration. This is indicated in Fig. 5.4. The SBMFT curve is

**Figure 5.4**: Néel boundary for the frustrated 2D Heisenberg model on a honeycomb lattice. The inverse of the critical spin $S_c$ as a function of frustration $J_2/J_1$. The lines show the LSWT and the SBMFT result. They coincide for $J_2 = 0$ and for $J_2/J_1 = \frac{1}{6}$ at the classical point $S = \infty$. Note the Néel stability beyond the classical value in the SBMFT case.

obtained by calculating the frustration at which the boson condensation parameter $S^*$ in Eq. (5.38) vanishes for a specified spin $S$. The LSWT boundary is calculated from the vanishing of the sublattice magnetization,

$$m^{\uparrow\downarrow}_{\mathrm{LSWT}} = S + \frac{1}{2} - \frac{1}{N}\sum_{\boldsymbol{k}} \frac{1 + 2\frac{J_2}{J_1}\left(\eta_{\boldsymbol{k},2} - 1\right)}{\sqrt{\left[1 + 2\frac{J_2}{J_1}\left(\eta_{\boldsymbol{k},2} - 1\right)\right]^2 - |\eta_{\boldsymbol{k},1}|^2}}\,, \tag{5.39}$$

obtained from Eqs. (4.36), (4.44), (5.8), (5.10).

We see that quantum fluctuations in our SBMFT model (present for any finite spin, see Sec. 4.3.1) *stabilize* the classical ground state against frustration, that is, we need to have a larger $J_2/J_1$ to obtain a disordered state than in the classical limit, $1/S_c = 0$. Analogous results for the frustrated square lattice antiferromagnet support this result for large spin [152]. However, for smaller spin, in particular $S = \frac{1}{2}$, our solution over-estimates the stability of the Néel state and further investigations are needed to determine whether a stabilization beyond the classical Néel boundary takes place or not.

Let us now leave this issue and instead turn to a study of the dynamic structure factor.

### 5.4.2 The dynamic structure factor

The dynamic structure factor is (more or less) the quantity measured in neutron scattering experiments as we saw in Sec. 4.6. For finite temperatures the structure factor is rotationally invariant since we have a disordered system, as is also the case for $T = 0$ outside the Néel boundary in Fig. 5.4. In these regions in parameter space we can look at any component of the structure factor, and we have chosen the $xx$ component in our calculations, the structure factor being defined in Eqs. (4.65) and (4.66). Note that Eq. (4.66) is a spatial Fourier transform of the spin-spin correlation function *only* if the lattice vectors $\boldsymbol{R}$ are on a Bravais lattice.

With LSWT we get

$$\mathcal{S}_{xx}^{\text{LSWT}}(\boldsymbol{q},\omega) = \frac{S}{2} g_{\boldsymbol{q}} \left\{ (n_{\boldsymbol{q}} + 1)\, \delta(\omega_{\boldsymbol{q}} - \omega) + n_{\boldsymbol{q}} \delta(\omega_{\boldsymbol{q}} + \omega) \right\} . \tag{5.40}$$

with $n_{\boldsymbol{q}}$ the Bose-Einstein distribution in Eq. (5.27), $\omega_{\boldsymbol{q}}$ the LSWT dispersion relation in Eq. (5.16), and

$$g_{\boldsymbol{q}} = \cosh 2\theta_{\boldsymbol{q}} - \cos\phi_{\boldsymbol{q}} \sinh 2\theta_{\boldsymbol{q}} . \tag{5.41}$$

Here $\phi_{\boldsymbol{q}}$ is the phase of $\eta_{1,\boldsymbol{k}}$, and $\theta_{\boldsymbol{q}}$ is defined by

$$\tanh 2\theta_{\boldsymbol{q}} = \frac{|\eta_{1,\boldsymbol{q}}|}{1 - \frac{J_1}{J_2}(1 - \eta_{2,\boldsymbol{q}})} . \tag{5.42}$$

With SBMFT we obtain

$$\mathcal{S}_{xx}^{\text{SBMFT}}(\boldsymbol{q},\omega) = \mathcal{S}_1(\boldsymbol{q},\omega) + \mathcal{S}_2(\boldsymbol{q},\omega) \quad , \tag{5.43}$$

where

$$\mathcal{S}_1(\boldsymbol{q},\omega) = \frac{1}{2} \int \frac{d^2k}{A} \frac{(f_{\boldsymbol{k},\boldsymbol{k}+\boldsymbol{q}} + 1)}{2} n_{\boldsymbol{k}} (n_{\boldsymbol{k}+\boldsymbol{q}} + 1) \delta(\omega_{\boldsymbol{k}} - \omega_{\boldsymbol{k}+\boldsymbol{q}} + \omega) \quad , \tag{5.44}$$

$$\mathcal{S}_2(\boldsymbol{q},\omega) = \frac{1}{4} \int \frac{d^2k}{A} \frac{(f_{\boldsymbol{k},\boldsymbol{k}+\boldsymbol{q}} - 1)}{2} (n_{\boldsymbol{k}} + \Theta(\omega))(n_{\boldsymbol{k}+\boldsymbol{q}} + \Theta(\omega)) \delta(\omega_{\boldsymbol{k}} + \omega_{\boldsymbol{k}+\boldsymbol{q}} - |\omega|) \quad . \tag{5.45}$$

Here $A = 8\pi^2/(3\sqrt{3})$ is the area of the reciprocal unit cell, $\omega_{\boldsymbol{k}}$ is the SBMFT dispersion relation in Eq. (5.15),

$$f_{\boldsymbol{k},\boldsymbol{k}+\boldsymbol{q}} = \cosh(2\vartheta_{\boldsymbol{k}})\cosh(2\vartheta_{\boldsymbol{k}+\boldsymbol{q}}) - \cos(\phi_{\boldsymbol{k}} - \phi_{\boldsymbol{k}+\boldsymbol{q}})\sinh(2\vartheta_{\boldsymbol{k}})\sinh(2\vartheta_{\boldsymbol{k}+\boldsymbol{q}}) \quad , \tag{5.46}$$

$\Theta(\omega)$ is the Heavyside step function, and

$$\tanh(2\vartheta_{\boldsymbol{k}}) = \frac{\frac{3}{2}J_1 Q_{\mathcal{A}}|\eta_{1,\boldsymbol{k}}|}{\lambda + 3J_2 Q_{\mathcal{B}}\eta_{2,\boldsymbol{k}}} \quad . \tag{5.47}$$

Note that the non-Bravais character of the honeycomb lattice is reflected by the non-zero value of $\phi_{\boldsymbol{k}}$.

As we see, $\mathcal{S}_1$ and $\mathcal{S}_2$ describe two different physical processes and give rise to two distinct peaks in the structure factor. This is depicted in Fig. 5.5 where

**Figure 5.5**: The dynamic structure factor for spin $S = \frac{1}{2}$ at a low temperature $T = \frac{1}{5}J_1$ close to an antiferromagnetic point $\boldsymbol{q}_0$. In (a) no frustration is present, $J_2/J_1 = 0$, and in (b) the frustration is $J_2/J_1 = 0.1$, below the critical frustration. The peak corresponding to $\mathcal{S}_2$ has a gap which increases with frustration.

the contributions from $\mathcal{S}_1$ and $\mathcal{S}_2$ are indicated. In the language of neutron scattering, $\mathcal{S}_1$ describes a process where neutrons scatter against a single spin-wave, while $\mathcal{S}_2$ corresponds to a process where two spin-waves are created or annihilated by a neutron. This double-peak structure may be difficult to detect experimentally: at low temperature with a small gap the double-peak can be hard to resolve, while at higher temperatures the $\mathcal{S}_2$ peak may be smeared out by thermal fluctuations and too small to be detected. The double-peak structure of the dynamic structure factor is also present for frustrations outside the Néel boundary at finite temperature (see Fig. 7 in Paper V) while the $\mathcal{S}_1$ peak vanishes at $T = 0$ due to the lack of thermally excited spin-waves.

Comparing with LSWT (Eq. (5.40)), we note that in SBMFT, excitations come in pairs, while the LSWT excitations are single bosons. We also see that in SBMFT we have a sum over $\boldsymbol{k}$ in Eqs. (5.44) and (5.45); the spin-waves probed by the neutrons are superpositions of pairs of SBMFT bosonic excitations.

Given the dynamic structure factor, the uniform susceptibility is easily obtained as will be shown next.

### 5.4.3 Uniform susceptibility

The uniform (in both space and time) rotationally averaged (in spin space) susceptibility $\overline{\chi}$ can be calculated from the dynamic structure factor. The susceptibility is the (linear) response of the magnetization to an applied field and is readily derived from the structure factor as follows (for details, see for example [153]). The susceptibility can be divided into a real and an imaginary part,

$$\chi(\boldsymbol{k},\omega) = \chi'(\boldsymbol{k},\omega) + i\chi''(\boldsymbol{k},\omega)\,, \tag{5.48}$$

but for the static case $\omega = 0$ the imaginary part vanishes since

$$\chi''(\boldsymbol{k},\omega) = \int_0^\infty \chi(\boldsymbol{k},t)\sin\omega t\, dt\,. \tag{5.49}$$

From this and the Kramers-Krönig relation,

$$\chi'(\boldsymbol{k},\omega) = P\int \frac{d\omega'}{\pi}\frac{\chi''(\boldsymbol{k},\omega')}{\omega'-\omega}\,, \tag{5.50}$$

one obtains

$$\chi(\boldsymbol{k},\omega=0) = P\int \frac{d\omega'}{\pi}\frac{\chi''(\boldsymbol{k},\omega')}{\omega'}\,. \tag{5.51}$$

The fluctuation-dissipation theorem,

$$\chi''(\boldsymbol{k},\omega) = \frac{1}{2}\left(1-e^{\beta\omega}\right)\mathcal{S}(\boldsymbol{k},\omega) \tag{5.52}$$

with $\mathcal{S}(\boldsymbol{k},\omega)$ the dynamic structure factor defined in Eqs. (4.65) and (4.66), implies that

$$\chi(\boldsymbol{k},\omega=0) = \int \frac{d\omega'}{2\pi}\frac{\left(1-e^{\beta\omega'}\right)}{\omega'}\mathcal{S}(\boldsymbol{k},\omega')\,. \tag{5.53}$$

From Eq. (5.40) we note that $\mathcal{S}(\boldsymbol{k} = \mathbf{0}, \omega) \propto \delta(\omega)$ in LSWT. As seen in Eqs. (5.44) and (5.45), this is also true for SBMFT. We therefore use the limit $\lim_{\omega \to 0}(1 - e^{\beta\omega})/\omega = \beta$ and get

$$\overline{\chi} = \chi(\boldsymbol{k} = \mathbf{0}, \omega = 0) = \beta \int \frac{d\omega'}{2\pi} \mathcal{S}(\boldsymbol{k} = \mathbf{0}, \omega') = \beta \mathcal{S}(\boldsymbol{k} = \mathbf{0}, t = 0) \,. \tag{5.54}$$

With SBMFT we get

$$\bar{\chi} = \frac{2}{3k_B T} \int \frac{d^2 k}{A} \tfrac{1}{2} n_{\boldsymbol{k}} (n_{\boldsymbol{k}} + 1) \quad , \tag{5.55}$$

while LSWT yields

$$\overline{\chi} = \frac{1}{6J_1} \,. \tag{5.56}$$

Note that the SBMFT result has an intricate temperature dependence, precluding a direct treatment at zero temperature. Instead we must numerically extrapolate to $T = 0$. This is done in Paper V, and the LSWT and SBMFT results are shown in Fig. 4 in Paper V.

## 5.5 Conclusions

The presence of a Bose condensate within SBMFT indicates that the two models studied are both ordered at $T = 0$. In the case of the honeycomb lattice we have included a next-nearest neighbor term allowing us to disorder the system by increasing the frustration. For large spin, quantum fluctuations *stabilize* the Néel state against frustration (as compared to the classical case) but the effect at smaller spin calls for further study. For the model on the triangular lattice we are able to obtain a solution that agrees with LSWT for large spin, thus indicating that our solution is indeed correct. Whether or not our solution is valid for small spins calls for further investigations.

To conclude, the Schwinger-Boson Mean-Field theory works well for both non-Bravais and non-bipartite lattices, even though modifications are needed to adapt the theory to these structures.

# Acknowledgments

On my winding way towards Lake Tanganyika, the symbol of my aspirations, my thesis advisor *Henrik Johannesson* has given me invaluable support. He has helped me back onto the right track whenever I was lost and he has given me new inspiration when I was tired and discouraged. He has proof-read this thesis many times and I have really appreciated his numerous suggestions for improvements. He has prepared me for my journey, a journey that I will have to continue on my own, and if, one day, my dreams do come through, he has certainly a great part in it.

My fellow travelers, *Sebastian Eggert*, *Torbjörn Einarsson*, *Per Fröjdh*, and *Jari Kinaret* have taught me many things, and I am grateful to them for sharing their knowledge with me and for fruitful collaboration. I would also like to thank *Stellan Östlund* for his general support as well as other former and present members of the solid state theory group, in particular the group "coordinator" *Yvonne Steen*, without whom we would never have managed.

A former member of our group deserves special thanks, namely *Mimmi Öckerman*, whom I miss very much since she left for a career as a teacher. In this context I also want to thank my mentor *Agnes Wold*, who has given me new insights[4], and who, together with all the girls in the "protégée group", has supported my continued scientific career. Another valuable mentor has been *Björn Sundelius*.

I thank *Bengt Lundqvist* who, together with *Lotta Hedenäs* and *Björn Rudberg*, encouraged me to start my graduate studies. In addition, their didactic skills have inspired me in my own teaching.

I want to thank *Urban Engberg* and *Stefan Rommer* who, together with *Andy Polyakov* and *Lennart Bengtsson*, have maintained our computers in an outstanding way. Stefan, thank you for "saving" my thesis, or at least my nerves!

Without *Björn von Sydow*, and the rest of *"Inst. BRA"*, life would have been much less agreeable. Thank you all for numerous activities of different kinds.

Other cherished friends are *Johan* and *Pernilla* who have taken me out to

[4]C. Wennerås and A. E. Wold, Nepotism and sexism in peer-review, Accepted for publication in Nature, (1997). See also article published in Dagens Nyheter 1996 08 03.

the cinema and who have served me and my family delicious dinners now and then. 'Delicious dinners' is also a trade mark of *Peter* and *Maria*. They share my love for the Swedish mountains and traveling in general. I have enjoyed every one of the evenings when they have shown pictures from their journeys.

My lovely family deserves many thanks. My husband *Thomas* is my best friend and I thank him for being patient and supporting during these last few months. Our two children *Carolina* and *Simon* have not seen their mother very much lately, but Carolina: Mum has finished the book at last! I love you all.

Finally, I want to mention my parents *Marianne* and *Ingemar*, sisters *Sara* and *Katti*, and brothers *Micke*, *Jonas* and *Lukas*, without whom I would not have been the person I am today.

I would have liked to mention by name all of you who have supported me in one way or another but this thesis is already voluminous enough, so I just say:

THANK YOU ALL!

# Bibliography


[1] E. Wigner, Effects of the electron interaction on the energy levels of electrons in metals, *Transactions of the Faraday Society* **34**, 678–685 (1938).

[2] E. H. Hall, On a new action of the magnet on electric currents, *American Journal of Mathematics* **2**, 287–292 (1879).

[3] K. v. Klitzing, G. Dorda, and M. Pepper, New method for high-accuracy determination of the fine-structure constant based on quantized Hall resistance, *Physical Review Letters* **45**, 494–497 (1980).

[4] D. C. Tsui, H. L. Stormer, and A. C. Gossard, Two-dimensional magnetotransport in the extreme quantum limit, *Physical Review Letters* **48**, 1559–1562 (1982).

[5] J. G. Bednorz and K. A. Müller, Possible high $T_c$ superconductivity in the Ba-La-Cu-O System, *Zeitschrift für Physik B* **64**, 189–193 (1986).

[6] A. Schilling, M. Cantoni, J. D. Guo, and H. R. Ott, Superconductivity above 130K in the Hg-Ba-Ca-Cu-O system, *Nature* **363**, 56–58 (1993).

[7] A. Aharony, R. J. Birgeneau, A. Coniglio, M. A. Kastner, and H. E. Stanley, Magnetic phase diagram and magnetic pairing in doped $La_2CuO_4$, *Physical Review Letters* **60**, 1330–1333 (1988).

[8] H. A. Bethe, Zur Theorie der Metalle, *Zeitschrift für Physik* **71**, 205–226 (1931).

[9] N. D. Mermin and H. Wagner, Absence of ferromagnetism or antiferromagnetism in one- or two-dimensional isotropic Heisenberg models, *Physical Review Letters* **17**, 1133–1136 (1966).

[10] V. J. Emery, The many-body problem in one dimension, In *Correlated electron systems* [49], pages 166–198.

[11] P. W. Anderson, “Luttinger-Liquid” behavior of the normal metallic state of the 2D Hubbard model, *Physical Review Letters* **64**, 1839–1841 (1990).

[12] D. Pines and P. Nozières, *The theory of quantum liquids*, volume I, Addison-Wesley, Redwood City (1966).

[13] H. J. Schulz, Fermi liquids and non-Fermi liquids, in *Les Houches lecture notes*, Les Houches lecture notes, chapter Session LXI. Mesoscopic Quantum Physics, Elsevier, Amsterdam (1995).

[14] R. Claessen, R. O. Anderson, J. W. Allen, C. G. Olson, C. Janowitz, W. P. Ellis, S. Harm, M. Kalning, R. Manzke, and M. Skibowski, Fermi-liquid line shapes measured by angle-resolved photoemission spectroscopy on 1-$T$-$TiTe_2$, *Physical Review Letters* **69**, 808–811 (1992).

[15] K. Matho, Fermi liquid phenomenology: "marginality" approached from the FL side, *Physica B* **199 & 200**, 382–383 (1994).

[16] J. W. Allen, G.-H. Gweon, R. Claessen, and K. Matho, Fermi liquids and non-Fermi liquids – the view from photoemission, *Journal of Physics and Chemistry of Solids* **56**, 1849–1853 (1995).

[17] G. D. Mahan, *Many-particle physics*, Plenum, New York, second edition (1990).

[18] R. D. Mattuck, *A guide to Feynman diagrams in the many-body problem*, McGraw-Hill, New York, second edition (1976).

[19] J. W. Negele and H. Orland, *Quantum many-particle systems*, volume 68 of *Frontiers in physics*, Addison-Wesley, Redwood City (1992).

[20] G. Rickayzen, *Green's functions and condensed matter*, Academic Press, London, 5:th edition (1980).

[21] N. W. Ashcroft and N. D. Mermin, *Solid state physics*, Saunders College, Philadelphia (1976).

[22] J. Lindhard, On the properties of a gas of charged particles, *Dan. Mat. Fys. Medd.* **28**, 1–57 (1954).

[23] R. E. Peierls, *Quantum theory of solids*, Oxford University Press, London (1955).

[24] W. Kohn, Image of the Fermi surface in the vibration spectrum of a metal, *Physical Review Letters* **2**, 393–394 (1959).

[25] S. Tomonaga, Remarks on Bloch's method of sound waves applied to many-fermion problems, *Progress of Theoretical Physics* **5**, 544–569 (1950).

[26] J. M. Luttinger, An exactly soluble model of a many-fermion system, *Journal of Mathematical Physics* **4**, 1154–1162 (1963).

[27] D. C. Mattis and E. H. Lieb, Exact solution of a many-fermion system and its associated boson field, *Journal of Mathematical Physics* **6**, 304–312 (1965).

[28] D. C. Mattis, New wave-operator identity applied to the study of persistent currents in 1D, *Journal of Mathematical Physics* **15**, 609–612 (1974).

[29] A. Luther and I. Peschel, Single-particle states, Kohn anomaly, and pairing fluctuations in one dimension, *Physical Review B* **9**, 2911–2919 (1974).

[30] F. D. M. Haldane, 'Luttinger liquid theory' of one-dimensional quantum fluids: I. Properties of the Luttinger model and their extension to general 1D interacting spinless Fermi gas, *Journal of Physics C: Solid State Physics* **14**, 2585–2609 (1981).

[31] R. Heidenreich, R. Seiler, and D. A. Uhlenbrock, The Luttinger model, *Journal of Statistical Physics* **22**, 27–57 (1980).

[32] S. Coleman, Quantum sine-Gordon equation as the massive Thirring model, *Physical Review D* **11**, 2088–2097 (1975).

[33] S. Mandelstam, Soliton operators for the quantized sine-Gordon equation, *Physical Review D* **11**, 3026–3030 (1975).

[34] J. Sòlyom, The Fermi gas model of one-dimensional conductors, *Advances in Physics* **28**, 201–303 (1979).

[35] J. Voit, One-dimensional Fermi liquids, *Reports on Progress in Physics* **58**, 977–1116 (1995).

[36] E. Fradkin, *Field theories of condensed matter systems*, Frontiers in physics, Addison-Wesley, Redwood City, California, first edition (1991).

[37] X. G. Wen, Metallic non-Fermi-liquid fixed point in two and higher dimensions, *Physical Review B* **42**, 6623–6630 (1990).

[38] A. Houghton and J. B. Marston, Bosonization and fermion liquids in dimensions greater than one, *Physical Review B* **48**, 7790–7808 (1993).

[39] A. Nersesyan. Lecture notes on bosonization, Solid State Theory Seminar 1993. Institute of Theoretical Physics, Chalmers University of Technology (1993).

[40] P. Goddard and D. Olive, Kac-Moody and Virasoro algebras in relation to quantum physics, *International Journal of Modern Physics A* **1**, 303–414 (1986).

[41] Proceedings of the Institute for Theoretical Physics conference on non-Fermi liquid behavior in metals (Santa Barbara, USA, 17-21 June 1996), *Journal of Physics: Condensed Matter* **8** (1996).

[42] M. Brech, J. Voit, and H. Büttner, Momentum distribution function of the one-dimensional Hubbard model–an analytical approach., *Europhysics Letters* **12**, 289–294 (1990).

[43] J. Voit, Charge-spin separation and the spectral properties of Luttinger liquids, *Journal of Physics: Condensed Matter* **5**, 8305–8336 (1993).

[44] J. Voit, Charge-spin separation and the spectral properties of Luttinger liquids, *Physical Review B* **47**, 6740–6743 (1993).

[45] V. Meden and K. Schönhammer, Spectral functions for the Tomonaga-Luttinger model, *Physical review B* **46**, 15753–15760 (1992).

[46] K. Schönhammer and V. Meden, Nonuniversal spectral properties of the Luttinger model, *Physical Review B* **47**, 16205–16215 (1993).

[47] K. Schönhammer and V. Meden, Correlation effects in photoemission from low dimensional metals, *Journal of Electron Spectroscopy and Related Phenomena* **62**, 225–236 (1993).

[48] Y. Suzumura, The Density of states of the Tomonaga-Luttinger model, *Progress of Theoretical Physics* **63**, 51–61 (1980).

[49] V. J. Emery, editor, *Correlated electron systems*, volume 9 of *Jerusalem Winter School for Theoretical Physics*, Singapore (1993). World Scientific.

[50] S. Eggert and I. Affleck, Magnetic impurities in half-integer-spin Heisenberg antiferromagnetic chains, *Physical Review B* **46**, 10866–10883 (1992).

[51] E. H. Lieb and F. Y. Wu, Absence of Mott transition in an exact solution of the short-range, one-band model in one dimension, *Physical Review Letters* **20**, 1445–1448 (1968).

[52] H. Gould and J. Tobochnik, *An introduction to computer simulation methods*, Addison-Wesley, Reading, Massachusetts, second edition (1996).

[53] K. G. Wilson, The renormalization group and critical phenomena, *Reviews of Modern Physics* **55**, 583–600 (1983).

[54] D. J. Amit, *Field theory, the renormalization group, and critical phenomena*, World Scientific, Singapore, second edition (1984).

[55] P. Pfeuty and G. Toulouse, *Introduction to the renormalization group and to critical phenomena*, John Wiley & Sons, London (1977).

[56] S.-T. Chui and P. A. Lee, Equivalence of a one-dimensional fermion model and the two-dimensional coulomb gas, *Physical Review Letters* **35**, 315–318 (1975).

[57] J. M. Kosterlitz, The critical properties of the two-dimensional $xy$ model, *Journal of Physics C: Solid State Physics* **7**, 1046–1060 (1974).

[58] J. M. Kosterlitz and D. J. Thouless, Ordering, metastability and phase transitions in two-dimensional systems, *Journal of Physics C: Solid State Physics* **6**, 1181–1203 (1973).

[59] R. Shankar, Renormalization-group approach to interacting fermions, *Reviews of Modern Physics* **66**, 129–192 (1994).

[60] H. J. Schulz, Correlated fermions in one dimension, *International Journal of Modern Physics B* **5**, 57–74 (1991).

[61] H. J. Schulz, Correlation exponents and the metal-insulator transition in the one-dimensional Hubbard model, *Physical Review Letters* **64**, 2831–2834 (1990).

[62] B. G. Levi, Experiment reveals a new type of electron system, *Physics Today* **47**, June, 21–23 (1994).

[63] B. G. Levi, One-dimensional systems show signs of interacting electrons, *Physics Today* **49**, September, 19–21 (1996).

[64] S. Tarucha, T. Honda, and T. Saku, Reduction of quantized conductance at low temperatures observed in 2 to 10 $\mu m$-long quantum wires, *Solid State Communications* **94**, 413–418 (1995).

[65] A. Yacoby, H. L. Stormer, N. S. Wingreen, L. N. Pfeiffer, K. W. Baldwin, and K. W. West, Nonuniversal conductance quantization in quantum wires, *Physical Review Letters* **77**, 4612–4615 (1996).

[66] C. L. Kane and M. P. A. Fisher, Transport in a one-channel Luttinger liquid, *Physical Review Letters* **68**, 1220–1223 (1992).

[67] C. L. Kane and M. P. A. Fisher, Transmission through barriers and resonant tunneling in an interacting one-dimensional electron gas, *Physical Review B* **46**, 15233–15262 (1992).

[68] M. Ogata and H. Fukuyama, Collapse of quantized conductance in a dirty Tomonaga-Luttinger liquid, *Physical Review Letters* **73**, 468–471 (1994).

[69] I. Safi and H. J. Schulz, Transport in an inhomogeneous interacting one-dimensional system, *Physical Review B* **52**, R17040–R17043 (1995).

[70] D. L. Maslov and M. Stone, Landauer conductance of Luttinger liquids with leads, *Physical Review B* **52**, R5539–R5542 (1995).

[71] V. V. Ponomarenko, Renormalization of the one-dimensional conductance in the Luttinger-liquid model, *Physical Review B* **52**, R8666–R8667 (1995).

[72] B. I. Halperin, Quantized Hall conductance, current-carrying edge states, and the exxistence of extended states in a two-dimensional disordered potential, *Physical Review B* **25**, 2185–2190 (1982).

[73] R. B. Laughlin, Anomalous quantum Hall effect: An incompressible quantum fluid with fractionally charged excitations, *Physical Review Letters* **50**, 1395–1398 (1983).

[74] X.-G. Wen, Topological orders and edge excitations in FQH states, *Advances in Physics* **44**, 405–473 (1995).

[75] F. P. Milliken, C. P. Umbach, and R. A. Webb, Indications of a Luttinger liquid in the fractional quantum Hall regime, *Solid State Communications* **97**, 309–313 (1996).

[76] X.-G. Wen, Edge transport properties of the fractional quantum Hall states and weak-impurity scattering of a one-dimensional charge-density wave, *Physical Review B* **44**, 5708–5719 (1991).

[77] K. Moon, H. Yi, C. L. Kane, S. M. Girvin, and M. P. A. Fisher, Resonant tunneling between quantum Hall edge states, *Physical Review Letters* **71**, 4381–4384 (1993).

[78] P. Fendley, A. W. W. Ludwig, and H. Saleur, Exact conductance through point contacts in the $\nu = 1/3$ fractional quantum Hall effect, *Physical Review Letters* **74**, 3005–3008 (1995).

[79] A. M. Chang, L. N. Pfeiffer, and K. W. West, Observation of chiral Luttinger behavior in electron tunneling into fractional quantum Hall edges, *Physical Review Letters* **77**, 2538–2541 (1996).

[80] S. R. Renn and D. P. Arovas, Nonlinear $I(V)$ characteristics of Luttinger liquids and gated Hall bars, *Physical Review B* **51**, 16832–16839 (1995).

[81] D. Jérome and H. J. Schulz, Organic conductors and superconductors, *Advances in Physics* **31**, 299–490 (1982).

[82] K. Bechgaard, C. S. Jacobsen, K. Mortensen, H. J. Pedersen, and N. Thorup, The properties of five highly conducting salts: $(TMTSF)_2X$, $X = PF_6^-$, $AsF_6^-$, $SbF_6^-$, $BF_4^-$ and $NO_3^-$, derived from TetraMethylTetraSelenaFulvalene $(TMTSF)$, *Solid State Communications* **33**, 1119–1125 (1980).

[83] C. S. Jacobsen, D. B. Tanner, and K. Bechgaard, Dimensionality crossover in the organic superconductor tetramethyltetraselenafulvalene hexafluorophosphate $[(TMTSF)_2PF_6]$, *Physical Review Letters* **46**, 1142–1145 (1981).

[84] K. Bechgaard and D. Jérome, Organic conductors and organic superconductivity, *Physica Scripta* **T39**, 37–44 (1991).

[85] P. Wzietek, F. Creuzet, C. Bourbonnais, D. Jérome, K. Bechgaard, and P. Batail, Nuclear relaxation and electronic correlations in quasi-one-dimensional organic conductors. II. Experiments, *Journal de Physique I. France* **3**, 171–201 (1993).

[86] B. Dardel, D. Malterre, M. Grioni, P. Weibel, Y. Baer, J. Voit, and D. Jérôme, Possible observation of a Luttinger-liquid behavior from photoemission spectroscopy of one-dimensional organic conductors, *Europhysics Letters* **24**, 687–692 (1993).

[87] Y. Hwu, P. Alméras, M. Marsi, H. Berger, F. Lévy, M. Grioni, D. Malterre, and G. Margaritondo, Photoemission near the Fermi energy in one dimension, *Physical Review B* **46**, 13624–13626 (1992).

[88] M. Nakamura, A. Sekiyama, H. Namatame, A. Fujimori, H. Yoshihara, T. Ohtani, A. Misu, and M. Takano, Metal-semiconductor transition and Luttinger-liquid behavior in quasi-one-dimensional $BaVS_3$ studied by photoemission spectroscopy, *Physical Review B* **49**, 16191–16201 (1994).

[89] G.-H. Gweon, J. W. Allen, R. Claessen, J. A. Clack, D. M. Poirier, P. J. Benning, C. G. Olson, W. P. Ellis, Y.-X. Zhang, L. F. Schneemeyer, J. Marcus, and C. Schlenker, Fermi surfaces and single-particle spectral functions of low-dimensional inorganic non-cuprate compounds: the molybdenum bronzes, *Journal of Physics: Condensed Matter* **8**, 9923–9938 (1996).

[90] B. Dardel, D. Malterre, M. Grioni, P. Weibel, Y. Baer, and F. Lévy, Unusual photoemission spectral function of quasi-one-dimensional metals, *Physical Review Letters* **67**, 3144–3147 (1991).

[91] M. P. A. Fisher and L. I. Glazman. Transport in a one-dimensional Luttinger liquid. cond-mat/9610037. To be published in "Mesoscopic Electron Transport" edited by L. Kowenhoven, G. Schoen, and L. Sohn, NATO ASI Series E, Kluwer Ac. Publ., Dordrecht.

[92] F. Mila and X. Zotos, Phase diagram of the one-dimensional extended Hubbard model at quarter-filling, *Europhysics Letters* **24**, 133–138 (1993).

[93] M. B. Green, J. H. Schwarz, and E. Witten, *Superstring theory*, Monographs on Mathematical Physics, Cambridge University Press, Cambridge (1994).

[94] R. Marnelius, Classical field theory: A course on the foundation of theoretical dynamics. Institute of Theoretical Physics, Göteborg (1989).

[95] E. Wong and I. Affleck, Tunneling in quantum wires: A boundary conformal field theory approach, *Nuclear Physics B* **417**, 403–438 (1994).

[96] H. Frahm and V. E. Korepin, Critical exponents for the one-dimensionel Hubbard model, *Physical Review B* **42**, 10553–10565 (1990).

[97] H. Frahm and V. E. Korepin, Correlation functions of the one-dimensional Hubbard model in a magnetic field, *Physical Review B* **43**, 5653–5662 (1991).

[98] M. Fuentes, A. Lopez, E. Fradkin, and E. Moreno, Bosonization rules in $\frac{1}{2}+1$ dimensions, *Nuclear Physics B* **450**, 603–640 (1995).

[99] M. Fabrizio and A. O. Gogolin, Interacting one-dimensional electron gas with open boundaries, *Physical Review B* **51**, 17827–17841 (1995).

[100] I. S. Gradshteyn and I. M. Ryzhik, *Table of integrals, series, and products*, Academic Press, San Diego, California, fifth edition (1994).

[101] D. C. Mattis, *The theory of magnetism I, statics and dynamics*, Springer-Verlag, Berlin Heidelberg New York (1981).

[102] H. P. Myers, *Introductory solid state physics*, Taylor & Francis, London (1990).

[103] F. Seitz, D. Turnbull, and H. Ehrenreich, *Solid state physics*, volume 21 of *Solid State Physics: Advances in Research and Applications*, Academic Press, New York (1968).

[104] D. Adler, *Insulating and metallic states in transition metal oxides*, pages 1–113, Volume 21 of *Solid State Physics: Advances in Research and Applications* [103] (1968).

[105] W. Heisenberg, Zur Theorie des Ferromagnetismus, *Zeitschrift für Physik* **49**, 619–636 (1928).

[106] P. A. M. Dirac, Quantum mechanics of many-electron systems, *Proceedings of the Royal Society of London* **A123**, 714–733 (1929).

[107] J. J. Sakurai, *Modern quantum mechanics*, Addison-Wesley (1985).

[108] D. P. Tunstall and W. Barford, editors, *High temperature superconductivity*, Bristol, Philadelphia and New York (1991). Adam Hilger.

[109] W. A. Goddard, The quantum chemistry view of high temperature superconductors, In Tunstall and Barford [108], pages 351–392.

[110] H. Haken and H. C. Wolf, *The physics of atom and quanta, introduction to experiments and theory*, Springer-Verlag, Berlin, third corrected and enlarged edition edition (1993).

[111] G. T. Rado and H. Suhl, *Magnetism I*, volume 1 of *Magnetism: A Treatise on Modern Theory and Materials*, Academic Press, New York and London (1963).

[112] P. W. Anderson, *Exchange in insulators: superexchange, direct exchange, and double exchange*, chapter 2, pages 25–83, Volume 1 of *Magnetism: A Treatise on Modern Theory and Materials* [111] (1963).

[113] H. A. Kramers, L'interaction entre les atomes magnétogénes dans un cristal paramagnétique, *Physica* **1**, 182–192 (1934).

[114] L. Néel, Influence des fluctuations du champ moléculaire sur les propriétés magnétiques des corps, *Annales de physique (Paris)* **18**, 5–105 (1932).

[115] J. F. Annett and R. M. Martin, Electronic Hamiltonian and antiferromagnetic interactions in $La_2CuO_4$, *Physical Review B* **40**, 2620–2623 (1989).

[116] M. Inui, S. Doniach, and M. Gabay, Doping dependence of antiferromagnetic correlations in high-temperature superconductors, *Physical Review B* **38**, 6631–6635 (1988).

[117] S. Bacci, E. Gagliano, and F. Nori, Frustrated spin (J-J') systems do not model the magnetic properties of high-temperature superconductors, *International Journal of Modern Physics B* **5**, 325–339 (1991).

[118] S. L. Sondhi, S. M. Girvin, J. P. Carini, and D. Shahar, Continuous quantum phase transitions, *Reviews of Modern Physics* **69**, 315–333 (1997).

[119] E. Manousakis, The spin-$\frac{1}{2}$ Heisenberg antiferromagnet on a square lattice and its application to cuprous oxides, *Reviews of Modern Physics* **63**, 1–62 (1991).

[120] E. J. Neves and J. F. Perez, Long range order in the ground state of two-dimensional antiferromagnets, *Physics Letters* **114A**, 331–333 (1986).

[121] I. Affleck, T. Kennedy, E. H. Lieb, and H. Tasaki, Valence bond ground states in isotropic quantum antiferromagnets, *Communications in Mathematical Physics* **115**, 477–528 (1988).

[122] D. A. Huse and V. Elser, Simple variational wave functions for two-dimensional Heisenberg spin-$\frac{1}{2}$ antiferromagnets, *Physical Review Letters* **60**, 2531–2534 (1988).

[123] I. Ritchey, P. Chandra, and P. Coleman, Spin folding in the two-dimensional Heisenberg *kagomé* antiferromagnet, *Physical Review B* **47**, 15342–15345 (1993).

[124] A. Bouvet, L. P. Regnault, and J. Rossat-Mignod, Critical spin dynamics of the planar two-dimensional compound $BaNi_2(PO_4)_2$, *Physica B* **180** & **181**, 185–187 (1992).

[125] J. Oitmaa and D. D. Betts, The ground state of two quantum models of magnetism, *Canadian Journal of Physics* **56**, 897–901 (1978).

[126] J. D. Reger, J. A. Riera, and A. P. Young, Monte Carlo simulations of the spin-$\frac{1}{2}$ Heisenberg antiferromagnet in two dimensions, *Journal of Physics: Condensed Matter* **1**, 1855–1865 (1989).

[127] J. Oitmaa, C. J. Hamer, and Z. Weihong, Quantum magnets on the honeycomb and the triangular lattice at $T = 0$, *Physical Review B* **45**, 9834–9841 (1992).

[128] Z. Weihong, J. Oitmaa, and C. J. Hamer, Second-order spin-wave results for the quantum $XXZ$ and $XY$ models with anisotropy, *Physical Review B* **44**, 11 869 – 11 881 (1991).

[129] D. P. Arovas and A. Auerbach, Functional integral theories of low-dimensional quantum Heisenberg models, *Physical Review B* **38**, 316–332 (1988).

[130] A. Auerbach and D. P. Arovas, Spin dynamics in the square-lattice antiferromagnet, *Physical Review Letters* **61**, 617–620 (1988).

[131] P. W. Anderson, Resonating valence bonds: a new kind of insulator, *Materials Research Bulletin* **8**, 153–160 (1973).

[132] V. Kalmeyer and R. B. Laughlin, Equivalence of the resonating-valence-bond and fractional quantum Hall states, *Physical Review Letters* **59**, 2095–2098 (1987).

[133] T. Jolicoeur and J. C. L. Guillou, Spin-wave results for the triangular Heisenberg antiferromagnet, *Physical Review B* **40**, 2727–2729 (1989).

[134] D. Yoshioka and J. Miyazaki, Boson mean field theory of the triangular lattice Heisenberg model, *Journal of The Physical Society of Japan* **60**, 614–624 (1991).

[135] R. R. P. Singh and D. A. Huse, Three-sublattice order in triangular- and kagomé-lattice spin-half antiferromagnets, *Physical Review Letters* **68**, 1766–1769 (1992).

[136] B. Bernu, C. Lhuillier, and L. Pierre, Signature of Néel order in exact spectra of quantum antiferromagnets on finite lattices, *Physical Review Letters* **69**, 2590–2593 (1992).

[137] N. Elstner, R. R. P. Singh, and A. P. Young, Finite temperature properties of the spin-$\frac{1}{2}$ Heisenberg antiferromagnet on the triangular lattice, *Physical Review Letters* **71**, 1629–1632 (1993).

[138] Y. R. Wang, Spin liquid state of Wigner-Jordan fermions of the quantum antiferromagnetic Heisenberg model on a triangular lattice, *Physical Review B* **45**, 12604 (1992).

[139] K. Yang, L. K. Warman, and S. M. Girvin, Possible spin-liquid states on the triangular and kagomé lattices, *Physical Review Letters* **70**, 2641–2644 (1993).

[140] T. Dombre and N. Read, Nonlinear $\sigma$ models for triangular quantum antiferromagnets, *Physical Review B* **39**, 6797–6801 (1989).

[141] K. Lefmann and P. Hedegård, Neutron-scattering cross section of the $S = \frac{1}{2}$ Heisenberg triangular antiferromagnet, *Physical Review B* **50**, 1074–1083 (1994).

[142] H. A. Ceccatto, C. J. Gazza, and A. E. Trumper, Comment on “Quantum spin nematics: moment-free magnetism”, *Physical Review Letters* **72**, 1943 (1994).

[143] P. Coleman and P. Chandra, Coleman and Chandra reply, *Physical Review Letters* **72**, 1944 (1994).

[144] T. Holstein and H. Primakoff, Field dependence of the intrinsic domain magnetization of a ferromagnet, *Physical Review* **58**, 1098 (1940).

[145] P. W. Anderson, An approximate quantum theory of the antiferromagnetic ground state, *Physical Review* **86**, 694–701 (1952).

[146] J. Schwinger, On angular momentum, in L. Biedenharn and H. V. Dam, editors, *Quantum theory of angular momentum*, reprinted U.S.Atomic Energy Commission Rpt. NYO-3071 (1952), Academic, New York (1965).

[147] P. Chandra, P. Coleman, and A. I. Larkin, A quantum fluids approach to frustrated Heisenberg models, *Journal of Physics: Condensed Matter* **2**, 7933–7972 (1990).

[148] F. Mila, D. Poilblanc, and C. Bruder, Spin dynamics in a frustrated magnet with short-range order, *Physical Review B* **43**, 7891–7898 (1991).

[149] T. Einarsson, P. Fröjdh, and H. Johannesson, Weakly frustrated spin-$\frac{1}{2}$ Heisenberg antiferromagnet in two dimensions: thermodynamic parameters and the stability of the Néel state, *Physical Review B* **45**, 13121–13124 (1992).

[150] R. M. White, *Quantum theory of magnetism*, volume 32 of *Solid-State Sciences*, Springer-Verlag, Berlin, second edition (1983).

[151] J. B. Kogut, An introduction to lattice gauge theory and spin systems, *Reviews of Modern Physics* **51**, 659–713 (1979).

[152] F. Mila, D. Poilblanc, and C. Bruder, Spin dynamics in a frustrated magnet with short-range order, *Physical Review B* **43**, 7891–7898 (1991).

[153] A. Sjölander, Graduate course in irreversible statistical physics. Institute of Theoretical Physics, Chalmers University of Technology and Göteborg University (1990).

# Paper I

# Paper II

# Paper III

# Paper IV

# Paper V